Combustion modeling for virtual SI engine calibration with the help of 0D/3D methods.

Von der Fakultät für Maschinenbau,Verfahrens- und Energietechnik
der Technischen Universität Bergakademie Freiberg
genehmigte

Dissertation

zur Erlangung des akademischen Grades
Doktor-Ingenieur
(Dr.-Ing.)
vorgelegt

von

Diplom-Ingenieur
Sebastian Grasreiner

aus Erfurt.

Berichter: Univ.-Prof. Dr.-Ing. Christian Hasse, Freiberg
Univ.-Prof. Dr.-Ing. Michael Wensing, Erlangen

Freiberg, 6. Juli 2012.

The man who said,
"I'd rather be lucky than good."
saw deeply into life. People are afraid to face how
great a part of life is dependent on luck. It's
scary to think so much is out of one's control.

Der Mann, der gesagt hat:
"Ich hätte lieber Glück als Talent",
hat tiefe Lebensweisheit bewiesen. Manchmal will
man nicht wahrhaben, wie viel im Leben vom
Glück abhängt. Es ist erschreckend, wie viel
außerhalb der eigenen Kontrolle liegt.

(Woody Allen - "Match Point")

Danksagung.

heiter anfühlen darf.

Last but definitely not least möchte ich meine Familien Grasreiner, Spitschan und Mayrhofer sowie meine Freundin erwähnen. Sie haben stets ein wenig extra Motivation und Aufheiterung für mich parat gehabt.
Auch falls ich noch ein paar Mal erklären darf, warum ich nun *keine Arztpraxis* eröffne und man mich auch nicht *"Sie'zen"* muss, ist ihnen meine Dankbarkeit dauerhaft sicher.

Diese Arbeit ist zwei besonderen Menschen in meinem Leben gewidmet:

<div align="center">

Sylvia und *Ottomar.*

</div>

Das Leben sorgt ausgezeichnet für uns.

Eidesstattliche Erklärung.

Ich versichere, dass ich diese Arbeit selbständig verfasst und keine anderen Hilfsmittel als die angegebenen benutzt habe. Die Stellen der Arbeit, die anderen Werken dem Wortlaut oder dem Sinn nach entnommen sind, habe ich in jedem einzelnen Fall unter Angabe der Quelle als Entlehnung kenntlich gemacht. Diese Versicherung bezieht sich auch auf die bildlichen Darstellungen.

Die Dissertation ist bisher keiner anderen Fakultät vorgelegt worden.

Ich erkläre, dass ich bisher kein Promotionsverfahren erfolglos beendet habe und dass keine Aberkennung eines bereits erworbenen Doktorgrades vorliegt.

6. Juli 2012   Sebastian Grasreiner

Abstract.

Spark ignited engines are still important for conventional as well as for hybrid power trains and are thus objective to optimization. Today a lot of functionalities arise from software solutions, which have to be calibrated. Modern engine technologies provide an extensive variability considering their valve train, fuel injection and load control. Thus, calibration efforts are really high and shall be reduced by introduction of virtual methods.

In this work a physical 0D combustion model is set up, which can cope with a new generation of spark ignition engines. Therefore, at first cylinder thermodynamics are modeled and validated in the whole engine map with the help of a real-time capable approach. Afterwards an up to date turbulence model is introduced, which is based on a quasi-dimensional $k - \varepsilon-$approach and can cope with turbulence production from large scale shearing. A simplified model for ignition delay is implemented which emphasizes the transfer from laminar to turbulent flame propagation after ignition. The modeling is completed with the calculation of overall heat release rates in a 0D entrainment approach with the help of turbulent flame velocities.

After validation of all sub-models, the 0D combustion prediction is used in combination with a 1D gas exchange analysis to virtually calibrate the modern engine torque structure and the ECU function for exhaust gas temperature with extensive simulations.

Zusammenfassung.

Moderne Ottomotoren spielen heute sowohl in konventionellen als auch hybriden Fahrzeugantrieben eine große Rolle. Aktuelle Konzepte sind hochvariabel bezüglich Ventilsteuerung, Kraftstoffeinspritzung und Laststeuerung und ihre Optimierungspotentiale erwachsen zumeist aus neuen Softwarefunktionen. Deren Applikation ist zeit- und kostenintensiv und soll durch virtuelle Methoden unterstützt werden.

In der vorliegenden Arbeit wird ein physikalisches 0D Verbrennungsmodell für Ottomotoren aufgebaut und bis zur praktischen Anwendung geführt. Dafür wurde zuerst die Thermodynamik echtzeitfähig modelliert und im gesamten Motorenkennfeld abgeglichen. Der Aufbau eines neuen Turbulenzmodells auf Basis der quasidimensionalen $k - \varepsilon-$Gleichung ermöglicht anschließend, die veränderlichen Einflüsse globaler Ladungsbewegung auf die Turbulenz abzubilden. Für den Brennverzug wurde ein vereinfachtes Modell abgeleitet, welches den Übergang von laminarer zu turbulenter Flammenausbreitung nach der Zündung in den Vordergrund stellt. Der restliche Brennverlauf wird durch die physikalische Ermittlung der turbulenten Brenngeschwindigkeit in einem 0D Entrainment-Ansatz dargestellt.

Nach Validierung aller Teilmodelle erfolgt die virtuelle Bedatung der Momentenstruktur und der Abgastemperaturfunktion für das Motorsteuergerät.

Contents

9

Nomenclature

0D	zero-dimensional
1D	one-dimensional
3D	three-dimensional
a.TDC	after top dead center
abs	absolute, mathematical absolute value
afr, AFR	air-fuel ratio
afvap	after evaporation
ang.	angular
avg	average, averaged
b.ITDC	before ignition top dead center
BDC	bottom dead center
bmep	break mean effective pressure
bnd	boundary
CA, degCA, °CA	degree crank angle
CA50	crank angle of 50% mass burned
CAD	computer aided design
CFD	computational fluid dynamics
chem	chemical
CO	carbon oxide
comb.	combustion
CPU	central processing unit
cyl.	cylinder
dev.	deviation, development
DI	direct injection
DNS	direct numerical simulation
DOHC	double over head cam shaft
ECU	engine control unit
eff	effective
eng.	engine
ex	exhaust related
Ex	expansion factor
ex-valve	exhaust valve
exc	eccentricity
fluct.	fluctuation
fmep	friction mean effective pressure

frac	fraction
GDI	gasoline direct injection
GT	Gamma Technologies
HC	hydrocarbon
HCCI	homogeneous charge compression ignition
HiL	Hardware in the loop
httr	heat transfer
idel	ignition delay
ign.	igntion
imep	indicated mean effective pressure
ind.	indicated
ini	initialization, initialized
ITDC	ignition top dead center
IV	intake valve
IVC	intake valve closure, intake valve closing
IVO	intake valve opening
KE	kinetic energy (mean flow)
LES	large eddy simulation
log	logarithmic
math	mathematical
max	maximum, maximal
mech	mechanical
min	minimum, minimal
mixt.	mixture
MLP	multi layer perceptron
MON	motor octane number
mot	motored, motor
NEDC	New European Driving Cycle
NN	neural network, neural networks
NO	nitric monoxide
nom.	nominal
NVH	noise-vibration-harshness
OBD	on-board diagnosis
ODE	ordinary differential equation
op.	operation
opt	optimum, optimal
OSC	oxygen storage capacity
pist	piston
pmep	pumping mean effective pressure
press.	pressure
prvap	prior to evaporation

quen .... quenching
rcm .... reduced charge motion
RDT .... Rapid distortion theory
res. .... residuals
RON .... research octane number
RPM .... revolutions per minute
RT .... real-time
SI .... spark ignited
SOI .... start of injection
spec .... specification
stoi, stoich. .... stoichiometric
SULEV .... Super Ultra Low Emission Vehicle (emission legislation)
TDC .... top dead center
TKE .... turbulent kinetic energy
tot .... total
Tu .... tumble number
turb. .... turbulence, turbulent, also turbine
U.S. .... United States of America
URANS .... unsteady Reynolds averaged Navier-Stokes equations
vap .... evaporation, vapor
vel. .... velocity
VL .... valve lift
vol. .... volumetric
voleff, vol.eff. .. volumetric efficiency
VVT .... variable valve train, sometimes BMW *Valvetronic*
w/o .... without

List of Figures

16

List of Tables

1 Introduction.

1.1 Motivation and goals of the work.

Development engineers of internal combustion engines face a further increase of conflicting goals regarding political, environmental and economical boundary conditions. For the solution of this optimization task, especially *engine calibration* plays a major

$\uparrow$ legislative limitations $\uparrow$
$\downarrow$ energy resources $\downarrow$

$\uparrow$ different vehicle variants $\uparrow$ $\uparrow$ system complexity $\uparrow$	*conflict of goals*	$\downarrow$ developing budgets $\downarrow$ $\downarrow$ developing times $\downarrow$

$\uparrow$ quality expectations $\uparrow$
$\downarrow$ life-long customer loyalty $\downarrow$
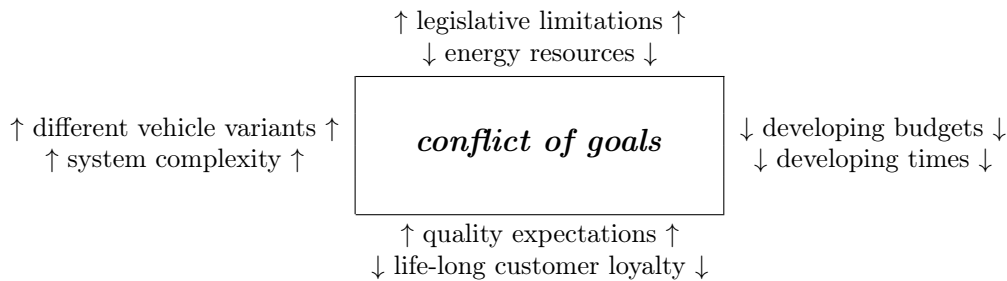
role. Thereby "calibration" of functions in the engine control unit (ECU) means a parameterization of data maps for optimal engine operation. The term *"virtual calibration"* thereby refers to the data acquisition via simulation methods instead of measurement. Nowadays, calibration processes get more complex due to the high degrees of freedom for new engine generations (in 2005 a typical SI ECU offered 5000 calibration labels whereas in 2012 this number has multiplied by 4, further increasing). Hence, simulation methods gain popularity in current projects and can also be applied to the development in series production issues. Physical modeling with ease in handling therefore promises best results and usability: Roithmeier [87, 88] showed calibration methods where one-dimensional engine simulations could predict the fresh air charge with high precision. Combining thermodynamics and turbulence from 3D CFD, Linse et al. [54, 55] demonstrated great benefits in the quasi-dimensional prediction of fuel burn rates.

Obviously, virtual calibration potentials may be boosted even further with reliable knowledge of the engine's combustion [27] because many ECU functions require a long, iterative and costly measurement process for good calibration.

In this work the derivation of a robust and simple but yet *physical combustion model for new SI engines* will accelerate engine calibration processes with enhanced simulation methods (compare figure 1.4). Hereby, some combustion related ECU functions shall be parameterized to prove industrial applicability.

1.2 State of the art – Current SI engine technology.

Within the foreseeable future, internal combustion engines will still play a central role for vehicle drive trains [111]. Here, especially spark ignited (SI) technologies haven't yet fully reached all their potential regarding high dynamics at low fuel consumption which results in further development of the whole power train and engine integration [43]. Also for new hybrid systems, the integrated SI engines must be optimized to gain the customer's acceptance.

Developing engineers face strict regulations regarding emissions, environmental sustainability and fuel efficiency on the one hand as well as partially contradicting customer demands on the other hand. This goal conflict can be summarized as aiming for *efficient dynamics* and it is tried to be resolved with several technical solutions. State-of-the-art systems involve turbo charging, variable valve trains and gasoline direct injection.

Exhaust gas turbo charging. Big SI engines suffer from low indicated efficiencies especially for customer relevant part load operation. The reasons are high gas exchange losses on the one hand and high friction losses on the other. To *increase overall efficiencies*, the coupling of an exhaust gas turbo charger to the engine's exhaust flow is practicable.

The cyclic feeding with burned gases transforms thermal and kinetic potential of the otherwise unused exhaust flow to rotational energy of the turbo charger. Therefore small volumes at the thermally insulated exhaust manifold support a better process conduct to the turbine. The amount of exhaust gas that flows over the turbine can be controlled by an actuated and variable waste gate opening which allows to only accelerate the turbo charger if needed.

The turbine's motion at the exhaust equally rotates the compressor at the intake side via a rigid shaft. On the fresh gas side together with a charge air cooler the cylinder charge density increases. Thus, a risen volumetric efficiency can achieve higher engine loads and extend the engine map in general.

The mentioned *load extension* can be used for a better fuel consumption due to a shift of engine operation on the trajectory of equal power output (going to more efficient higher loads and lower engine speeds). Moreover the friction efficiency can be boosted with a smaller aggregate which then doesn't lack power and maximum torque compared to bigger SI engines (*downsizing*, upgrading).

One has to mention the considerably higher exhaust back pressure which results from the changed manifold construction compared with naturally aspirated engines. To not corrupt the single gas exchange processes, the sub-division of consecutive ignited cylinders is performed as "twin scroll" exhaust manifold, compare figure 1.1 (left). Here, the exhaust gases are led out separately until they meet the sole turbine.

Further details on exhaust gas turbo charging and the effects on SI engine operation are to be found in literatures [18, 24, 99].

Fully variable valve trains. For conventional SI engines the load control works as quantity control on the mixture. This means that air charge differs for load variation and fuel masses are coupled to them by a fixed air-fuel ratio. Standard concepts thereby regulate the cylinder's air charge with a modulation of the throttle flap opening upstream to the intake. This reduces the intake manifold density for part load operation and the pressure drops below ambient pressure. Thus, the engine traps less fresh air but also has to work against this partial vacuum which causes throttling losses, also known as *"gas exchange losses"*.

Fully variable valve trains (VVT) improve the situation for part load. Therefore they offer *variable valve timing* on the exhaust and intake side as well as a fully *variable intake valve lift*. Seldomly, the exhaust valve lift is variable as well, which can satisfy the special needs of HCCI operation.

Fully variable valve trains relocate the throttling of the incoming air mass flow to the intake valve. The nominal (maximum) valve lift of a certain load point together with the timing of intake valve closure define the amount of trapped air for this working cycle. The throttle flap is only needed for emergency operation and for the definition of a small underpressure in the intake manifold which is not anymore gas exchange related (e.g. for crank train ventilation, fuel-tank venting). Together with an early valve closure (IVC) the small intake valve lift achieves a so called "gas spring" effect in the indicator diagram. This means that cylinder pressure nearly behaves adiabatically after IVC which results in reduced gas exchange losses and hence minimized part load fuel consumption for *unthrottled load control* [90, 91, 111].

The VVT construction offers the opportunity for an internal fluent gas recirculation. The very early or very late exhaust valve closure allows to control the burned mass fractions in the cylinder. It is known that inhibitant components minimize nitric oxides and improve the degree of dethrottling.

Here again it may be considered, that smaller valve lifts at the intake considerably change the flow field characteristics in the cylinder. This may be positive for mixture formation due to high gas velocities over the valve which can help the fuel spray break up and homogenization. On the other hand, it could be shown that combustion relevant turbulence must be enhanced with improvement of induced charge motion [18, 43].

A wider scope on all issues of fully variable valve trains can be found in literatures [18, 42, 89].

Gasoline direct injection. SI engines with fuel direct injection share properties of an *inner mixture formation*. Therefore, the fuel is directly given to the cylinder charge but comparably earlier than in compression ignition engines. For SI operation, the main fuel fraction is injected into the intake stroke when the valves are still open. This helps a better vaporization and mixture of fuel and fresh air and is possible even for high engine speeds, when available time spans are quite short.

There can be found three different forms of fuel direct injection which are "wall guided", "air guided" and *"spray guided"*. The spray guidance is technically the most complex solution but shows little piston/wall contact (reduction of hydro carbon emissions) and is more independent from surrounding global flow formations than "air guided" methods [99].

Regarding air-fuel ratios of gasoline direct injections (GDI), there are established stratified/lean and *homogeneous/stoichiometric* concepts. Though lean engine operation promises better fuel consumptions for part load, it lacks the ability of world wide distribution. In many countries the fuel quality is rather low and the special catalytic conversion system for lean combustion cannot cope with induced poisoning. Moreover the rich operated release of nitric oxides from the special storage catalyst reduces possible saving potentials of the system. Hence, for reaching world wide emission regulations with only one construction, the GDI concept must be chosen to be operated at $\lambda = 1$ in homogeneous mode, so standard three-way catalyst technology is at use. Stoichiometry must only be left at high engine loads/high speeds for temperature regulation on the outlet (component overheat protection).

State of the art GDI systems share a common rail connected to all injectors. This has the advantage that high pressure availability is decoupled from the injection timing. These systems are then quite flexible in operation. For a variable number of partial injections in the working cycle the different crank angles of injection start (SOI) can be nearly freely defined, considering the injector's opening behavior and an optimal mixture formation. Moreover the feeding rail pressure is responsible for a good spray break up, spray penetration depths into the cylinder and the maximum amount of insertable fuel at a fixed time span. Here, the mentioned high degrees of freedom still leave potential for a multi-criteria optimization of the engine process [112].

Summarizing the advantages of fuel direct injection for SI engines are

- cylinder charge cooling via the fuel's heat of vaporization, causing
    - a density drop in the cylinder and a higher intake mass flow (theoretically 9% more air mass at $\lambda = 1$ compared to port injection [99])
    - a temperature drop improving knock limits at full load. This can be used to increase the compression ratio $\Delta \epsilon \approx 1.5 - 2$ (theoretical potential of 5% fuel savior at part load [44]).

- a better agility (torque supply) compared to port injection systems because no fuel mass must be slowly vaporized from the manifold walls first.

- improved cold start behavior and thus potential for good emission levels because in-cylinder fuel vaporization boundaries are better than in the cold intake manifold.

For further comments on system components, GDI operation etc. the reader is advised to consult literatures [76, 99].

24

System combination: BMW TwinPower Turbo   To achieve the overall goals of global CO_2 reduction at high dynamics of the SI engine power train, there are two ways

1. optimization of fuel consumption and

2. operating the engine in fuel efficient map regions.

Together with optimizations of the gear box design and vehicle boundaries, the BMW Group combines the advantages of an exhaust gas turbo charger, a fully variable valve train and a homogeneous/stoichiometric gasoline direct injection for their new generation SI engines, compare figure 1.1. This section shall shortly describe special features of
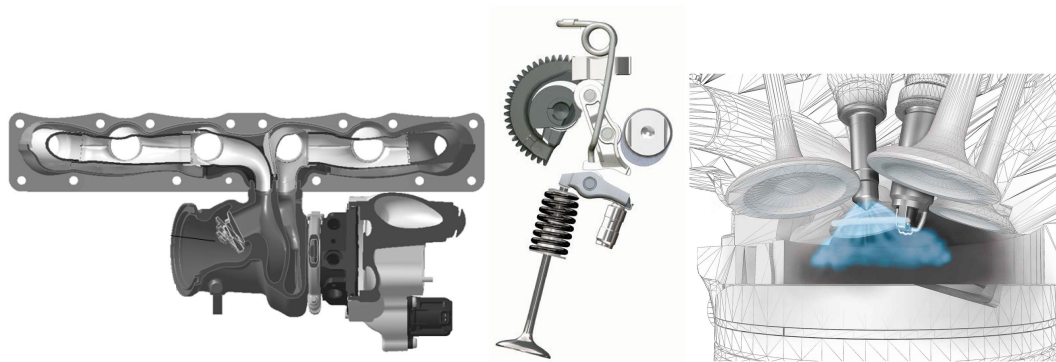
Figure 1.1: *BMW TwinPower Turbo system* – sample twin scroll exhaust manifold with variable waste gate for the turbo charger (left), schematic fully variable valve train *BMW Valvetronic* (middle) and homogeneous gasoline direct injection (right). Sources: BMW Group

the *BMW TwinPower Turbo* system that are relevant for the aimed combustion model. The *twin scroll turbo charger* is directly exposed to pressure pulses and therefore uses also the exhaust's kinetic energy. To improve dynamics of turbine acceleration at low engine speeds (*low end torque*), the engine is operated at high valve overlap and positive pressure gradient from intake to exhaust manifold. This "scavenging" can only be performed because a later direct injection doesn't spill fuel to the exhaust. Hence, residuals are pressed out of the cylinder, the trapped air charge is maximized and the turbine speed increases by a higher mass flow than just the exhaust gas flow. Concluding, the aggregate can supply a higher torque at low engine speed and the vehicle's total gear ratio can be adapted for optimum fuel consumption. With this concept, an SI engine can deliver high Diesel like torque levels over a wide range of the engine map but outperform the Diesel's specific power output enormously. Actual serial production engines with *BMW TwinPower Turbo* combination allow an output

of around 90kW/Litre and 175Nm/Litre of cylinder displacement.

The *BMW Valvetronic* system realizes the cam timing shift with hydraulic components and the differing intake valve lift with a mechanical engagement at the intake-cam-intake-valve connection, compare figure 1.1 (middle). It has to be considered that a smaller intake valve lift in contrast to other systems here combines with a shorter intake duration. This VVT system may achieve up to 12% fuel savior compared to SI engines without any variability [43]. It was already mentioned that a variable intake valve lift requires a higher level of air charge motion to keep up the combustion efficiency. The same fact accounts also for highly charged engine loads, where the burning duration must not considerably exceed the optimum process limits. The BMW Valvetronic achieves a modulation of entering air charge motion via *valve phasing* and *intake masking*, compare figure 1.2. The valve phasing opens up the single intake valves of a
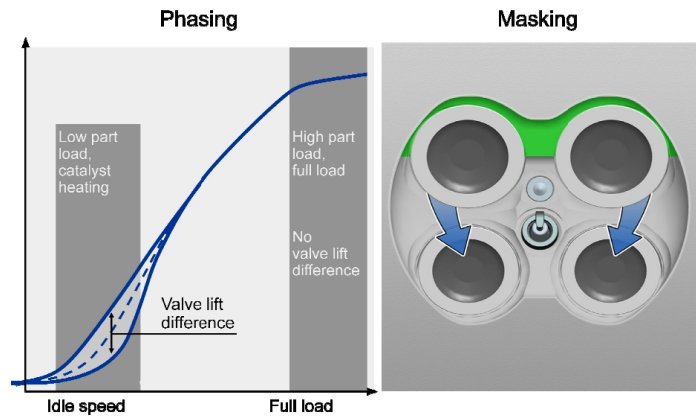
Figure 1.2: *BMW Valvetronic* modulation of the entering gas flow at small valve lift. Valve phasing (left) causes air swirl motion due to different valve lifts. Intake masking (right) induces air tumbling motion due to asymmetric mass flows over the valve seat. Sources: BMW Group

cylinder at different heights, thus provoking a swirl motion driven by entering mass flow differences. Extreme phasing (valve lift difference) accounts for small valve lifts but both intake valve curves assimilate for maximum load. Hence, swirl motion vanishes at full lift. The partial mechanical machining of the valve seat area influences the symmetry of the flow and is called "intake masking". Here, the rear part of the seat is shadowed for small valve lifts and the bulk mass enters over the front part, inducing a greater tumble motion. This effect is especially important for early intake valve closure, where tumble motion is normally cut before it can establish. Together, swirl and tumble motion at small valve lifts improve turbulence at ignition timing (possibly later ignition with better combustion efficiency), lower sensitivity for residuals and enhance mixture

26

homogeneity.

The used common rail system can produce a high pressure of up to 200bar for high precision fuel injection. It combines robust solenoid fuel valves that are centrally located to the spark plug. The injectors are cross directionally displaced to the engine's centre line. This helps the spray guided mixture formation to profit directly from instantaneous intake turbulence and induced tumble motion will drift the fuel clouding to the spark location, thus assuring good ignition conditions.

The direct injection cooling helps the *BMW TwinPower Turbo* concept to work at an comparably high compression ratio of $\epsilon = 10$. Increased inner efficiencies of the combustion process thereby decrease the exhaust gas temperature (energy balance), which rectifies the trade-off between high engine output in the maximum power region and the needed exhaust cooling via rich operation.

In summary, the combination of *BMW Valvetronic*, fuel direct injection and late ignition timings has the technical potential to fulfill even the U.S. classification of "Super Ultra Low Emission Vehicle" emission standards (SULEV) [43]. Several papers on the serial production and combustion process of *BMW TwinPower Turbo* are published already [43, 50, 51].

In this work, the in-line 4 cylinder *BMW N20B20* engine with *BMW TwinPower Turbo* stands as example for combustion modeling of complex new generation SI engines, see details in appendix A.

Variability of modern SI engines. The previously mentioned combination of exhaust gas turbo charging, fully variable valve train and gasoline direct injection offers a wide range of variability for every engine operation point. For each set of engine parameters (e.g. boost pressure, intake valve lift, fuel injection timing etc.), there exists a corresponding combination of "inner cylinder states". Thus, the prediction of combustion burn rates becomes quite complex, due to widely differing influences on the burning velocities, compare figure 1.4. In the following, table 1.1 summarizes the physical variability of "inner cylinder states" in modern SI engine systems for the example *BMW N20B20* engine.

With emphasis on the variable *ignition timing*, this leads to potential *burning velocities* with $s_L = 0.4m/s$ (lower part load) up to $1.1m/s$ (full load) and the turbulent counter part $s_T = 0.7m/s$ (part load, low engine speed and small intake valve lift) up to $1.6m/s$ (at nominal power output). It must be noted, that peak values of s_L and s_T are reached along the engine cycle together with high cylinder gas temperatures.

Summarizing, there are complex requirements for combustion modeling, because influencing physical quantities are constantly changing in the engine cycle. The accuracy of those inputs defines the quality of predictions, thus thermodynamics and turbulence has to be given special recognition in advance, compare sections 2 and 3.

quantity	unit	range at ignition	.. caused by
pressure	[bar]	2 .. 45	engine load control
temperature	[K]	500 .. 800	load control, residuals, fuel injection
residual fraction	[-]	0.01 .. 0.25	exhaust/intake valve timing
air-fuel ratio λ	[-]	0.75 .. 1.05	direct injection strategy
turbulence level	[m^2/s^2]	5 .. 450	engine speed, valve train calibration

Table 1.1: Variation of "inner cylinder states" within the engine map for the BMW N20B20 engine. Named quantities impact on the turbulent flame propagation.

1.3 State of the art − Simulation methods for virtual engine calibration.

Technical simulation procedures generally aim to reproduce or predict the system's behavior with regard to certain characteristics. Thereby, models are an abstraction (the degree depends on model compexity) and can be employed to learn about real systems. For virtual engine calibration, ECU relevant system behavior shall be derived from a virtual image of the engine itself. Roithmeier [87] could show that for engine simulations, the preferred model types are physically based including a medium up to high level of detail. *Physically based* stands for reduced empiricism in this context. Thus, acceptable modeling efforts call for "grey-box modeling" where important behavior is represented by physical equations (only minor influences are parameterized for model *tuning* purposes).

State of the art modeling types are summarized in table 1.2. They are distinguished

model type	granularity	factor to RT	typical application
non-dimensional	low	1 (real-time)	RT neural network m
0D	medium	50-100	combustion m/a
1D	medium-high	100-1000	gas exchange m/a
3D CFD	very high	10000+	flow field / combustion m

Table 1.2: State of the art modeling of engine related processes and feasible applications. Here, *granularity* is a measure for the level of detail. (RT=real-time, m=modeling, a=analysis)

by their degree of spatial resolution. While *neural networks* are non-dimensional (they neither consider absolute coordinates nor time scales of the guiding process), they can be only obliged to review integral states without physical knowledge. They are especially capable for fast calculations of the ECU or other real-time systems, because

the mathematical algorithms behind them are rather simple. Also polynomial models and data retrieval from stored maps can be seen as non-dimensional. Their bad ability to extrapolate requires high training efforts to keep all simulation results within known model ranges.

Zero-dimensional (0D) models can be assigned state variables that describe the system status (e.g. thermodynamic volume, turbulent length scale). The qualities are assumed to be time dependent but homogeneous in the system boundaries which describes the model class as being *"quasi-dimensional"*. The greater the individual systems are, the worse gets the quality of a single-zone 0D approach. Hence, for thermodynamic calculations the determination of user-defined zones (burned zone, unburned zone, liquid fuel zone, vaporized fuel zone etc.) with equal inner properties are state of the art. Every zone itself can then be evaluated with according physical description. The mentioned zonal modularity and the simpleness of the spatial resolution at physically based nature, helps this model class to be state of the art for thermodynamic analysis, heat release analysis and also fast burn rate prediction.

One-dimensional (1D) models are able to differentiate the calculated quantities along one spatial direction. Here, the solved equations are depending on time and one coordinate, which makes them handy for acoustic and wave related problems. The implementation of continuity, momentum and energy equations again leads to a jump of processing times compared to simpler model classes. The still reasonable effort for calculation justifies the nowadays broad application of *1D models* for all wave propagation related engine phenomena (e.g. in hydraulic systems, mechanical damping problems and *especially engine intake and exhaust flow processes without heat release*).

Multi-dimensional models (3D) resolve all quantities in every spatial direction. These computational fluid dynamics (CFD) methods are theoretically able to compute thermodynamics and turbulence at every single location of the engine. In practical use, due to missing computing capacities, the use of a direct numerical simulation (DNS) is often restricted to very small areas of interest and short time spans. Thus, large eddy approaches (LES) become more frequent [34] whereas solving averaged Navier-Stokes equations (URANS) is still most common. Here, the computational grids for in-cylinder problems are coarse-meshed but too wide to resolve all physical processes as in DNS. Part of the physics must be modeled (sub grid models). Multi-dimensional models allow to evaluate the complex interaction of fluid mechanics and depending reaction kinetics. But in general, comparably long processing times and extensive expert knowledge still prevent calibration engineers to use 3D CFD methods for data generation of their ECU functions.

In summary, only low-dimensional models remain as practical alternative to simulate a complete range of widely spread engine variability. Aiming at a rather broad than detailed simulation depth, only simple model types can accomplish the processing in realistic developing time spans. Even so, in this work the simplified 3D analysis of turbulence closes the gap between complex and accurate CFD and fast but low-dimensional

29

simulation methods.

Many authors address the simulation of engine processes with different backgrounds and objectives in their works [21, 33, 60, 71, 84, 97]. Some of them will be discussed in the following.

Low-dimensional combustion models.   When it comes to industrial applications and a complete engine map exploration, the low-dimensional combustion prediction is either of non-dimensional or 0D (quasi-dimensional) quality. Typically there are distinguished two major model classes:

1. empirical models – contain observed system knowledge as integral formulation

2. phenomenological models – contain partially the physics of major contributing processes

Classical *Vibe* function (also *Wiebe*) aims to reproduce the heat release in internal combustion engines with static mathematical methods. The parametrical functions are derived from *empirical* knowledge and were first introduced in 1970 [60, 108]. Up to today, Vibe's empirical approach is still popular in cases where a non-predictive combustion is sufficient for appropriate simulation quality [88] or processing times are most important.

Simulation tasks must recover changes in the combustion process for varying boundary conditions and can be furthermore derived from Vibe's functions. Therefore, its defining parameters are changed due to the current engine operation. The authors Milocco [63] and Barba [4] established *semi-empirical* models for certain engine concepts from extensive measurement data bases. They were able to widely extract Vibe parameters and feed them into neural networks which can later be used for interpolation of a given engine operation. This method shows a high repeatability and accuracy but requires very high experimental efforts at the same time. Hence, these models are not precisely predicting but recapitulating combustion processes.

Other authors directly regarded single parts of the combustion process and correlated them to physical phenomena. Csallner [12], Hockel [40], Theissen [106] and Witt [115] investigated the change of thermodynamics and turbulence and observed e.g. the impact on ignition delay times. Figure 1.3 plots their methods for the *BMW N20B20* engine varying the operation point *swirl 1* (cf. table 3.2) independently once in resdiual fraction (left) and once in engine speed (right). Therefore, a reference point of engine operation is used for each model and one-by-one variations of expected main parameters of combustion are performed. After again defining best-fit Vibe functions, a produced parameter set more or less physically quantifies essential influences. Compared to other methods, the authors arrange predictability from observed physics instead of only engine actuation, which rises the level of physical knowledge. Yet, these models
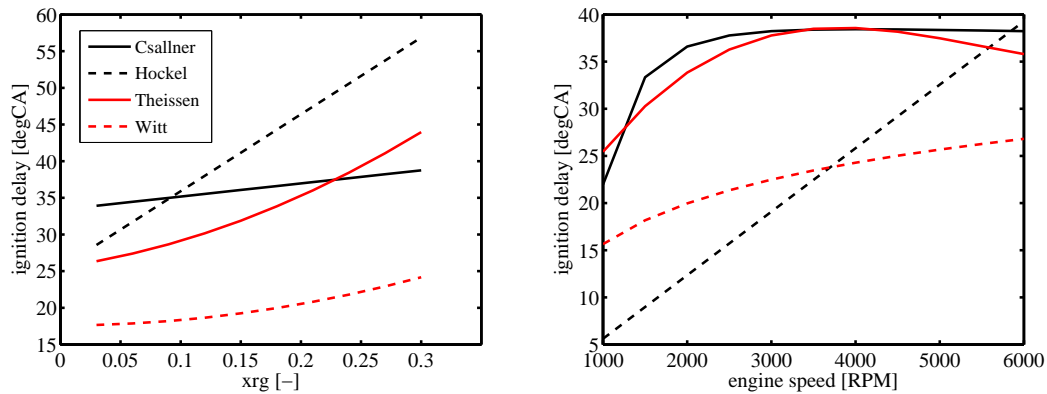
Figure 1.3: Example reaction of semi-empirical combustion predictions from differing authors, which are all based on Vibe's approach. The increase of residual fractions (left) extends ignition delay, whereas the engine speed shows quite contradicting results (right) for the variation of *swirl 1*.

are semi-empirical and differ very much for new engine constructions, compare figure 1.3. Concluding, extrapolation abilities can only be achieved with physical modeling.

Phenomenological 0D/1D models derive physical descriptions for the dominating processes of the heat release. Thus, it is not aimed to model all occurring dynamics in detail, but to capture the most relevant physics. (The entrainment model, the flamelet model, the fractal model, the eddy-break-up model and the eddy-dissipation model are typical phenomenological combustion approaches for different application ranges.) This model class seems most useful for the defined requirements of *virtual engine calibration*:

- physical basis

- little fine-tuning efforts

- little risks in extrapolation

- fast computation times

- simple application

- high usability/modularity for different combustion related simulation tasks

Phenomenological models with one-zone combustion are so called "thermodynamic models". They don't distinguish pressure, temperature and gas composition locally and thus assume a perfectly mixed stirring reactor. They cannot calculate pollutant

formations [102] but still these approaches are precious to gain a fast overview on complex systems where the SI engine only plays a contributing role e.g. large-scale gas power plants.

The *0D entrainment approach* is a multi-zone combustion model, which could prove its excellent applicability several times [3, 31, 68]. But yet there is no compilation available that can handle the complexity of all SI engine technologies combined and derive ECU calibration data from simulation results. The high amount of variability in a BMW TwinPower Turbo concept still lacks accurate simulation of all needed quantities.

Hence, the current work closes the gap between *accurate thermodynamics* in the whole engine map, physical *turbulence production* in a complex VVT system, *predictive ignition delay* modeling and the calculation of the consecutive heat release. The identification of turbulent burning velocities in the cylinder is essential. At the very end, the targeted 0D combustion simulation shall be employed for correct ECU calibration. This requires reproducing the physics in the whole model development process.

Figure 1.4 shows a flow chart of signals that are processed by the entrainment model structure. On the left side all relevant engine parameters are put into the calculation
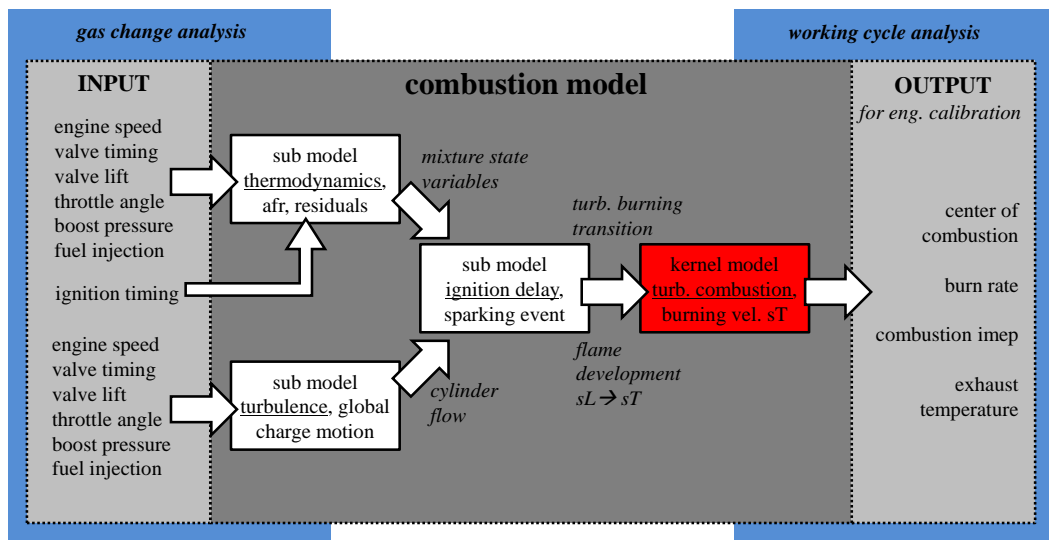
Figure 1.4: "Big picture" for physical combustion modeling of modern SI engines.

and moreover also processed by a gas exchange analysis. In the middle of figure 1.4, the thermodynamic evaluation together with the turbulent boundaries are combined and serve as input for an ignition delay model as well as a turbulent flame classification (red). The crank angle resolved output of the model structure can be seen on the right hand side, which will be evaluated in cooperation with a working cycle analysis tool.

32

The underlying work aims at developing a combustion model for complex SI engines and consists of the following parts:

- chapter 2: thermodynamic modeling to provide the inputs to the laminar burning velocity

- chapter 3: quasi-dimensional modeling of turbulence and global charge motion to provide additional inputs to the turbulent burning velocity

- chapter 4: physical modeling of ignition delay for a quasi-dimensional estimation of the beginning combustion process

- chapter 5: combustion modeling based on an entrainment approach to capture the burn-out phase of the combustion process

- chapter 6: virtual engine calibration considering engine torque production and the exhaust gas temperature

2 Thermodynamic modeling with real-time capability.

Preface for thermodynamic modeling. This section introduces the derivation of a real-time (RT) capable model structure, providing the in-cylinder quantities pressure, temperature, residual fraction and air-fuel ratio as input to the laminar burning velocity s_L. Parts of the discussed physical model refer to the diploma theses of Koppes [47] and Mühlbauer [62], which I supervised during my time as doctoral candidate. Chapter excerpts were published previously [28].

2.1 Introduction.

A physical prediction of burn rates within a BMW TwinPower Turbo engine requires an estimation of turbulent flame propagation. Common approaches [74] for turbulent burning velocities involve the local interaction of a flame with turbulent structures. Based on a flamelet approach and with a laminar flame in mind there can occur wrinkling, corrugation and a change in flame topology via turbulent influences, see e.g. the classification of propagation behavior according to the Peters-Borghi diagram [74]. Therefore, it seems evident that all traditional evaluations of turbulent burning velocities need a comparison with laminar flame conditions. Hence, the laminar flame speed is a significant input to the targeted combustion model. It describes the propagation rate of a laminar premixed flame front into a resting unburnt gas zone [61]. The laminar flame speed depends on system pressure, unburnt temperatures, air-fuel ratio and residual gas mass fraction [60]. The laminar flame speed data for iso-octane used in this study is based on Ewald [20], which includes exhaust gas ratios up to 30%. (The data base was originally compiled by 1D flame simulations where results for important quantities such as flame speed were stored.)

2.1.1 Sensitivity analysis.

Regarding an accurate prediction of burn rates within the whole engine operation map, variations showed that the combustion stages of 5% and 50% burned mass fraction must be calculated precisely. Thus, it could be shown that the laminar flame speed estimations must fall below a relative deviation of $\pm 5\%$. When relying on the physical determination of laminar flame speed s_L based on Ewald [20] the greatest uncertainties evolve from the vector of input parameters: pressure, unburned temperature and

residual gas mass fraction. Air-fuel ratio can be seen as variable dimension for engine calibration purposes and it is not directly considered in sensitivity calculus. Figure 2.1 shows the physical sensitivity of the laminar flame speed for isooctane and the maximum bandwidth of $\pm 5\%$. The results were plotted with reference to six different
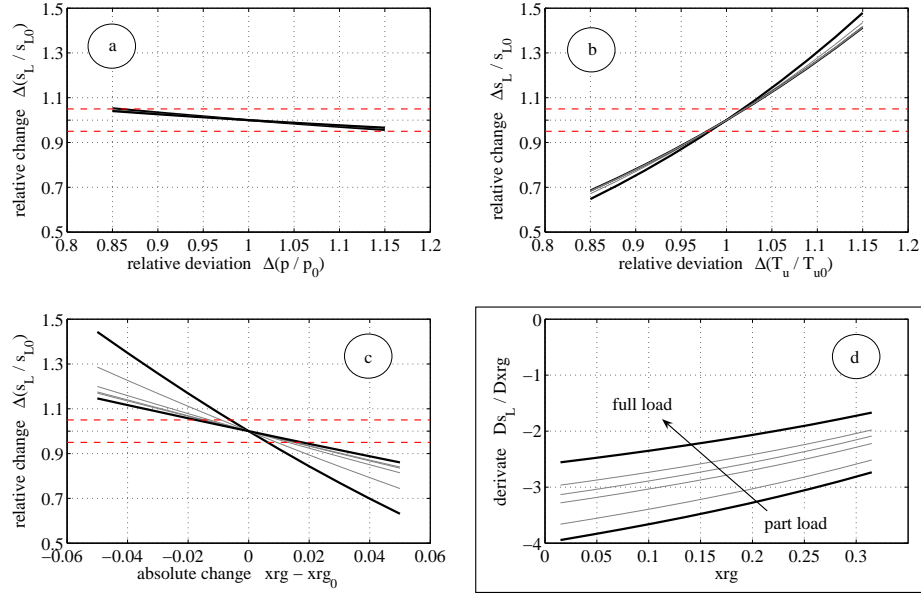
Figure 2.1: Physical response of the laminar flame speed s_L on deviations of pressure p (a), temperature T_u (b), residual fraction x_{rg} (c) and sensitivity to global load change (d). Subscript "0" relates to a reference operating point.

thermodynamic states at ignition timing, spread within the engine map of the *BMW N20B20* aggregate, compare appendix A and C.1. Therefore deviations of the input vector (caused by possible inaccuracies of the thermodynamic model) were implied with "one-by-one" variations. For these variations, it was assumed that the laminar flame speed model is without error, so that possible failures in resulting burn rates cannot be considered. In summary, the laminar flame speed shows a weak response to pressure deviations and a strong sensitivity to temperature and residual fraction. Moreover the decline of the flame speed is highest for part load engine operations and midrange residual fractions. These physical observations state that temperature and residual fractions must be determined very accurately especially at low engine load. Up to that conclusion all experiments were conducted without a realistic interaction between cylinder pressure, temperature and gas composition at engine operation. Hot residuals

relative change $\Delta(s_L / s_{L0})$

1.3
1.2
1.1
1
0.9
0.8
0.7

- · - · w/o temperature effect
——— with temperature effect

0.6 0.7 0.8 0.9 1 1.1 1.2 1.3 1.4

relative deviation $\Delta(xrg / xrg_0)$
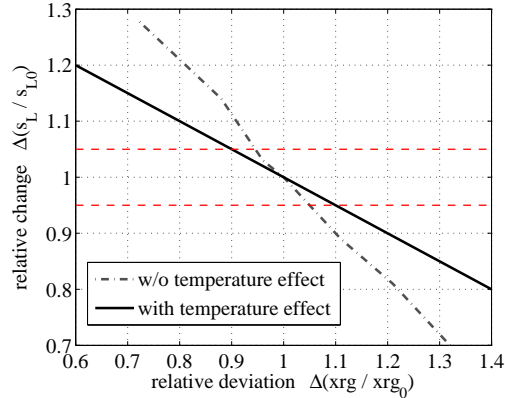
Figure 2.2: Response of the laminar flame speed s_L on deviations of residual fraction x_{rg} with respect to realistic engine behavior. Subscript "0" relates to a reference operating point.

from the last burning cycle have a big impact on global temperature levels before and after ignition. Therefore, it is feasible to examine the effects that a change of residual fraction has on temperature and consequently on the laminar flame speed. Keeping in mind that a higher dilution slows down the flame but increases the mean cylinder temperature, figure 2.2 shows the sensitivity for a part load operation at 2000RPM and *bmep* 2bar (cf. appendix C.2, VVT). The combined effect with a temperature rise relaxes accuracy requirements for the thermodynamic modeling. The dilution sensitivity in real engine applications is weaker than regarded without temperature rise. Following a detailed analysis of unthrottled engine operation [47] at the *BMW N20B20* engine, final accuracy requirements for a modeling of laminar flame speed can be derived using data from figures 2.1 and 2.2 and are give in table 2.1.

The named boundary conditions have now to be provided by the upcoming thermody-

quantity	unit	quality
pressure	[bar]	$\pm 5\%$
temperature	[K]	$\pm 4\%$
residual fraction	[-]	$\pm 10\%$

Table 2.1: Aimed accuracy corridor for thermodynamic outputs [47].

namic analysis.

2.1.2 Prerequisites for complex thermodynamic modeling.

Current BMW engines actually combine multiple technologies aiming at improved consumption and pollutant reduction. Some of them have become state-of-the-art such as direct injection, others are BMW specific such as fully variable intake valve lift. Thus, the interaction of various effects must be considered in the simulation:

- Boost pressure, variable intake valve lift and cam timing are main influences to trapped air charge, compare section 2.3.3.

- The intake manifold pressure is nearly independent from air charge demand for part load (variable intake valve lift operation works unthrottled).

- Variable exhaust cam timing are accounting for trapped residual masses.

- Variable overlap areas between intake and exhaust valves affect the degree of cylinder scavenging, compare equation 2.10.

- Fuel direct injection causes a temperature drop depending on GDI parameters and fuel properties, compare section 2.4.

- The air-fuel ratio (afr) changes polytropic behavior in the compression stroke, compare equation 2.6.

Figure 2.3 shows that ignition timing influences significantly the laminar flame speed (up to a factor of 2.5 between early and late ignition). Thus, the thermodynamic model interprets all state variables at a constant reference crank angle for better comparison.

2.2 Simulation of engine thermodynamics.

2.2.1 Governing physics.

The first law of thermodynamics for open systems is formulated for engines as follows in equation 2.1. All mass flows are calculated, following the downstream gas motion from air inlet to exhaust muffler, thus at least establishing a one-dimensional problem.

$$-\frac{pdV}{d\alpha} + \frac{dQ_{comb}}{d\alpha} - \frac{dQ_{httr}}{d\alpha} + h_{int}\frac{dm_{int}}{d\alpha} - h_{exh}\frac{dm_{exh}}{d\alpha} - h_{bb}\frac{dm_{bb}}{d\alpha} = \frac{dU}{d\alpha} \qquad (2.1)$$

Therefore pdV considers volumetric work, dQ_{comb} quantifies the combustion heat and dQ_{httr} calculates the wall heat transfer from the cylinder gas. The terms $h_x \cdot dm_x$ sum up all enthalpy flows via the system's boundaries (index int over the intake valves, exh over the exhaust valves and bb as blow by between piston and liner). Depending on their flow direction, a negative sign indicates that the enthalpy leaves the system, whereas a positive sign indicates an entering enthalpy flow. All mentioned terms contribute to
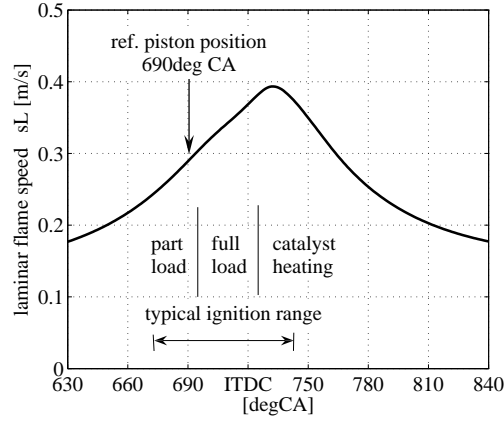
Figure 2.3: Effective laminar flame speed for 2000RPM, *bmep* 2bar with x_{rg} 17%. Reference crank angle at 690degCA eases comparability with different ignition timings.

the change of internal energy dU in the system.

Furthermore the ideal gas law in equation 2.2 requires the knowledge of the working fluid's mixture gas constants.

$$p \cdot V = m \cdot R \cdot T \tag{2.2}$$

They vary with its composition as well as cylinder temperature and pressure, which can be found in the differential form of equation 2.3. Whilst the original demand was a resolution of the thermodynamic state, now there is uncovered an implicit link between thermodynamic state variables and thermo physical properties like enthalpy and internal energy.

$$p\frac{dV}{d\alpha} + \frac{dp}{d\alpha}V = mR\frac{dT}{d\alpha} + m\frac{dR}{d\alpha}T + \frac{dm}{d\alpha}RT \tag{2.3}$$

Closing the basic equation set, mass conservation is adopted for all discrete modules. Due to high relevance in engine thermodynamics, the heat loss term dQ_{httr} from equation 2.1 shall be explained in more detail. Common approaches sum up convective and radiant heat transfer, which is often written in Newtonian form [60].

$$dQ_{httr} = dQ_{\alpha} + dQ_{\epsilon} \approx \sum_{i} \alpha_i \cdot A_i \cdot (T_{wall} - T_{gas}) \tag{2.4}$$

The summation considers effective areas of convection for cylinder liner, cylinder head and piston in A_i. For evaluation of equation 2.4, a temperature gradient must be

assumed. Especially the heat transfer coefficient α_i is rather complicated to determine. There exist a variety of semi-empirical approaches, that have their origin in dimension analysis for flow field and temperature boundary layers. The applied heat transfer coefficients in this work were introduced by Woschni in 1970 [116] and by Bargende in 1990 [6]. A closer look on the derivation of heat transfer coefficients can be found in [6, 9, 19, 65, 79, 116] and a recent study of Frommater [22] which compares state of the art approaches considering their applicability for new engine generations.

2.2.2 1D GT Power instrumentation.

In the following, GT Power (Gamma Technologies) is used for thermodynamic engine simulation. Commonly there are system models available even for early development stages. Roithmeier [88] enabled GT Power to predict the fresh air charge for a calibration of RT ECU functions. Njis [69] later on reevaluated ECU air charge results with reference simulations. Table 2.2 shows in a qualitative manner that an adjusted detailed full engine simulation can predict thermodynamic states precisely.

Summarizing, parallel *GT Power detailed full engine simulations* on computer cluster

method	adjusted accuracy	calculation speed	prediction quality
engine test bed & gas change analysis	*reference*	$--$	*reference*
focus: GT Power detailed engine model	$++$	$-$	$+$
GT Power non-predictive map model	$+$	$++$	$--$

Table 2.2: Qualitative comparison of different methods for thermodynamic modeling with focusing for this work.

units achieve an overall time cut of 50%+ compared with test bed measurements, which is very important when a high number of evaluations is needed (several thousand operation points for air charge purposes). Hence, this calculation method shall be focussed for the build up of a thermodynamic model, which then subdivides into the following steps:

- Designing an RT environment for thermodynamic quantities (cf. section 2.3.1)

- Building up a full engine simulation and adjusting it by a small number of test bed measurements (cf. section 2.3.2).

- Setting up several cases covering all engine operating points with consequent computation on parallel cluster infrastructure (cf. section 2.3.3).

- Transfer GT Power results into RT model structure and ensuring quality of results (cf. section 2.3.4).

The above process combines the advantages of a full engine calculation (accuracy and overall effort) with the calculation speed of a standalone RT structure. The construction of a GT Power full engine simulation model for the *BMW N20B20* can be seen in figure 2.4. Therefore all important engine parts are projected back to their influences
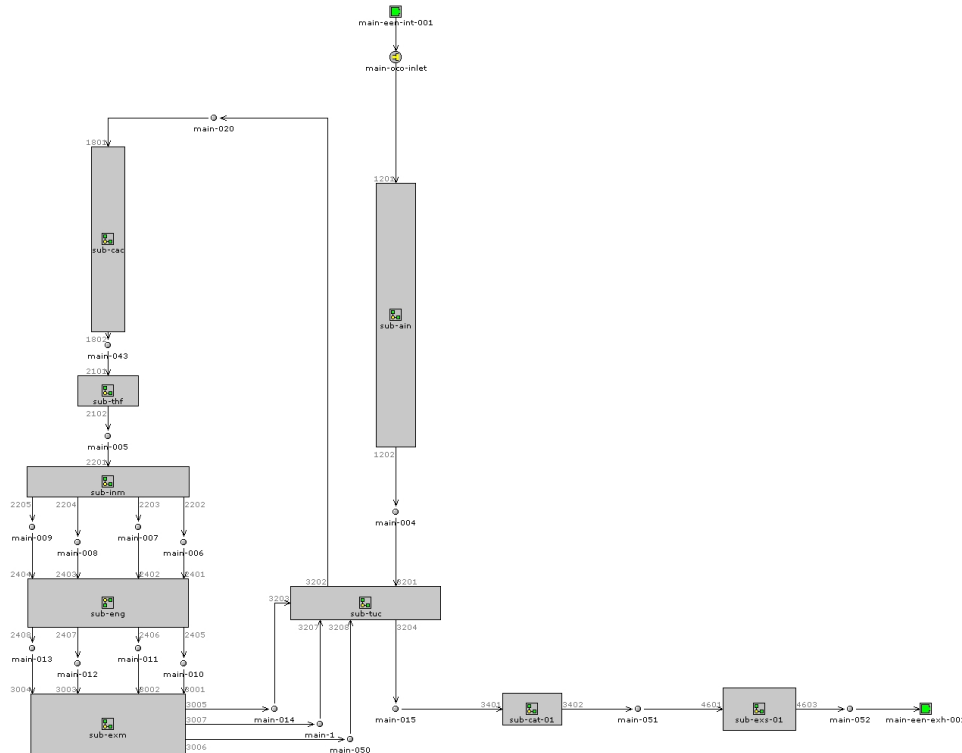
Figure 2.4: GT Power model structure for the BMW N20B20 engine. (*ain*=air intake coupled to environment, *tuc*=turbine and compressor, *cac*=charge air cooler, *thf*=throttle flap, *inm*=intake manifold, *eng*=thermodynamic basic engine model, *exm*=exhaust manifold, *cat*=catalyst, *exs*=exhaust system coupled to environment)

in the operation process (e.g. a fuel injector works on air-fuel ratio, spray evaporation, instantaneous turbulence etc.).

2.3 Systematic thermodynamic calculation in real-time.

2.3.1 Construction of the real-time setup.

Basing on the BMW function for air charge determination, the aimed approach contains a utilization of neural networks (NN) like in the ECU - their configuration can be re-read in section 2.3.4. The networks are linked and interact with each other [64]. These NN structures seem beneficial and robust because they are RT capable (calculation sometimes below 5msec depending on the amount of operations in one run), they easily represent complex nonlinearities and can be employed to interpolate and to a minor extent extrapolate results without deeper physical knowledge. Figure 2.5 shows the structure for BMW TwinPower Turbo thermodynamics with exhaust gas turbo charger, variable valve train and gasoline direct injection. The model parts are repeatedly
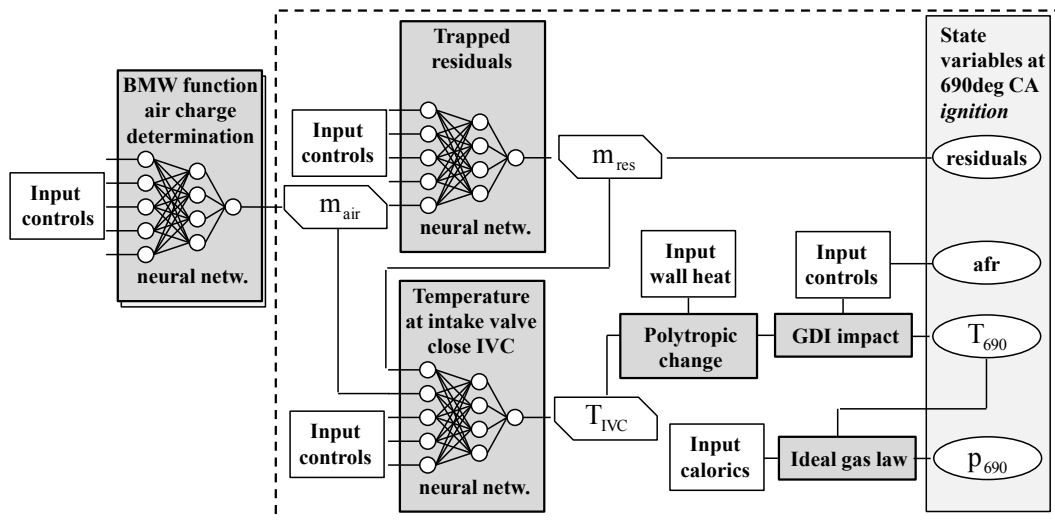
Figure 2.5: Flow chart design for real-time thermodynamic modeling of a new BMW Group SI engine. The linkage of several NN and fast calculations (dark) results in an output of state variables near ignition top dead center (ellipses). The dashed environment distinguishes all innovative structures of the model. Vectors qualifying input controls are similar.

stimulated by the vector "Input controls". This vector combines operation parameters (engine speed, boost pressure, intake manifold pressure and temperature) together with actuated engine variables (intake cam timing, intake valve lift, exhaust cam timing). The structure in figure 2.5 contains the original BMW function for air charge determination,

which supplies the cylinder's trapped air mass for all other calculations. The following NN for residuals considers an internal feedback between trapped air mass and trapped residuals. Together with a recent air-fuel ratio (afr), the cylinder contents at intake valve closure (IVC) are sufficiently known. Temperatures at IVC can be calculated with a correlation of residuals and fresh air fractions in the last neural net. This modular isolation in the determination of temperature and residuals allows making use of effects explained in section 2.1.1. Consequently following the temperature path in equation (2.5), the changes during compression are described by a polytropic change.

$$T_* = T_{IVC} \left(\frac{V_*}{V_{IVC}} \right)^{n-1} \tag{2.5}$$

Here the polytropic exponent n can be modeled easiest regarding the cylinder air-fuel ratio. Bracketed values in equation 2.6 are adjusted by few test bed measurements for the concerning engine. (Polytropic errors could be even minimized when engine speed and engine load effects on wall heat transfer are observed. Sample values for n can be found in Mühlbauer [62] and range between 1.3 for rich mixture and 1.33 for stoichiometric operation. Here, the increased influences of heat transfer rates can be seen, since older publications estimate the polytropic coefficient higher.)

$$n = [slope] \cdot \text{afr} + [offset] \tag{2.6}$$

Until now the cylinder temperature decrease caused by fuel evaporation was not resolved. The specific direct injection effect (GDI) in figure 2.5 is modeled as offset on the polytropic temperature value. The underlying physics are explained in section 2.4.1. The pressure at ignition is derived from the ideal gas law. Mixture composition impacts on the specific gas constant in equation 2.7, where x_i stands for mass fractions of component i.

$$R_{mixt} = x_{air}R_{air} + x_{fuel}R_{fuel} + x_{rg}R_{rg} \tag{2.7}$$

Together with air-fuel ratio as parameter, the model in figure 2.5 can predict cylinder thermodynamic states in RT for the evaluation of the laminar flame speed at ignition.

2.3.2 Calibration of the GT Power model.

From figure 2.5, it is evident, that the correct estimation of cylinder air charge is important to the whole model output of state variables. m_{air} serves as direct or indirect input for all other linked calculi. Hence, the fine-tuning of this step is performed carefully. Following Roithmeier's approach [87], it might be useful to employ "discharge characteristics" at cylinder valves as command variable. For an idealized but throttled

flow [60], the isentropic mass flow over the valve is given by

$$\dot{m}_{is} = A_{dis} \cdot \sqrt{\rho_0 p_0} \cdot \Psi_{dis}. \tag{2.8}$$

Hereby, A_{dis} characterizes the cross section area of the outflow and $\Psi_{dis} = f(p_1/p_0, \kappa)$ is the isentropic flow function. Due to friction losses, the flow cannot be described as isentropic process. The real mass flow over a throttling device is therefore scaled with isentropic conditions via a "discharge number" or "alpha number".

$$\dot{m}_{real} = \alpha_{dis} \cdot \dot{m}_{is} \tag{2.9}$$

As measured at flowing test benches, α_{dis} is a function of the open cross section. The flow itself will considerably change if the valve lift changes, hence $\alpha_{dis} = f(L_{IV})$, which can be seen in figure 2.6 (start of iteration). Roithmeier already pointed out,
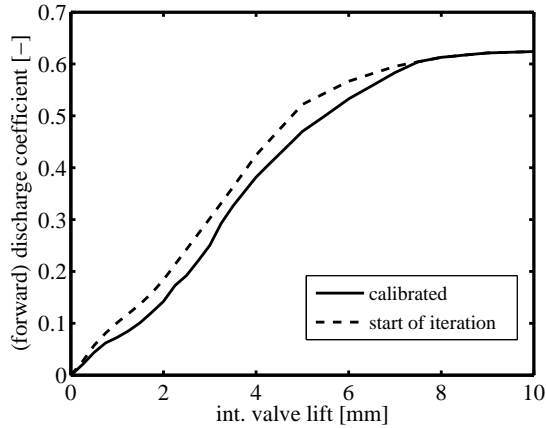
Figure 2.6: Alpha curves are used as optimizing command to achieve expected values of cylinder charge especially for very low loads.

that for engine operation at variable valve lift, the discharge characteristics α_{dis} have to be adapted especially in low lift ranges [87]. The procedure can be still seen as physical because the adaption takes into account that the valve flow can then not be approximated as quasi-stationary anymore, while the measuring process is still preserved. (More details and further investigations on the measuring process of alpha curves can be found in Natkaniec [66] and Dorsch [15].) In this case, a standard optimizer algorithm was employed to minimize the squared sums of error between expected and predicted air charge for different valve lifts, valve timings etc. The optimizer worked by a change of low-lift alpha numbers and a combination of variable

spline and fixed-point interpolation to keep the inflow alpha curve steady, compare figure 2.6 (calibrated). The overall algorithm iterates automatically, which makes its use comfortable. It shall be mentioned, that the thermodynamic model can also work without external fine-tuning (and therefore without available measurement data) but accuracies especially within low load points can be improved notably with little effort in this step. For throttled operation (maximum intake valve lift), the adaption of reverse alpha numbers can be interesting to keep back flowing residuals from virtually "blocking the intake valves" for entering fresh air.

2.3.3 Investigation work flow for a complete engine map with GT Power.

Engine simulations provide the base data to train the RT model. The main idea is to gain profound knowledge of trapped cylinder masses, which depend on highly varying engine parameters. Hence, a methodical approach to the problem can keep the simulation effort rather manageable: the air charge determination per cylinder can also be interpreted as volumetric efficiency (*voleff*). Equation 2.10 relates the trapped mass to a reference state.

$$voleff = \frac{1}{m_{ref}} \cdot \left(\int_{IVO}^{IVC} \dot{m}_{air,int} dt - \int_{IVO}^{EVC} \dot{m}_{air,scav} dt - \oint \dot{m}_{air,bb} dt \right) \qquad (2.10)$$

The first term $\dot{m}_{air,int}$ contains the entering air mass flow in the intake phase, the second term considers an exiting mass flow $\dot{m}_{air,scav}$ over the exhaust valves in the scavenging phase and the blow by term $\dot{m}_{air,bb}$ can be seen as negligible for efficient engine operation. (The scavenging term has special relevance for long valve overlaps at low engine speeds, which assists direct interaction between intake and exhaust port.) The mentioned reference state in equation 2.10 occurs when the whole cylinder displacement is filled with air at reference density (1013mbar, 303K), cf. equation 2.11.

$$m_{ref} = V_{displ} \cdot \rho_{air \ ref} \qquad (2.11)$$

Volumetric efficiency shows a major dependency on the intake manifold pressure. In figure 2.7 the trapped air curve is plotted for a single combination of engine parameters. A higher degree of throttling in the intake reduces and a higher degree of turbocharging increases fresh cylinder charges. The behavior shown in figure 2.7 is quite similar for every air charge curve irrespective of surroundings: a certain slope of the throttled operation distinguishes the linear curve part in *part 1*. When the cylinder aspirates at ambient pressure, *part 2* is the specific volumetric efficiency for certain cam timings, valve lift etc.. When exposed to higher intake pressure, residual gas is flushed out of the cylinder rapidly and leaves more volume fraction to fresh air charge. This effect results in an s-shaped curve part for turbocharged operation. The character of *part 3* lies within the starting point and the offset value from linear extrapolation. As all these
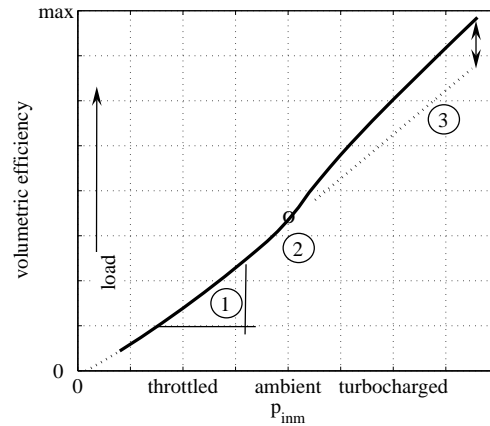
Figure 2.7: Generic profile of volumetric efficiency for variations of intake manifold pressure.

property values in figure 2.7 vary for different engine operations, systematic simulation may determine air charge curves and further thermodynamic states straightforward. Just before scanning the complex engine map, specific modifications were applied to the GT Power model, compare figure 2.4:

- Direct injection shut off. (A function outside the NN computes the temperature drop.)

- Build up of monitor points for air mass, residual fraction and temperature at IVC.

The preparation of the GT Power simulation also involves making a grid of virtual measuring points. The input parameters contain all operation variables except for intake pressure. They can be obtained from optimum maps out of basic engine calibration (valve timing, valve lift, ignition timing) or empirical data of parental engines. Here, the computation of the whole engine map range prevents from NN extrapolation later on. The intake pressure quantity is left to variation. Aiming a good reproduction of air charge curves, the rastering nodes should be lying closer within the s-shape. In summary the present work simulated around 750 complete air charge curves with nearly 10.000 steady state operations within 5 days of parallel computing.

2.3.4 Training of the real-time model.

Neural networks (NN) are arithmetic structures that can reproduce nonlinear behavior of technical systems. Basically they contain neurons (compare figure 2.5, white circles)

that interact via signals with each other. The network is provided with several input stimuli from its environment (input control vectors in figure 2.5), performs the required calculations via signal processing in the hidden layer and delivers an output back to the environment (rhombic signals in figure 2.5). All signal processing is performed via weighting, accumulation and transferal conversion [49, 117]. NN behave akin to natural organisms: RT processing, reaction on changing boundary conditions and learning abilities are valued properties in many applications. Thereby the learning or "training process" refers to a shift in signal weights for signal processing. The discrepancy between a target output value and real output supplies the measure imperative for the training. Hence the learning is known to be "supervised" and minimizes the output error. Static NN of the type multilayer perceptron (MLP) were enabled to account for air charge determination problems at the BMW Group [87].

Together with a Bayesian training algorithm at 200 learning iterations and several random seedings of initial weights, a variety of networks can be trained in short CPU time spans. The number of neurons in the net's hidden layer thereby has a big impact on the quality of results. It determines whether the network wrongly linearizes the context (too little neurons), "overfits" the trained data with tendency to oscillation (too many neurons) and whether the response surface is rather smooth and steady or rather noisy and unstable. It seems obvious that a good proof of quality for a bulk of trained networks is needed for selection of the best network construction. Figure 2.8 shows a possibility to choose the best network constellation via the expected output of temperature at IVC (true/predicted plot). Moreover if the output error appears to be quasi normal in distribution, the network shows favored behavior to external disturbances like in figure 2.8. These good quality criteria are most likely to be obtained with at least some 1000 evenly spaced training points (high complexity of the problem) and between 30-40 neurons in the hidden layer. The used neural structures are based on MLP with Bayesian regularisation algorithm for learning and several random initialization runs for weighting values between the neurons. The multilayer perceptron uses a "*sign*" basic activator function within only 1 hidden layer. The error of each training run is defined as cumulated difference between the known thermodynamic target result and the network's produced output.

2.4 Modeling fuel direct injection.

Accurate modeling of fuel evaporation is an important key to predict cylinder temperatures [7]. Common rail direct injection is highly flexible, regarding the number and starts of injections (SOI), their duration and rail pressure. The approach of modeling temperature drop outside of the NN in figure 2.5 keeps the structure modular (the effect is left out of the calculus for temperature at IVC). Thus, it is desired to resolve the temperature effect at 690°CA, the virtual ignition timing. The measure is called
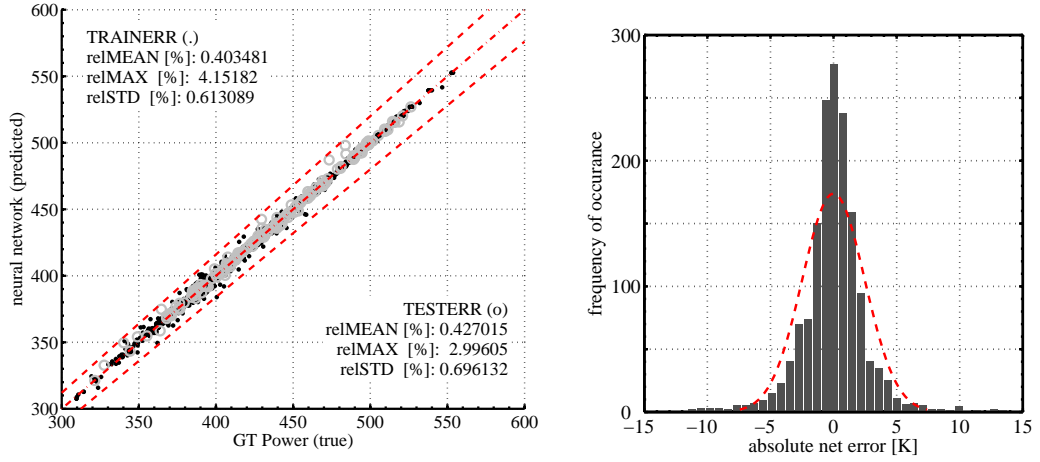
Figure 2.8: Example quality rating of neural network training (temperature at IVC) via true/predicted plot with ±5% bounds (left) and quasi-normal distribution of the error function (right). These charts contain data from the whole engine map investigation with several 1000 single simulations.

ΔT_{690} and accounts for the temperature drop compared to the motored curve without injection, see equation 2.12.

$$\Delta T_{690} = T_{690,mot} - T_{690,fired} \tag{2.12}$$

2.4.1 Main ideas for the GDI impact.

The integration of an injection sub model [62] into the given structure of section 2.3.1 is based on the following assumptions:

- Time dependent effects are neglected (instantaneous injection and evaporation).

- Evaporation processes are adiabatic inside the cylinder, hence external heat exchange is neglected.

- 0-dimensional modeling can be applied (homogeneous temperatures profiles in fresh air, fuel and residual gas).

- Thermochemical properties only depend on temperature and composition. The fuel's specific gas constant values $R_{fuel} = 80 J/kgK$ and its heat of evaporation lies between 350-500kJ/kg with 298K start temperature, compare appendix B.

It's now straightforward to form two states for the energy balance [7]. Equation 2.13 refers to the explicitly known state prior to evaporation (prvap) when all gaseous components are perfectly mixed and liquid fuel enters at a level between rail and cylinder temperature. Subsequently equation 2.14 forms the implicit state after evaporation (afvap) when all components in the cylinder share the same temperature. Both equations can be identified and solved for temperature after evaporation with the help of an implicit table lookup. Therefore figure 2.9 shows the internal energy with parameters temperature and afr according to Pischinger's tabulation [75].
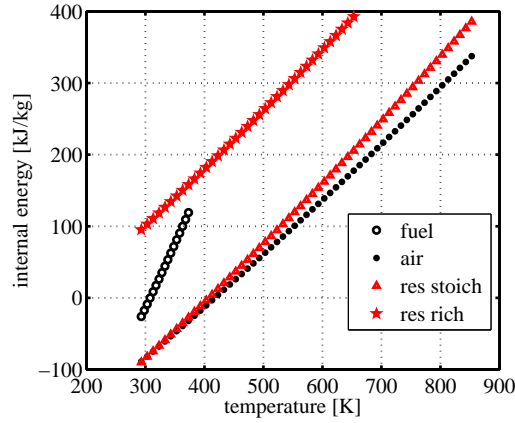
Figure 2.9: Components' internal energy vs. temperature at fuel direct injection.

$$
\begin{aligned}
E_{prvap} = m_{air}u_{air}\left(T_{prvap}\right) + m_{res}u_{res}\left(T_{prvap}, \text{afr}\right) \\
+ m_{fuel} \cdot \left[u_{fuel}\left(T_{fuel}\right) + R_{fuel}T_{fuel} - \Delta H_{vap}\right]
\end{aligned}
\tag{2.13}
$$

$$
\begin{aligned}
E_{afvap} = m_{air}u_{air}\left(T_{afvap}\right) + m_{res}u_{res}\left(T_{afvap}, \text{afr}\right) \\
+ m_{fuel}u_{fuel}\left(T_{afvap}\right)
\end{aligned}
\tag{2.14}
$$

It is important to note that the integration over time for ΔH_{vap} only accounts for short time spans of the instantaneous evaporation in this energy balance. The interpretation of equation 2.15 leads to the temperature drop directly at SOI. The impact differs from 20 to 40K, which was also investigated in literatures [17, 39].

$$
\Delta\left. T_{inj}\right|_{SOI} = T_{prvap} - T_{afvap}
\tag{2.15}
$$

49

Furthermore the obtained temperature difference is held constant in the intake stroke until IVC. This considers the compensating effect of still entering fresh gas. In the compression stroke a polytropic change is assumed for the temperature delta, hence the final volume accounts to $690°$CA and produces the offset ΔT_{690}. (This proceeding is in accordance with a separation of total temperature and temperature delta in equation 2.15 which can be separately entered in equation 2.5. So the superposition principle is preserved over the piston stroke.) The final offset ΔT_{690} can then be easily applied.

2.4.2 Main influences on the temperature drop.

Figure 2.10 shows some resulting variations of a wide model analysis: the richer the
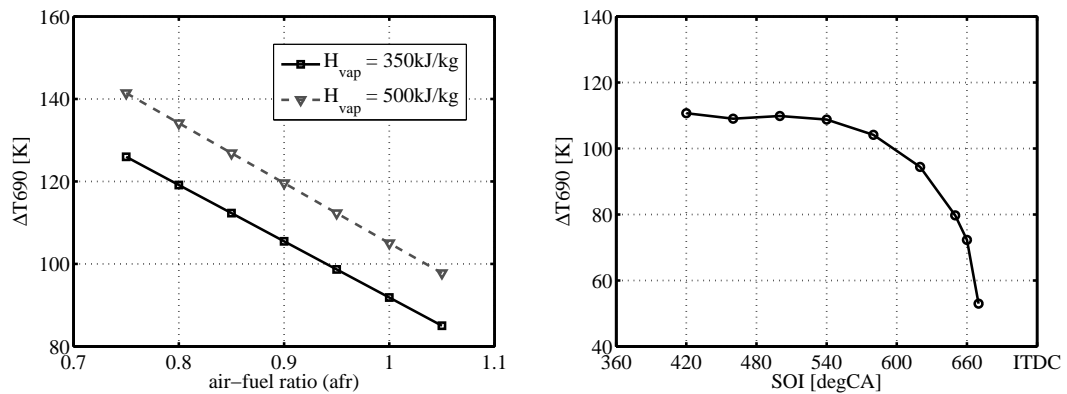
Figure 2.10: GDI parameter variation on the temperature impact at $690°$CA. The influences were varied for an operation at 6000RPM and full load (*bmep* equals 21bar for the BMW N20B20 engine).

mixture, the higher the cooling effect at $690°$CA (with respect to global fuel properties). This behavior is sometimes used for wider knock limits or for protection against overheat in the exhaust manifold. Moreover a late injection shows a decrease of the resulting offset drop in figure 2.10. This is caused by a lower volume ratio that compresses the delta from SOI to $690°$CA. (When injecting at 420degCA, the amplification of $T_{inj}|_{SOI}$ reaches 75% at 690degCA, whereas for equal fuel masses only 66% and 28% of amplification occur for ignition timings at 600degCA and 660degCA.) Hence the optimal injection timing can again be used to operate the engine further from knock events. In summary some observations resulted in more than 100K delta before ignition (compression ratio $\epsilon = 10$). Mühlbauer arranged to put main influences on the GDI temperature drop before ignition into an order of priority [62] - the results can be found in table 2.3. It can be mentioned, that fuel temperature, engine load, charge air

priority	influence	reason
1	start of injection	effective compression ratio
2	engine speed	wall heat transfer rates
3	air-fuel ratio	instantaneous temperature drop
4	heat of vaporization	instantaneous temperature drop

Table 2.3: Priorized impacts on temperature drop caused by gasoline direct injection.

temperature and injection delivery rate are only minor aspects to relative examinations of ΔT_{690} (< 10K).

In a future step, considering all time dependent effects could improve the model's quality. Thereby all processes involved have a defined duration and shift the evaporation center (CA with 50% vaporized) away from SOI with direct transfer to the offset ΔT_{690}. Further recognition of engine speed within the polytropic compression contributes to a better account of wall heat transfer, cf. section 2.3.1. Currently the air charge determination is not supposed to back link the injection cooling on fresh gas inflow at the intake stroke. This recharging might be an additional modeling step to be included.

Regarding the model flow chart in figure 2.5, at first all temperature relevant calculations are carried out (neutal networks for air mass and residuals, NN for T_{IVC}, polytropic change) before the GDI cooling approach is applied. With that final step, the temperature T_{690} at a virtual ignition timing of 690°CA can be obtained.

2.5 Model validation with pressure trace analysis.

In the following section the thermodynamic model results are compared with its expected performance. Therefore, air charge measurements from a test bed were basis for a quantative validation of the NN output in figure 2.11. Tolerated limits for "virtual air charge determinations" typically value around $\pm 10\%$ and are met nearly in the whole engine map (light green marks). But there still are certain improvements necessary regarding GT Power accuracy at very low loads (low intake valve lifts) and high valve overlap. Whilst air charge quantities can be measured directly on the engine's air path, other quantities e.g. residual fractions have to be calculated with more sophisticated methods. Therefore, one possibility is the so called *"three pressure analysis"*. Recorded pressures in the inlet manifold, cylinder and exhaust manifold plus some constant temperature estimations allow to balance certain mass flows (e.g. internal/external residuals) that occur at the engine test bed. (When coupled with a "pressure trace analysis, the evaluation of the first law of thermodynamics produces burn rates of
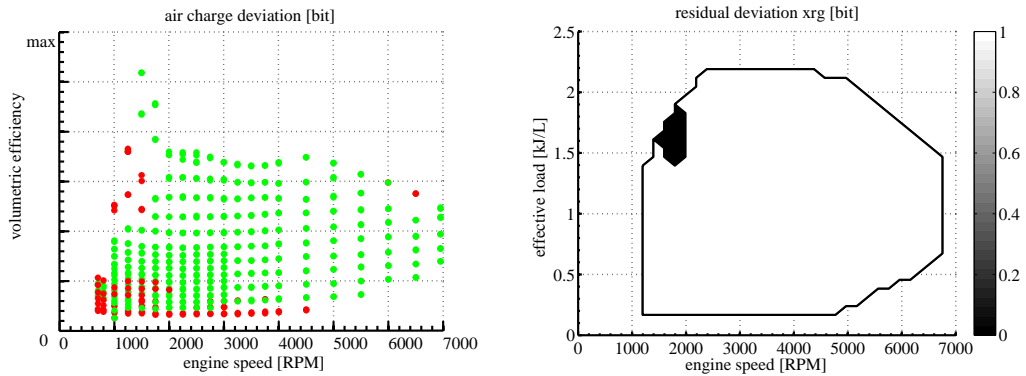
Figure 2.11: Qualitative model validation of air charge (left) and residuals versus cylinder pressure trace analysis (right) for the BMW N20B20 engine. Only dark marks exceed tolerance limits.

the combustion with the measured cylinder pressure as input.) Figure 2.11 (right) also shows a good comparison of residual fractions versus some pressure trace analysis results. Only when complex scavenging flow effects occur at high valve overlap, the results diverge from requirements in the table 2.1. Temperature deviations in figure
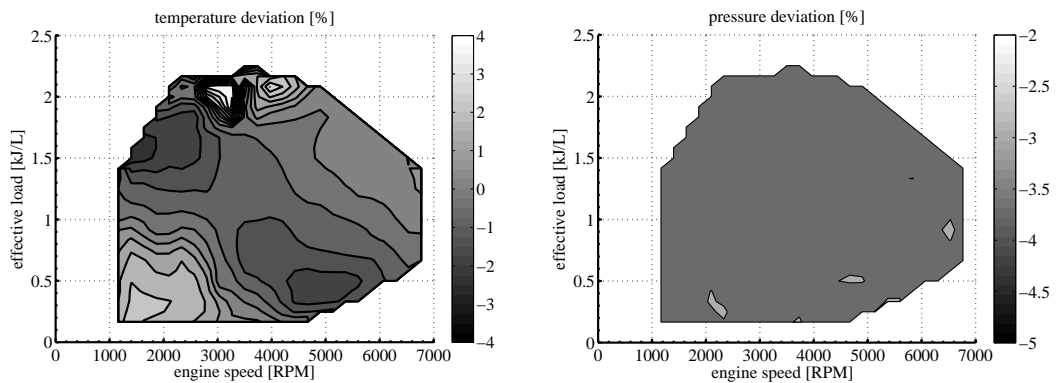
Figure 2.12: Quantitative validation for temperature (left) and pressure (right) of the model vs. test bed measurements from BMW N20B20 .

2.12 (left) compared with results from the pressure trace analysis, show a sophisticated distribution caused by the overall parameters that act on it. Nevertheless all required accuracies are met. Also pressure outputs are reliable although partially underestimated within the map.
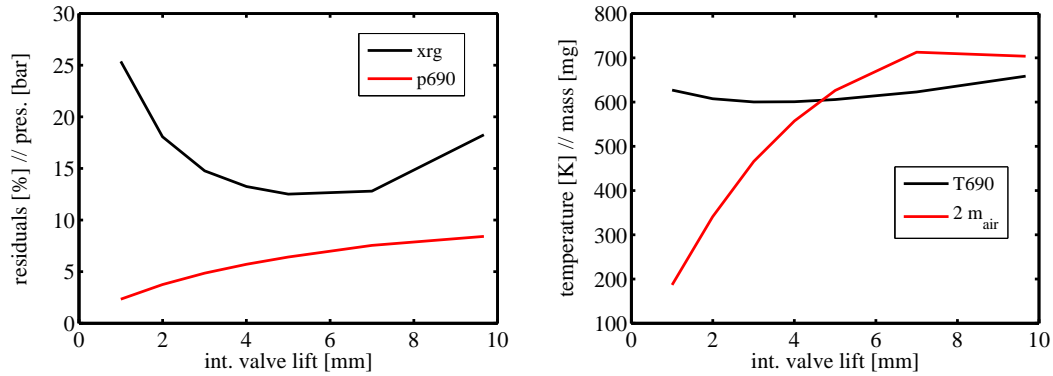
Figure 2.13: Variation of intake valve lift for part load operation at 2000RPM. This parameter serves as actuator for cylinder air charge. Temperature T_{690} replicates the quality of pressure p_{690} and residual fraction x_{rg}.

2.6 Parametric study

After assuring that the calibrated thermodynamic model shows satisfying behavior, it's now straightforward to perform parametric variations and observe thermodynamic quantities at ignition top dead center (ITDC). This serves as general study to gain knowledge about the engine behavior. All upcoming studies begin at a sample operation of 2000RPM/$bmep$ 2bar (VVT) with single direct injection to the intake stroke at AFR=1 for the *BMW N20B20* engine, see appendix A and C.2. In figure 2.13 it can be seen the effect of increasing mean valve lift at the intake side. In unthrottled operation mode, the mean lift is used to control trapped air charges. Hence, an increase of intake valve lift rises engine load as well as the pressure level before ignition. Temperature T_{690} depends on pressure and trapped residual fractions, which commands to see a minimum of T_{690} at minimized residuals. (Residual fractions x_{rg} in figure 2.13 have a minimum at around 5-6mm mean lift. Up to that state the increased cylinder fresh charge suppresses residual rise. For higher intake valve lifts, a decent throttling of around 50mbar in the intake manifold causes a back flow of residuals into the intake port. These residuals in the intake port "block" the intake valves and are the first masses to insert the cylinder again, preventing an increase of the air charge flow at the same time.)

Figure 2.14 shows a direct variation of in-cylinder residuals. The wide range of diluent fractions was performed via proceeding exhaust valve timing from late to early (low to high x_{rg}). The coupling of temperature and gas composition could already be observed in figure 2.2: hot residuals heat up the overall cylinder gas mass. Moreover, it is
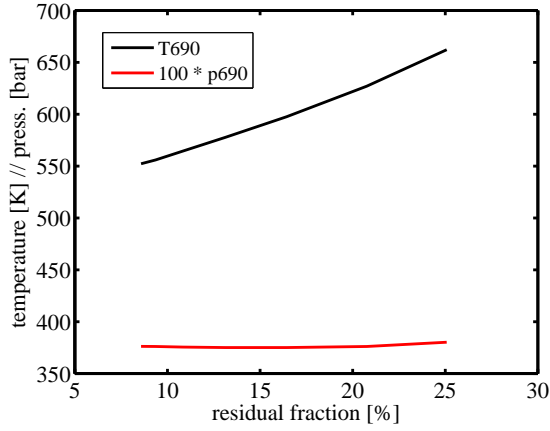
Figure 2.14: The variation of exhaust valve timing yields a greater change of residual fractions for part load operation. With this mechanism, temperature levels before ignition can be adjusted greatly (as performed at HCCI operation). Pressure shows little reaction.

interesting to note, that cylinder pressure nearly stays unaffected by residual rises. Hence, the detaining of residuals for coming cycles actuates temperature levels. Another feature of variable valvetrains, intake valve timing, is variated in figure 2.15. Again, the valve timing determines trapped air masses after gas exchange. Residual fractions react quite similar to a fresh air change like in figure 2.13. For the assessment of gas change losses, there was defined a quality index, which scales

$$\text{qual}_{gas-chg} \propto \frac{voleff}{\text{pmep}} \tag{2.16}$$

with pumping losses from the gas change cycle defined as

$$\text{pmep} = \left. \frac{1}{V_{displ}} \cdot \int pdV \right|_{gas-chg} < 0. \tag{2.17}$$

Hence, the quality index from equation 2.16 is high, if volumetric efficiency *voleff* is high and pumping losses pmep are low. This state is the most efficient. In figure 2.15 (right), the normed quality index is plotted. There exists an optimal and early valve timing, which can achieve dethrottling via high residual fractions and small gas change loops in the indicator diagram. For later valve timing, the optimum is left – the advantages of early intake valve closure are corrupted. The engine states converges to a Miller cycle.

54
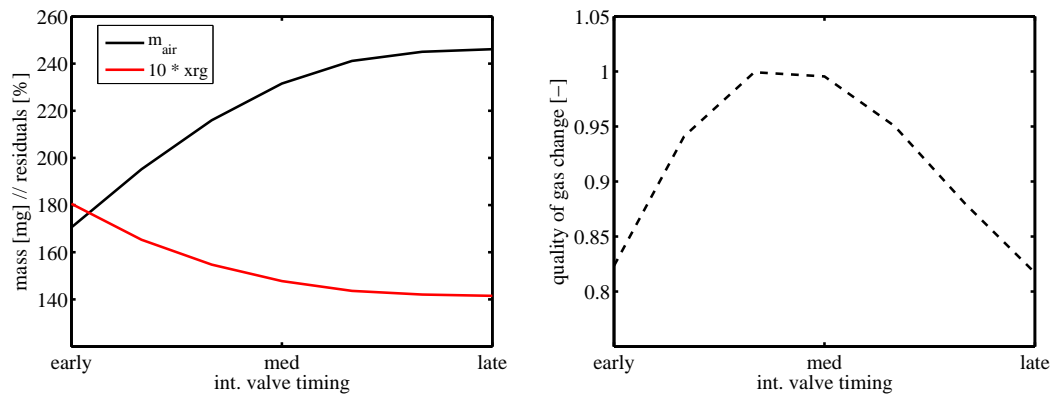
Figure 2.15: A change of intake valve timing (60-115degCA a.TDC) shows a variety of effects. IVC timing impacts on trapped air and links back on lower residual fractions for late closure (left). With the help of an additional gas change analysis, there was established a measure for the quality of gas change in certain engine operations (right). There exists an optimal valve timing (early for part load), which optimizes the trade off between air charge and gas exchanges losses. A deviation from this optimum lacks efficiency.

2.7 Outlook on applications.

All possible applications can be divided into two categories, online and offline:

- Online results are demanded in the case of
    - an upcoming ECU structure that needs information about residual fractions and temperature (model based combustion control [113], knock limits, robust HCCI operation [67] or flexible online emission prediction).
    - a HiL unit processing an RT thermodynamic cycle. The calculation can then omit the critical gas exchange because cylinder charge and starting temperature are estimated in advance [35].

- Employing the model offline can be feasible for calibration engineers when assessing parameter changes quickly without remeasurement.

2.8 Summary and confidence interval.

Within this section a complex thermodynamic model with RT capability was developed employing neural networks and fast calculations. The model structure was supplied with an extensive data base of 1-dimensional GT Power simulations, which were previously fine-tuned in an automatic process. Now the laminar burning velocity can be determined accurately for RT purposes like in ECU and HiL applications. Hence, the consequent advance of methodic tools contributes to a virtual model of complex combustion processes.
Nevertheless, a couple of thermodynamic states in the engine map have to be observed with caution, because of the applied methodology. For the following operating regimes, the errors may be outside the acceptable range:

- high valve overlap between exhaust and intake (there occur 3D effects, which are hardly defined).

- highly throttled operation with early intake valve openings (massive reverse flows of residuals into the intake port block the next cycle's intake flow).

- highly fluctuating pressure gradients and greater oscillations at the valves and in adjacent control volumes (affect discharge solutions of equations 2.8 and 2.9).

3 Quasi-dimensional modeling of turbulence and global charge motion.

Preface for turbulence modeling. Chapter excerpts were published previously [29]. The introduced turbulence model is summarized in appendix D.4.

3.1 Introduction.

3.1.1 Nature of turbulence.

A turbulent flow is characterized by highly varying velocity components considering its time-averaged value. The velocity field is normally irregular in time and spatial dependency. Kinetic energy of a turbulent flow is constantly dissipated to friction heat. Hence, large scale motion in a turbulent flow constantly breaks down to smaller scales. The existence of this energy cascade depends on constant external supply, otherwise it will extinct [16, 60]. Turbulence effects can be classified into mass transport and energy transfer. Mass transport occurs in mixture formation processes (e.g. fuel spray break-up, convective vaporisation) as well as within cylinder charge homogenisation (e.g. mixing of residual gas and fuel in the fresh charge). Energy transfer especially relates to convective heat transfer (e.g. thermal boundary layer at the cylinder walls, gas to valve heat transfer at gas exchange). The premixed flame propagation is affected by turbulence on multiple length scales. Global charge motion in internal combustion engines contributes to optimum performance and emissions [1]. This effect is known to evolve from the interaction of the laminar flame with local flow field characteristics. The flame front is deformed by vortices, broadened and gains in surface $dA_{f,turb}$. Hence,the consumption of unburnt fresh gas is accelerated by the term $\rho_u \cdot s_L \cdot A_{f,turb}$. Moreover, certain global charge motion can stabilize cycle to cycle fluctuations of the flame. Hence, turbulent structures in internal combustion engines are of common interest.

3.1.2 Necessity for an in-cylinder turbulence model.

The high pressure part of an engine cycle is highly sensitive to in-cylinder turbulence:

- models for the gas to wall heat flux consider turbulence [6]

- convection mean flow and turbulence intensity at top dead center define initial boundary conditions for the ignition phase, e.g. sparking heat loss and flame kernel development [20]

- the developing flame after inflammation spreads according to the proportions of integral length scale, laminar flame thickness and turbulent fluctuation [20]

- turbulent flame speeds in internal combustion engines are several times faster than laminar propagation [74]

- high flame speeds can achieve favorable low emissions, especially with time-depending nitric oxide mechanisms and the avoidance of early wall quenching for hydrocarbon formation (burn-off phase)

- cyclic variations have their origin in turbulent fluctuations [25, 34, 75]

Those effects are all of major interest for the simulation of the engine cycle. Hence, the goal is to obtain a simple and quasi-dimensional model for turbulence quantities in the compression and working stroke of the cycle. In section 3.2.1 several approaches to this problem are reviewed. Yet, none of those is able to cope with modern complexity of variable valve trains with different intake valve lifts and valve timings, because the flow fields and occurring turbulence differ widely [5]. The proposed model here can physically predict tumble and swirl based motion and the production of turbulent kinetic energy based on a k-ε-approach within all engine operations.

3.1.3 Sensitivity analysis.

The key idea in determing the turbulent flame development s_T involves the turbulent Damkoehler number Da, whereas turbulent and chemical time scales are evaluated.

$$Da = \frac{\tau_{turb}}{\tau_{chem}} = \frac{s_L}{v'} \cdot \frac{l_t}{l_f} \tag{3.1}$$

Hence, the turbulence model must supply the turbulent velocity fluctuation v' from Reynolds' decomposition (simple isotropic assumption yields $v' = \sqrt{2/3k}$) and the turbulent length scale l_t. Laminar flame thickness l_f and laminar flame speed s_L are independently evaluated, following the thermodynamic path. The variational calculus regarding a match of burn rates (model versus pressure trace analysis) showed a required accuracy of around $\pm 5\%$ for the turbulent burning velocity s_T. The determination of s_T therefore follows Peter's correlation [74] and was performed similar to the previous quasi-steady proceedings (compare chapter 2.1.1). Figure 3.1 (left) shows the sensitivity of the flame propagation speed for the variation of turbulent kinetic energy k in six different engine operation points for the *BMW N20B20* engine, compare appendix A and C.1. Here s_T/s_L was used as a measure for the flame acceleration. Especially in weakly turbulent regimes, a small deviation of k proves a high interaction potential. The more turbulent the flow gets, the more "saturated" gets the flame acceleration (not every fraction of k is invested in a faster flame [53, 55]).
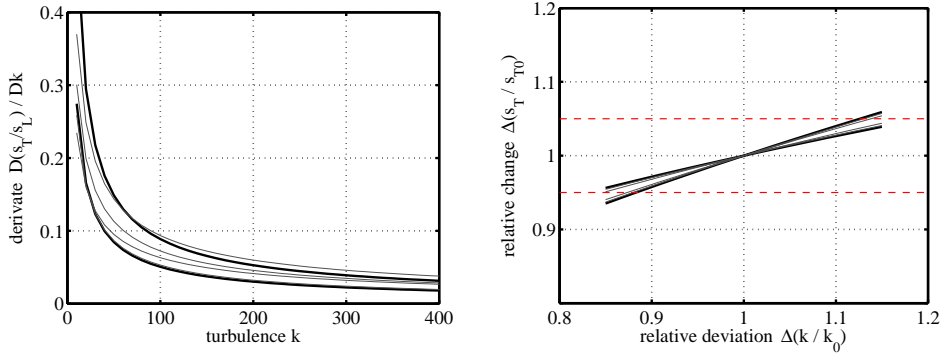
Figure 3.1: Physical response of the burning velocity s_T on turbulence. Additional flame acceleration decreases with increasing turbulence (left) and deviation in the turbulent kinetic energy k determines the resulting change in flame speed (right). Subscript "0" relates to a reference operating point, dashed lines set accuracy limits.

Hence, assuming that turbulent inputs are most uncertain, figure 3.1 (right) shows the relative change of turbulent burning speed s_T as depending on quasi-dimensional deviations. Also shown are the accuracy intervals for $\pm 5\%$ in s_T along the ordinate direction, which consequently aim at comparable fuel burn rates. It can be stated from figure 3.1, that the turbulence model must deliver the effective turbulent kinetic energy k with $\pm 15\%$ accuracy to meet the overall requirements. The results are derived from six different operating points within the engine map. (A broader confidence interval of $\pm 10\%$ for s_T would even allow a quasi-dimensional freedom of $\pm 25\%$ for the turbulent kinetic energy k around its effective value. In this context, Schubert [93] mentions a 30% deviation for k as input for convective inner cylinder heat transfer calculations as sufficient.)

3.2 Governing Physics.

3.2.1 Quasi-dimensional turbulence via k-ε-modeling.

Common approaches for turbulence modeling without spatial information often solve a simplified combined k-ε-equation. Whereas this turbulence model is known as two-equation set in 3D CFD applications, its quasi-dimensional counterpart corresponds to a volume integration working with only one ODE as shown in equation 3.2.

$$dk = (dk_{int} - dk_{exh} + dk_{inj}) + dk_{dens} + dk_{squish} - \varepsilon \cdot dt \tag{3.2}$$

The change of turbulent kinetic energy (TKE) according to equation 3.2 consists of

- produced TKE from the intake stroke mass flow dk_{int}

- TKE convection out of the system over the exhaust valves dk_{exh}

- produced turbulence via fuel direct injection dk_{inj}

- a density depending increase or decrease dk_{dens}

- the squish volume depending term dk_{squish} and

- the viscous dissipation ε on molecular length scales

Together, dk_{int}, dk_{exh} and dk_{inj} form a gas change related influence. It is important to note, that the specific equation 3.2 can only be balanced with the help of extensive energy levels $dK = d(k \cdot m)$ which consider mass changes in the system. Standard turbulence theory proposes a two-equation k-ε set with recognition of dk_{dens} and ε [80, 105]. In 1980 Borgnakke et al. [9] solved this set for quasi-dimensional purposes, compare equations 3.3 and 3.4.

$$dk_{dens} \propto \frac{2}{3} \cdot \frac{k}{\rho} \cdot d\rho \qquad (3.3)$$

$$\varepsilon \propto \frac{k^{3/2}}{l_t} \qquad (3.4)$$

The reduction to a simpler one-equation ODE can be found at Noske in 1988 [70]. Later on, Bargende added the squishing term dk_{squish} in 1991 with relevance for high compression ratios especially in Diesel combustion, compare equation 3.5 [6]. (In spark ignition engines with compression ratios around 10 and rather small piston cup geometries, dimensional comparison shows a vanishing squishing term compared to a 2-3 orders of magnitudes larger density term dk_{dens}.)

$$dk_{squish} \propto \frac{dV_{squish}}{V_{cyl}} \cdot v_{squish}^2 \qquad (3.5)$$

Here, the volume flow dV_{squish} is driven with the radial velocity v_{squish} out of the piston cup, both evolve from the piston's compression movement. Moreover Bargende introduces a new starting value k_{IVC} at intake valve closing for the ODE calculation. It takes into account the global velocity, the volumetric efficiency and the intake valve lift [6]. In 2001, the completion step for quasi-dimensional turbulence was established by Pivec with introduction of an injection term as in equation 3.6 [79]. Hence, the directly injected mass flow $\dot{m}_{inj}$ enters the cylinder at a velocity v_{inj} and adds up to the total

mass m_{cyl}.

$$dk_{inj} \propto \frac{\dot{m}_{inj} \cdot v_{inj}^2}{m_{cyl}} \tag{3.6}$$

In equation 3.2 the terms dk_{int} and dk_{exh} are rarely evaluated because of immense calibration efforts when fine-tuning the model. Nevertheless, some applications do have the need to know about turbulence within the whole engine cycle and newer engine generations show a high sensitivity of in-cylinder turbulent states on intake and exhaust processes [5]. So there are often arising problems. Figure 3.2 shows another problem of the named model: When complex charge motion occurs in the cylinder, it cannot
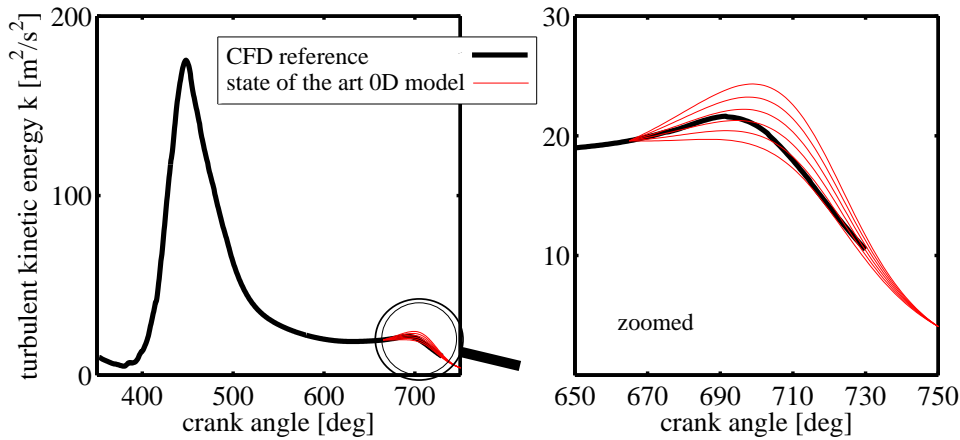
Figure 3.2: State of the art for quasi-dimensional turbulence modeling carried out for the BMW N20B20 engine. 3D CFD sample operation at 2000RPM and *bmep* 2bar (VVT), the 0D model is calibrated in different ways to best fit the reference.

predict the production of turbulence from viscous shearing forces. Hence, this model is not intended to predict the effects of tumble break down and swirl decline within compression, especially when both types of charge motion superpose. In figure 3.2, a comparison of 3D CFD data with the quasi-dimensional approach from equation 3.2 is plotted in different configurations as Schubert [94] and Nefischer [68] proposed, compare appendix C.2 (VVT with swirl motion) for details. Especially the term dk_{dens} is repeatedly used to fit quasi-dimensional data to reference turbulence by introduction of an anisotropy prefactor. Nevertheless, different 0D model calibrations neither agree with quality nor with quantity of the 3D CFD calculation, caused by negligence of charge motion effects. This issue even aggravates, when the prediction of turbulence in the whole engine operation map is required. The obviously resulting need for a quasi-

dimensional turbulence production term (investigations on charge motion shearing) was already identified by Achuth and Mehta in 2001 [1, 2]. They operate with only tumble driven engines and assume some geometry relevances for the shearing gradient $\frac{\partial U}{\partial y}$. A new approach for turbulence production in section 3.2.3 is not restricted to only one direction of charge motion and furthermore it won't assume geometric measures for quasi-dimensional evaluation. This keeps the approach flexible for different operation states and engine geometries. A transfer to other engines is therefore promoted.

Another term of equation 3.2 plays a significant role for turblence: dissipation ε. The common problem in equation 3.4 is now finding a straightforward formulation for integral length scales l_t in the cylinder. Currently, there exist two accepted approaches which link the length scale with the current cylinder volume V_{cyl}, compare equation 3.7.

$$l_t \propto (V_{cyl})^{exp} \text{ with } exp = \left\{ 1; \frac{1}{3} \right\} \tag{3.7}$$

Both formulations suffer from the fact, that they cannot precisely reproduce the quality of the "global" integral length scale from 3D CFD analysis, because they are directly associated with geometry. Figure 3.3 shows, that the integral length l_t from 3D CFD converges after the anisotropic intake stroke (around 450degCA) for a wide variety of engine operations. A misinterpretation of l_t by formula 3.7 leads to wrong Damkoehler numbers and therefore to an uncertain turbulent burning velocity s_T. This case especially occurs in the prediction for an ignition timing near or after ITDC, where quasi-dimensional approach and CFD analysis diverge widely like in figure 3.3. Obviously, only a wider 3D analysis is capable to solve this problem and transfer the results back to a 0D approach. Caused by the weakness of equation 3.7, it seems reasonable to produce an expression that takes into account the formation of flow structures via the limiting intake valve lift L_{IV} and later turbulence development after intake valve closure values k_{IVC}. Simple proposals as in equation 3.8 are give at Hunzinger [41] and Dai [13].

$$l_t \propto (L_{IV})^a \cdot \sqrt{\frac{k_{IVC}}{k}} \tag{3.8}$$

Summarizing, the aim of a new 0D turbulence model is to predict the production of turbulent kinetic energy caused by shearing forces on complex charge motion and by the intake flow. This is achieved by an extra term dk_{prod} in the sum of equation 3.2. In the following, several assumptions are described and evaluated.

3.2.2 General assumptions for a new modeling approach.

On the one hand the quasi-dimensional model of section 3.2.3 allows a fast and straightforward evaluation of turbulence at all engine operations. On the other hand,
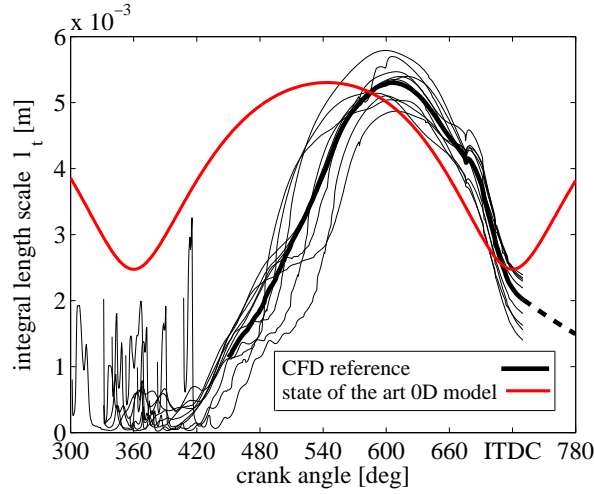
Figure 3.3: Integral length scale development over an engine cycle. CFD analysis was performed at all relevant engine operations (thin curves, compare appendix C.1 and C.2) and converges within the compression stroke (mean curve solid and extrapolated curve dashed). Common 0D models cannot precisely interpret the l_t quality.

the modeling of global flow phenomena without spatial resolution must introduce some simplifications. All calculations take place in a strongly simplified combustion chamber with flat cylinder head and piston geometry as shown in figure 3.4 together with the given coordinate system. In this cartesian coordinate space, the angular momentum vector $\vec{L}$ describes all occurring motions of charge and can be written in a simplified form (assuming the inertia tensor is a diagonal matrix) as

$$\vec{L} = \begin{pmatrix} L_x \\ L_y \\ L_z \end{pmatrix} = \begin{pmatrix} J_x \cdot \omega_x \\ J_y \cdot \omega_y \\ J_z \cdot \omega_z \end{pmatrix} = m_{cyl} \cdot \begin{pmatrix} j_x \cdot \omega_x \\ j_y \cdot \omega_y \\ j_z \cdot \omega_z \end{pmatrix}. \tag{3.9}$$

Thereby, L_x describes the main tumble component in the cylinder, L_y is the minor tumble component and L_z can be seen as swirling motion around the cylinder axis, see figure 3.4. In equation 3.9, the quantities J_i represent the global momentum of inertia (j_i as the mass weighted counterpart is derived in appendix D.2) and ω_i is the angular velocity component around the moving axis $i = \{x, y, z\}$.

Moreover the turbulent production is associated with the following physical phenomena:

- Intake flow is the main driver for charge motion generation (CFD analysis shows a negligible influence of the exhaust flow).
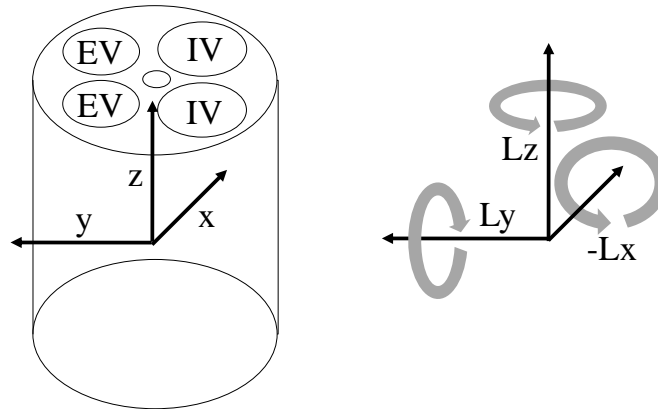
Figure 3.4: Geometry of the simplified combustion chamber (intake valves *IV*, exhaust valves *EV*) together with orientation of cartesian coordinates (left). Global charge motion from intake valves with main tumble induction L_x and the swirl component L_z (right).

- Air, fuel and residuals in the cylinder are homogeneous in density and perfectly mixed. Generated charge motion affects all internal components equally.

- Main tumble motion moves around x-axis (minor occurence of y-tumble can be derived from x-tumble in many engines). The xy-tumble associates both occuring tumble motions mathematically without quality loss in modeling, cf. figure D.1 in the appendix.

- The xy-tumble and z-swirl motion don't behave akin in decay and must be considered independently by superposition.

- Inlet port and valve masking provoke a mainstream direction for the incoming flow at small valve lifts (especially appropriate for z-swirl generation).

- The approach of an energy cascade can be applied [1, 82].

- The TKE distribution behaves quasi-dimensional and velocity fluctuations are isotropic within the compression stroke. A one-zone approach for turbulence can cope with all main effects in the pancake formed combustion chamber (simplified geometries).

- Gas viscosity can be assumed as constant impact on turbulent development for all temperatures in relevant engine operations.

3.2.3 Complex charge motion and production of turbulent kinetic energy.

The basic principle of an energy cascade concept is the idea of vortex stretching. This self-preserving energy transfer happens from greater to smaller length scales and is driver for turbulence production, which corresponds to the term dk_{prod}. [16] Vortex stretching constantly reduces the mean size of circulating flows by shearing. The smaller the rotating structures get, the higher is the influence of friction effects until the former kinetic energy totally dissipates into internal energy (heat) on Kolmogorov scales. Thus, turbulent fluctuations in an engine cylinder will vanish without continuous energy supply from the mean flow of directed global charge motion.

Modern engine concepts induce either swirl or just tumble or combination of both in the cylinder depending on the valve train actuation. So it seems evident to take a closer look at build up and decay of charge motion and all important effects on TKE. This follows the ideas of Poulos and Heywood [82] with recognition of angular momentum and rotational energy in every spatial direction. General production of turbulence $dk_{prod} \propto (\partial U / \partial y)^2$ contains the shearing rate of the mean velocity field U. Ramajo et al. [85] obtain the modified formulation in equation 3.10, which can be easily rewritten corresponding to Eiglmeier's approach [19] using global kinetic energy E_{rot} in equation 3.11.

$$dk_{prod} = C_{Ramajo} \cdot \frac{k^2}{\varepsilon} \cdot \frac{U^2}{l_t^2} \qquad (3.10)$$

$$dk_{prod} = C_{Eiglmeier} \cdot \frac{E_{rot}}{l_t} \cdot \sqrt{k} \qquad (3.11)$$

Ramajo et al. [85] and Achuth et. al [1, 2] mention the determination of production terms to be the most significant and hence complex part of quasi-dimensional turbulence modeling. The following sections interprete dk_{prod} as in equation 3.12 by direct employment of the energy cascade.

$$dk_{prod} \propto -dE_{rot} \qquad (3.12)$$

In the following, rotational energy E_{rot} is described as function of angular momenta L_{dir}, because they are seen as *global* quantities. (*Local* velocity components U of the flow field are not available in a non-spatial approach.) The objective is now to find an appropriate closure for k_{prod} which can cope with different forms of wide scale charge motion and their deviation into small scale turbulence. Therefore compression stroke and intake stroke of the engine cycle must be considered independently. Table 3.1 sums up frequent indices abbreviations, used in the following derivation.

index	description
IVi	*intake valve* numbering, IVi={1, 2}
dir	*direction* of vector decomposition, dir={xy, z}
prod	*production* formulation for TKE
rot	*rotational* energy of the gas mass
int	*intake* stroke related term
shr	*shearing* stress related term

Table 3.1: Frequently used indices for turbulence modeling.

3.2.4 Compression and expansion stroke (closed valves).

This section derives a form for the rate of change of turbulent kinetic energy TKE that applies for tumbling and swirl motions at constant cylinder mass (mass balance is adopted). Turbulent production at engine strokes with closed valves represents a special case of general modeling. Thereby the term k_{prod} can only evolve from the "potential", existing kinetic energy E_{rot} the cylinder offers. It accumulates shearing effects in directions *dir* like in equation 3.13.

$$dk_{prod} = dk_{prod,shr} = -\frac{1}{m_{cyl}} \cdot \sum_{dir} dE_{dir,rot,shr} \tag{3.13}$$

Hence, an energy term is needed for proceeding. The cylinder charge moves with rotational energy, which can be written as

$$E_{dir,rot} = \frac{1}{2} \cdot \frac{L_{dir}^2}{m_{cyl} \cdot j_{dir}}. \tag{3.14}$$

Therefore the change of rotational energy by shearing forces in the gas mass can be easily derived with static cylinder geometry in mind ($dj_{dir} = 0$, not evaluating the angular momentum conservation at piston movement).

$$dE_{dir,rot,shr} = \frac{1}{2} \cdot \frac{2 \cdot L_{dir}}{m_{cyl} \cdot j_{dir}} = 2 \cdot \frac{E_{dir,rot}}{L_{dir}} \cdot dL_{dir,shr} \tag{3.15}$$

Mass specific angular inertia j_{xy} of the tumbling gas mass depends on cylinder bore D_{bore} and the actual piston position s_{pist} in this time step. (The derivation of the terms in equation 3.16 and 3.17 is plotted in appendix D.2.)

$$j_{xy} = \frac{1}{4} \cdot \left(\left(\frac{D_{bore}}{2} \right)^2 + \frac{s_{pist}^2}{3} \right) \tag{3.16}$$

Specific angular inertia for swirl motion only depends on cylinder geometry because no vortex deformation takes place normally to the vertical axis.

$$j_z = \frac{1}{2} \cdot \left(\frac{D_{bore}}{2} \right)^2 \tag{3.17}$$

"Steady" shearing of the charge motion can be used to characterize the production of turbulent kinetic energy [19, 86].

$$\frac{d}{dt} L_{dir,shr} = L_{dir} \cdot \Psi_{dir} \cdot \sqrt{k} \tag{3.18}$$

Hereby, Ψ_{dir} represents the decaying function for charge motion (a study on the decay functions together with a Taylor-Green vortex construction is performed in section 3.3). Equation 3.18 states, that actual turbulence values have a great impact on charge motion behavior and thus on later turbulent quantities. Hence, huge turbulent generation early in the engine cycle works against a good turbulence level at combustion.

Together, equations 3.13-3.18 can reproduce occuring tumble decay, swirl decline and following up turbulence production within the compression stroke.

3.2.5 Intake stroke (open valves).

The intake stroke sets up a more general problem for turbulence production. The incoming fresh charge builds up global charge motion ("turbulent potential") and generates intake turbulence directly. This is accounted for in an adapted production term for the intake which is solved together with mass balances:

$$dk_{prod} = dk_{prod,shr} + dk_{prod,int}. \tag{3.19}$$

Mean flow kinetic energy from inlet boundaries are therefore partially transformed in $dk_{prod,int}$. Thus, additional consideration of contributing flow components (mass flow and gas velocity) over the intake valves IVi is essential, compare indices' table 3.1. The aforementioned behavior of equation 3.19 later leaves starting values for a further calculation within compression and expansion stroke. The idea of kinetic energy conversion at the intake stroke is shown in figure 3.5. Main tumble L_x sets one important type of global charge motion. Tumble production caused by incoming charge within the intake stroke ($\dot{m}_{IVi} > 0$) writes

$$\frac{d}{dt} L_{x,IVi,int} = j_{xy} \cdot \dot{m}_{IVi} \cdot \mathrm{Tu}_{x,IVi} \cdot \omega_{mot}. \tag{3.20}$$

Thereby $\mathrm{Tu}_{x,IVi}$ is an equivalent for tumble generation, based on the steady state discharge analysis in 3D CFD (cf. appendix D.3). Keep in mind that the angular
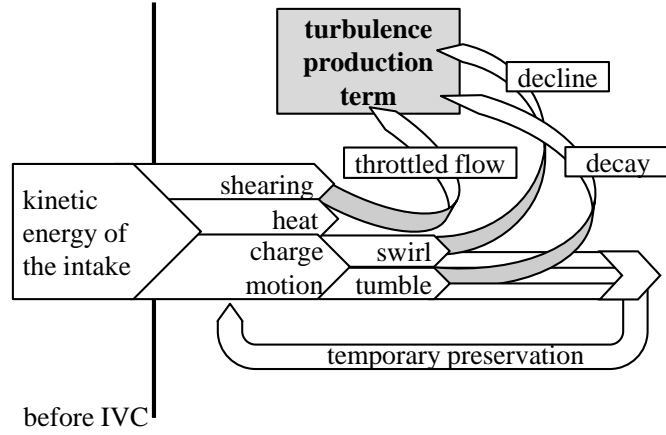
Figure 3.5: Modeling approach for fragmentation of kinetic energy from the intake. The intake flow feeds the energy cascade by creation of global charge motion (tumble and swirl) as "turbulent potential". Moreover turbulence production before IVC is increased by direct shearing of the incoming gas flow. Residual kinetic energy converts to friction heat.

velocity scales with engine speed via $\omega_{mot} = 2\pi \cdot n_{mot}$.

Swirl production caused by different incoming massflows ($\dot{m}_{IVi} > 0$) over IVi intake valves depends on differential entry of momentum ($\dot{m}_{IVi} \cdot \vec{v}_{IVi}$) and the lever $\vec{r}_{int}$. Note that the components of $\vec{r}_{int}$ and $r_{z,int}$ do have different signs for various valves.

$$\frac{d}{dt} L_{z,IVi,int} = \vec{r}_{int} \times (\dot{m}_{IVi} \cdot \vec{v}_{IVi}) \cdot \vec{e}_z \tag{3.21}$$

Due to valve masking (shadowing of the rear intake valve seat), the incoming gas mass flows mainly along the y-axis into the cylinder, compare figure 3.4 left. Thus, a high fraction of momentum can be used to generate swirl motion at small valve lifts. This allows a simplification of the cross product with $\vec{r}_{z,int} \perp (\dot{m}_{IVi} \cdot \vec{v}_{IVi})$ like in equation 3.22.

$$\frac{d}{dt} L_{z,IVi,int} \approx r_{z,int} \cdot \dot{m}_{IVi} \cdot v_{IVi} \tag{3.22}$$

Here $r_{z,int}$ induces an effective swirl lever (measuring approximately from intake valve center to the symmetry plane between both pairs of valves).

If massflow exits the cylinder through IVi valves ($\dot{m}_{IVi} < 0$), the loss of angular

momentum fraction writes

$$\frac{d}{dt}L_{dir,IVi,int} = L_{dir} \cdot \frac{\dot{m}_{IVi}}{m_{cyl}}. \tag{3.23}$$

Overall angular momentum change for IVi different valves combines as

$$dL_{dir,int} = \sum_{IVi} dL_{dir,IVi,int}. \tag{3.24}$$

Total tumble change at the intake stroke consists of shearing decay (destruction of angular momentum) and kinetic build up for all intake valves IVi. Hence, the conversion of main tumble to overall tumble works as in equation 3.25 ($C_{x,xy} \approx 1.05$, cf. appended figure D.1).

$$dL_{xy} = dL_{xy,shr} - C_{x,xy} \cdot dL_{x,int} \tag{3.25}$$

Overall swirl change at the intake stroke, consisting of shearing and a kinetic balance for all intake valves IVi, writes

$$dL_z = dL_{z,shr} + dL_{z,int}. \tag{3.26}$$

The build up of rotational energy $E_{rot,int}$ within the cylinder is fed from all charge motion in directions dir according to equation 3.15.

$$dE_{rot,int} = 2 \cdot \sum_{dir} \left(\frac{E_{dir,rot}}{L_{dir}} \cdot dL_{dir,int} \right) \tag{3.27}$$

Mean flow kinetic energy KE_{int} from the entering gas mass ($\dot{m}_{IVi} > 0$) for all intake valves IVi balances

$$dKE_{int} = \frac{1}{2} \cdot \sum_{IVi} \left(\dot{m}_{IVi} \cdot (\vec{v}_{IVi})^2 \right) dt. \tag{3.28}$$

Intake production considers how much of induced kinetic energy produces "instantaneous" turbulence right away. Thus, the difference between intake mean flow kinetic energy KE_{int} and global charge motion build up $E_{rot,int}$ is a measure for instant shearing turbulence. ($C_{prod,int}$ in equation 3.29 works as proportional factor and accounts for the turbulent efficiency at high dissipation rates for the intake flow.)

$$dk_{prod,int} = +C_{prod,int} \cdot \frac{dKE_{int} - dE_{rot,int}}{m_{cyl}} \tag{3.29}$$

Finally, the general turbulence production term for the intake stroke (equation 3.19) adds up shearing $dk_{prod,shr}$ and intake build up $dk_{prod,int}$.

69

The 0D turbulence model is now set up and can be evaluated for different engine operations. Figure 3.6 shows the function for a sample engine cycle at 2000RPM and 2mm mean intake valve lift, compare appendix C.2 (VVT). Due to intake phasing (valve
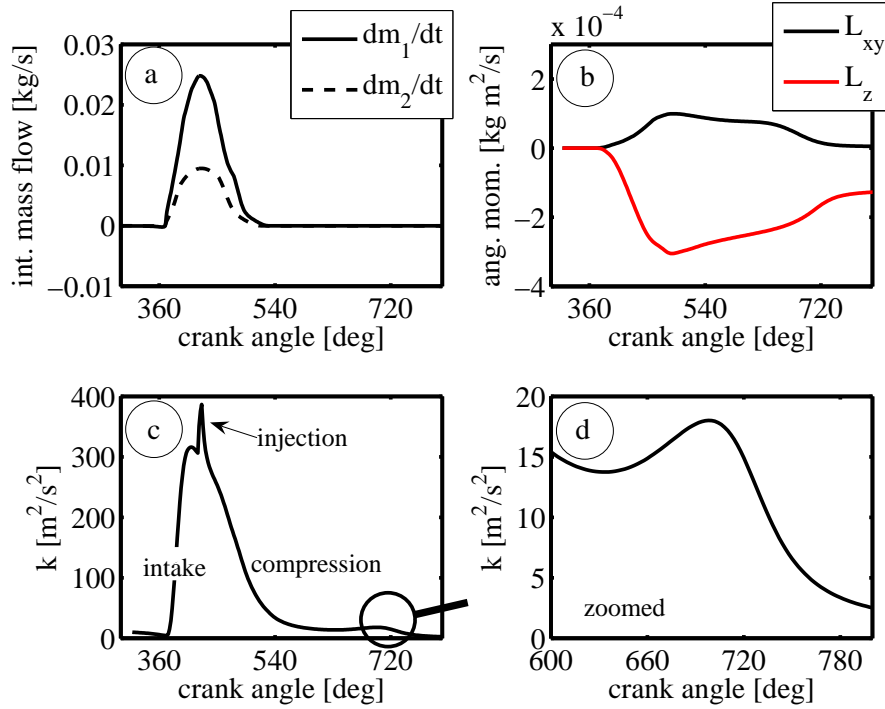
Figure 3.6: *New quasi-dimensional approach* for turbulence reproduction at sample operation with 2000RPM, 2mm valve lift and early IVC. Incoming mass flows over phased intake valves (a) and thus the build up of charge motion potential (b) cause turbulent build up (c,d) within the compression stroke.

lift curves differ), a differing mass flow dm_{IVi}/dt enters for each intake valve, figure 3.6 (a). Hence, there is not only created a tumble motion L_{xy} but also a swirl component L_z in the cylinder, figure 3.6 (b). In fact, the swirl component even dominates this engine operation, because an early valve closing at the intake inhibits further tumble build up. The little rest of tumble L_{xy} was mainly induced by the wider opening valve (around 90%) which improves its "tumble production ability" through higher valve lift (compare appended section D.3) and greater mass flow. The reaction of turbulence can also be seen in figure 3.6 (c) and zoomed in (d). As expected, there is a high peak at the very beginning of the cycle, caused by high intake velocities. This peak is enhanced by a short and early fuel direct injection. When entering the compression

stroke, there exists an abrupt gradient of turbulence destruction. Nearly at ignition top dead center (720degCA) occurs the last turbulence peak for this cycle. Here, the swirl motion transfers its long-lasting energy to produce small scale turbulence, which will later dissipate after ITDC. (A detailed comparison of the 0D turbulence model with CFD data follows in section 3.4 after the derivation of the decay functions Ψ.)

3.2.6 Turbulence interaction with heat release.

As there certainly exists a feedback from the propagating flame to turbulence, many authors have argued its modeling in different ways [32, 38, 68, 70]. A very common formulation yields the scaling of "unburnt turbulence" as found in the above model with a density ratio that considers combustion.

$$v' = v'_u \cdot \sqrt[3]{\frac{\rho_u}{\rho_b}} \tag{3.30}$$

Equation 3.30 evolves from an adapted conservation concept, related to the *rapid distortion theory* (RDT), with the turbulent flame surface as interface [103].
Lately, Linse [53] could constitute that an identification of the unburnt turbulent quantities is sufficient for resolution of turbulent burning velocities. He states that the estimation of s_T over the whole burning duration can be done without calculating combustion feedbacks to the turbulence model. The *"cold procedure"* not only speeds up the quasi-dimensional estimation but also alleviates the code which then needn't take into account enhanced turbulence at combustion in the terms of equation sets 3.2, 3.13 and 3.19. Thus, an adaption of the combustion model is not necessary.

3.3 An analysis of shearing effects.

As mentioned previously, charge motion and especially the tumble motion decays during compression. This decay is known to highly depend on the piston position and may be expressed as a function Ψ. In this section, the piston position dependence (geometric dependency) of Ψ is investigated considering its mathematic origin and using a simplified test case.
For the integration of the general shearing equation 3.18

$$\frac{d}{dt}L = L \cdot \Psi \cdot \sqrt{k} \tag{3.31}$$

it is assumed that Ψ and k are independent of time. The integration yields for $L(t)$ as Eulerian exponential function

$$L(t) = e^{\Psi \cdot \sqrt{k} \cdot t}. \tag{3.32}$$

Hence, for the initialized state $\{L_0, k_0\}$ at the starting time $t_0 = 0$, the decay function can be defined as gradient like

$$\Psi = \frac{1}{\sqrt{k_0}} \cdot \frac{d}{dt}\left(\frac{L}{L_0}\right)\Bigg|_{t_0}. \tag{3.33}$$

Equation 3.33 only considers shearing influences on angular momentum decay. Therefore, geometric boundaries like the moving piston and valves are frozen for this ODE initial value problem. The unit of the decay function Ψ is expected to act like an inverse length scale $[1/\mathrm{m}]$.

In order to determine the general shape of the decay function in equation 3.33, the following idealized set-up is investigated using CFD by

1. definition of the static cylinder geometry (piston position at a certain crank angle),

2. employment of the initial state $\{L_0, k_0\}$ for the whole cylinder gas mass,

3. unsteady analysis of charge motion decay over time.

For the initialization of the initial state in the cylinder, there was used a 3D CFD geometry of the *BMW N20B20* engine with all valves closed in the compression state, compare appendix A. The general aim was to keep angular momentum for the main tumble constant for different piston positions. Its mathematical form with the assumption of homogeneous density ρ writes

$$\vec{L} = \rho \cdot \int_{V_{cyl}} \vec{r} \times \vec{v} \, dV. \tag{3.34}$$

Here, the cross product of velocity field $\vec{v}$ and effective lever $\vec{r}$ is integrated in the cylinder volume V_{cyl}. Vector decomposition similar to equation 3.9 yields for the main tumble component

$$L_x \propto \int_{V_{cyl}} (r_y \cdot v_z - r_z \cdot v_y) \, dV \to \mathrm{const.} \tag{3.35}$$

Thus, the x-tumble depends on the levers r_y and r_z as well as on the velocity components v_z and v_y, compare figure 3.4. The lever in y-direction is fixed with cylinder bore and in z-direction there occurs a permanent change of the lever length according to the actual piston position which then writes

$$r_y \propto D_{bore} = \mathrm{const.}$$
$$r_z \propto s_{pist}. \tag{3.36}$$

For the initial flow field, this demands to adapt the velocity component v_y to constantly fulfill relation 3.35. The velocity vectors were initialized according to a simplified 2D

Taylor-Green vortex form like

$$\vec{v} = \begin{pmatrix} v_x \\ v_y \\ v_z \end{pmatrix} = \begin{pmatrix} 0 \\ \Gamma \cdot cos\,(y \cdot \pi/D_{bore}) \cdot sin\,(z \cdot 2\pi/s_{pist}) \\ sin\,(y \cdot 2\pi/D_{bore}) \cdot cos\,(z \cdot \pi/s_{pist}) \end{pmatrix}. \qquad (3.37)$$

In equation 3.37, y and z are spatial coordinates and Γ represents an artificial amplification of the originial velocity component v_y. Here, $\Gamma \propto (D_{bore}/s_{pist})$ ranges from 1..10 for the *BMW N20B20* and was chosen iteratively to get a constant main tumble component initialization L_x for piston positions near BDC and TDC as well, see equation 3.35. For the starting value of turbulent state k_0 in equation 3.33, there was performed a simple estimation which scaled mean velocity field v and velocity fluctuation v'.

$$v' = \sqrt{\frac{2}{3}k} \approx 2\% \cdot v \qquad (3.38)$$

Here, the mean velocity v was defined to value 25m/s at BDC. Therefore, the tumble initialization is completely defined.

These steps were repeated for different piston positions in the real cylinder geometry and the behavior of decays were investigated. The process of decay analysis combines several advantages: a convenient experimental set up, a high repeatability, a very well defined mathematical structure and predictable behavior of the Taylor-Green vortex as well as rather fast CFD evaluations (minutes up to few hours for long analysis time spans).

In figure 3.7 the CFD results for selected (numerical) tumble experiments are plotted for two sample piston positions. The chosen view shows a cross section of the y-z-plane with projected velocity vector plots of the decaying vortex. It can be seen how the induced tumble decays over time. After initialization, especially at the cylinder boundaries in figure 3.7 the vortex rapidly decays. The tumble cannot preserve its original shape because friction effectively causes its deformation. Once this cascade has started, the large scale motion is likely to vanish due to large gradients. Moreover, figure 3.7 makes evident that charge motion decay is linked with geometric boundary conditions. (Thereby, the initialization of the Taylor-Green fields aims at similar values for $\{L_0, k_0\}$.) The further a rotating motion is stretched or compressed, which means $s_{pist}/D_{bore} \neq 1$ in this manner, the faster the energy transfer away from large scales is. The measured time scales for reducing the tumble motion by a factor of 2 are therefore 24-25ms at 600degCA and only 6-7ms at 645degCA. The reason for this can be seen in gradually higher mean stress rates for the flow field at piston positions located nearer to TDC. These results for the conducted tumble experiments are illustrated in figure 3.8. Here the static decaying curves for angular tumble momentum were recorded for different crank shaft positions. The mean stress rates again drive the charge motion decay. The more the piston evolves to TDC, the faster the kinetic energy transfers
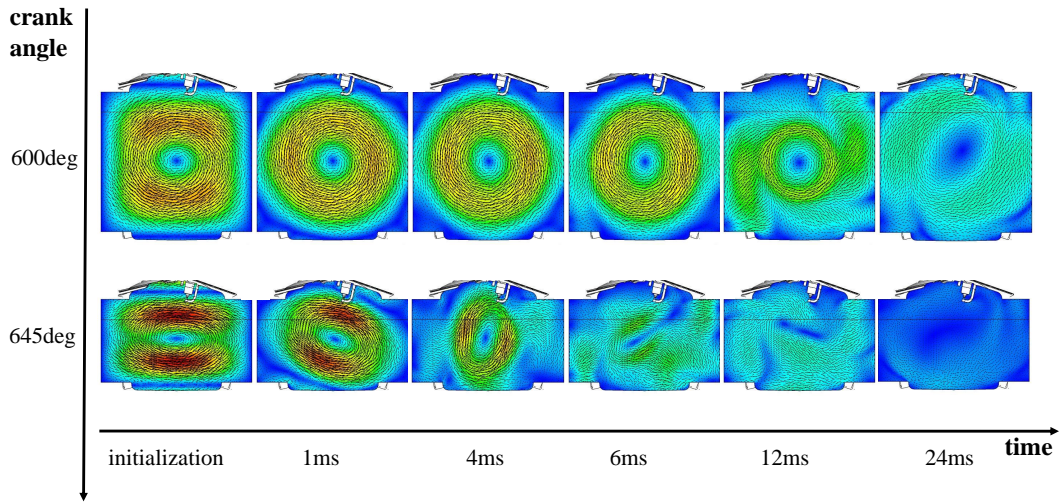
Figure 3.7: Static tumble decay of the Taylor-Green initialization in real combustion chamber geometries. Sample crank shaft positions at 600 degCA with $s_{pist}/D_{bore} = 1$ and at 645 degCA with $s_{pist}/D_{bore} = 0.61$. Velocity flow fields are equally scaled.
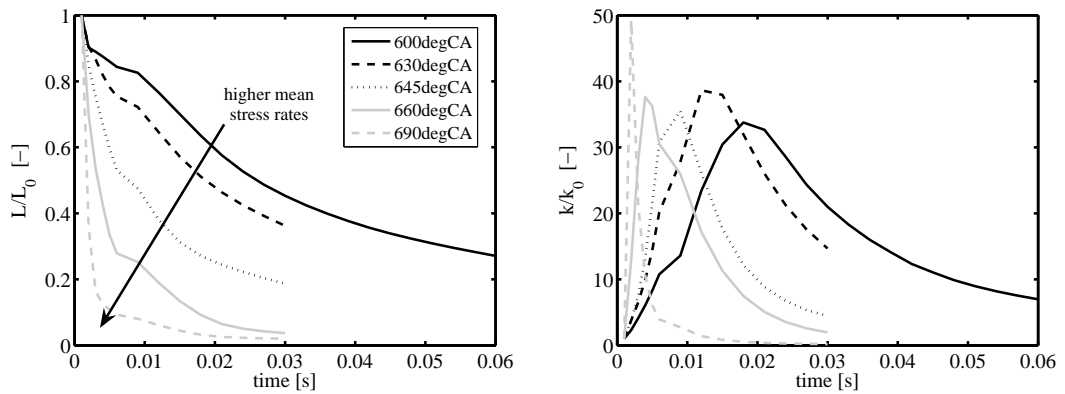
Figure 3.8: Static tumble decay versus time after 3D Taylor-Green initialization. Normalized reduction of global charge motion for different crank shaft positions (left) and according normalized turbulence development (right). Subscript "0" refers to the initialization state at $t_0 = 0$.
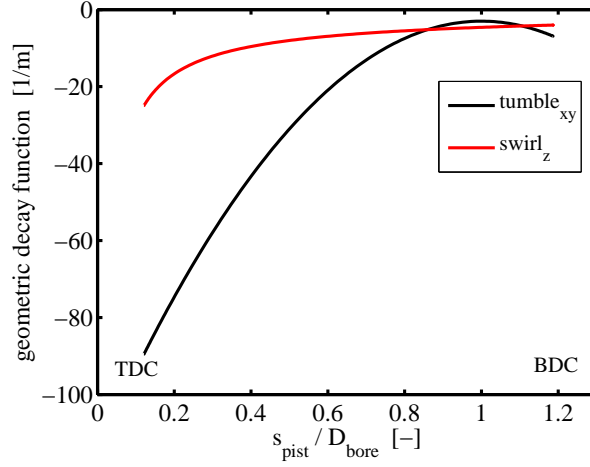
Figure 3.9: Resulting decay functions for different types of charge motion. Both curves were derived using numerical Taylor-Green experiments without piston motion.

into small scale turbulence, which can be seen in figure 3.8 in the right diagram. This results not only in earlier but also in higher turbulence peaks. (It must be stated, that for a piston position at BDC with $s_{pist}/D_{bore} > 1$, the tumble is also deformed from its most likely construction and decays fast. In the observed geometry, 600degCA forms the optimum combustion chamber shape for a long tumble preservation.)

The whole procedure of tumble decay observation can be transfered to swirl analysis with only the adaption of the Taylor-Green initialization. Therefore the velocity profiles have to be turned into the z-axis with the angular momentum conservation

$$L_z \propto \int_{V_{cyl}} (r_x \cdot v_y - r_y \cdot v_x) \, dV \to \text{const.} \tag{3.39}$$

and the fixed cylinder boundaries $r_x, r_y \propto D_{bore} = \text{const.}$, compare figure 3.4. Remaining experimental steps stay unchanged (initialization for different piston positions, unsteady analysis of decaying motion, calculation of decaying function Ψ_z).

Together with equation 3.33, the analysis of all results yield, that the decay function Ψ can be obtained with the slope of charge motion reduction at the very beginning of the calculation time. Figure 3.9 shows the different decay functions for tumbling gas motion (around x- and y-axis) and swirl motion (around z-axis). Approximated decay functions are of different nature when plotted versus normalized piston position.

Whereas the tumble decay has an optimum with least tumble destruction per time step, the swirl decline is monotonic along the piston movement from BDC to TDC. The reason is obvious: tumbling motion is rapidly deformed because it has its rotational axis perpendicular to the piston translation. Thus, the degree of geometric disturbance defines the gradient of tumble decay. The swirl decline function in figure 3.9 constitutes that the swirl motion is only "compressed". Its frictional forces are increasing whilst compression, but the swirl vortex can preserve its shape. Thus, the swirl motion is long lasting. Another consequence is the differing contribution to turbulence production between tumble and swirl. There again it is important to analyze them independently with later superposition. The shown plots in figure 3.9 are later on used for model calibration and validation.

Following the approach of Voisine et al. [109], an eddy turn over time τ_t can be defined for the tumbling motion via current piston displacement and mean cylinder velocity with

$$\tau_t \approx \frac{s_{pist}}{v}. \tag{3.40}$$

For the *BMW N20B20* crank train at 600degCA with $D_{bore} = s_{pist}$ and the mentioned velocity assumptions, this results in a turn over time τ_t of 3ms. As in about the same time, the tumble motion loses a high degree of rotational energy, see figure 3.7. Hence, kinetic energy decay scales with the tumble's turn over time.

3.4 Model calibration and validation with 3D CFD data.

3D CFD experimental set-up. In order to assure the right functionality of the introduced 0D turbulence model, a data basis with 3D CFD data had to be created. This data basis can provide the different types of charge motion, the turbulent state, turbulence dissipation and turbulent length scale at every evaluated crank angle of the cycle.

For simplification reasons, there were conducted adapted experiments of the dynamic discharge analysis in ANSYS CFX. This involves:

- starting the computation at IVO

- neglecting the early direct injection in 3D CFD

- neglecting the combustion in 3D CFD ("cold procedure")

- ending the computation after ITDC

Typical maximum mesh sizes range around 2-3million elements for a symmetrical type of charge motion (only tumble) and 4-6million elements for asymmetric types of motion. Impressed boundary conditions contain the valve timing and lifts on intake and exhaust side as well as constant pressures in the intake and at the exhaust (considering the

different engine load points) and a certain engine speed. The commercial code in ANSYS CFX contains the following models for this procedure: mesh movement, solution of the total enthalpy considering friction losses, k-epsilon turbulence model with a Kato-Launder production limiter and a scalable wall function model.

Results from the 3D CFD experiments were used in the following comparisons.

0D model calibration and validation. The introduced turbulence model was constructed upon physical basics. This allows a calibration of the production terms for k_{prod} with minimum effort. Furthermore, it is likely to only optimize the turbulence production terms from instantaneous intake turbulence, swirl decline and tumble decay with the help of the free parameters $C_{prod,int}$, $C_{z,prod}$ and $C_{xy,prod}$ (cf. equations 3.29 and 3.13). A run of a least-square optimizing routine can result in the following causality for the parameters

$$0.05 \approx C_{prod,int} << C_{z,prod} < C_{xy,prod} < 1.$$

Due to high dissipation rates at the intake valve gap, the high turbulent state is instantaneously dissipated and has no more influence at the beginning of the combustion. Following the difference between swirl decline and tumble decay, less turbulence can be produced from the long lasting swirl motion. Moreover, all production efficiencies are below 100% – obviously not all shearing energy can be transformed to turbulent potential.

The model calibration was performed at an engine operation with 2000RPM, *bmep* 2bar because this offers the occurrence of tumble and swirl motion at the same time, compare appendix C.2 (VVT). The used optimizing algorithm is based on a gradient determination for least-square error minimization and coupled with the *MATLAB* solver for the described equation set. The algorithm was given a criteria to match the peak height and quality of turbulence near ITDC. All found tuning parameters for the turbulence model were later applied unchanged to the upcoming comparisons from table 3.2.

For the validation it is important to note that the 3D intake flow shows a high complexity and is farly anisotropic. Following, it is neither expected nor important to rebuild the occurring local intake phenomena by a quasi-dimensional modeling approach. So the following plots concentrate on the comparison of all quantities after the closure of the intake valves. Nevertheless, the starting values at IVC are predicted by the 0D routine itself. Therefore equations 3.19-3.29 are applied over the whole duration of the opened intake valves, respectively intake valve opening (IVO) till intake valve closing (IVC). The initial values for turbulence and global charge motion at IVO are set according to

common practices in 3D CFD as

$$\{k,\ L_{dir}\}\ \bigg|_{IVO} = \left\{10\frac{m^2}{s^2},\ 0\right\}.$$ (3.41)

For the evaluation of charge motion build up, the air mass flows over the opened intake valves are provided by a gas change analysis.
It is widely known, that not only engine speed but also intake valve lift and timing have a great impact on turbulence and global charge motion. Therefore, the validation

operation state	engine speed	IV timing	IV lift	manifold pressure
swirl 1	2000RPM	early	2mm	ambient
swirl 2	2000RPM	early	4mm	ambient
tumble 1	2000RPM	late	max	ambient
tumble 2	6000RPM	mid	max	turbocharged

Table 3.2: Overview of 3D CFD results for quasi-dimensional model validation at the BMW N20B20 engine.

points from 3D CFD vary all these parameters within the *BMW N20B20* engine map, see table 3.2. In order to gain wide insights to 3D in-cylinder phenomena, the CFD set-ups were slightly simplified (e.g. by negligence of minor influences from the exhaust, injection and squishing on the general quality of turbulence). Thus, a variety of different CFD calculations could be performed very fast with original cylinder geometries.
The results of the comparison between 3D CFD and quasi-dimensional model are give in figures 3.10-3.13.
 In figure 3.10, there are shown the validation results for the *BMW N20B20* operation point *swirl 1*. Tumble component L_{xy} is matching quite well between 0D approach and 3D CFD. The 0D swirl motion L_z is underestimated in figure 3.10. Especially at IVC (beginning of the dashed lines), the initialization values for the compression stroke might be improved due to a very dominating swirl motion in reality. Nevertheless, the 0D turbulence quality k for *swirl 1* is predicted very well and lies within a $\pm10\%$ accuracy at 690degCA.
 In figure 3.11, the comparison between 0D approach and 3D CFD can be seen for the operation at *swirl 2*. Here, the swirl component L_z is less dominant compared to the tumble component L_{xy}. Both charge motions are predicted very well at IVC (beginning of the dashed lines) and in general quality by the 0D approach. Thus, the turbulence quality k in figure 3.11 also matches very well and lies within an accuracy of $\pm15\%$ at 690degCA.
 Figure 3.12 shows the comparison between 0D and 3D CFD results for the engine
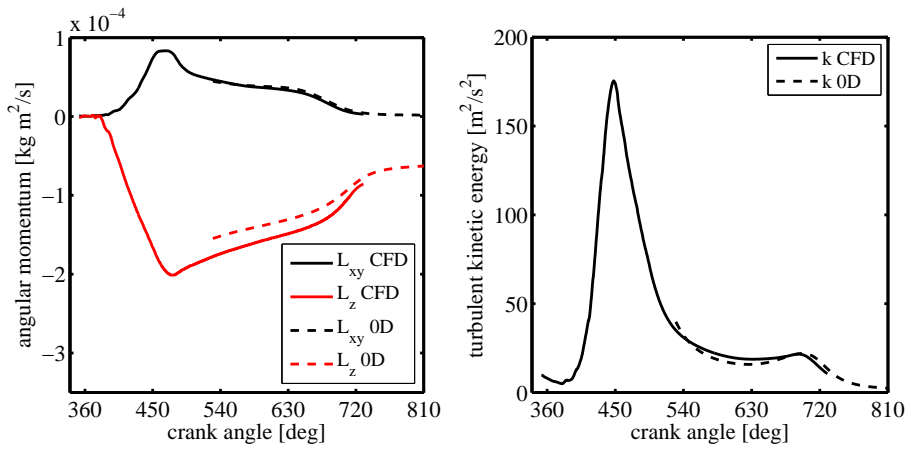
Figure 3.10: Validation of charge motion and turbulence for the BMW N20B20 engine at operation state *swirl 1*. Although swirl component L_z is underestimated by the quasi-dimensional model, turbulence development can be predicted quite well.
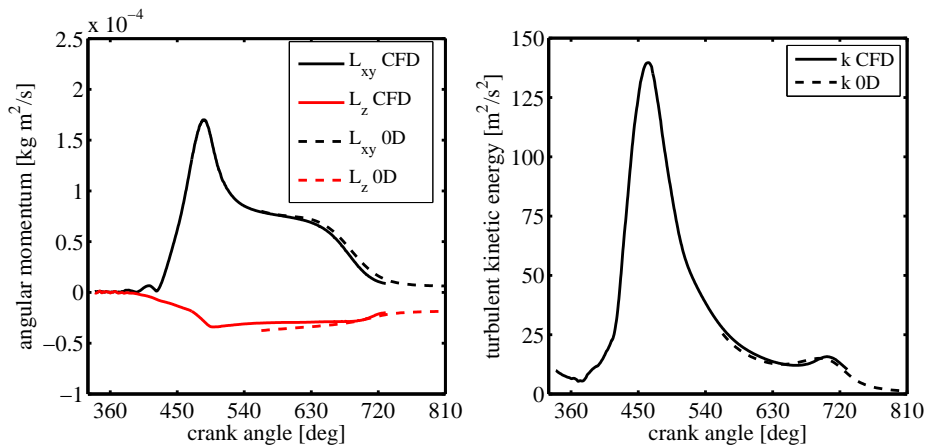
Figure 3.11: Validation of charge motion and turbulence for the BMW N20B20 engine at operation state *swirl 2*. The quasi-dimensional model fits the CFD results very well.
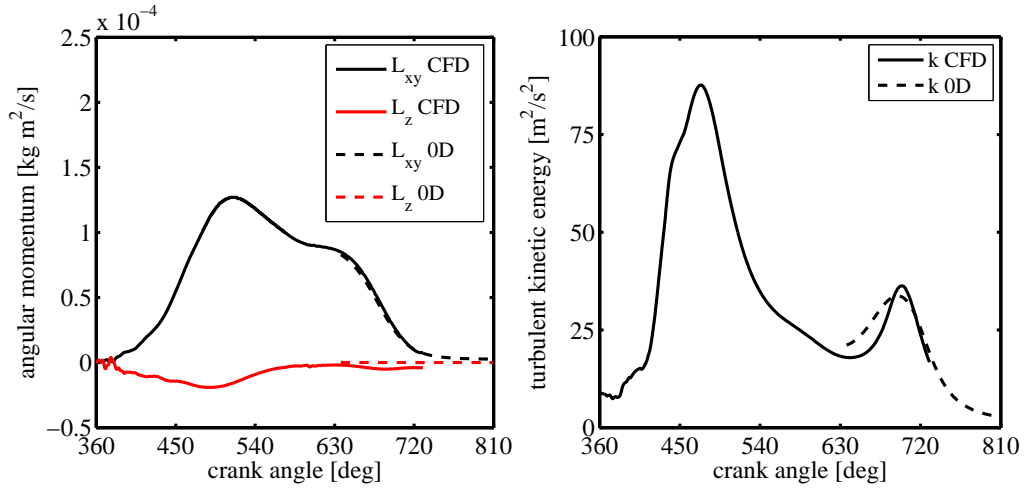
Figure 3.12: Validation of charge motion and turbulence for the BMW N20B20 engine at operation state *tumble 1*. Charge motion development matches well with CFD experiments. The turbulence peak of the 0D model is slightly too early and subsequently underestimated.

operation at *tumble 1*. It must be mentioned here, that for tumble operation the swirl component L_z at IVC should vanish in 3D CFD because both intake valves let enter the same air mass flow. The remaining L_z values in the 3D results evolve from inner cylinder flow field irregularities which aren't covered by the 0D equations. But compared with the amplitude of the tumble L_{xy} (10 times higher at IVC), these effects can be neglected. The tumble build up and decay are predicted very well by the 0D approach in figure 3.12. Turbulence k shows an earlier peak for 0D compared to 3D CFD. Its accuracy still remains within $\pm15\%$ at 690degCA but could be even improved with the help of a refinement between $C_{prod,int}$ and $C_{xy,prod}$.

Figure 3.13 illustrates the comparison between 0D approach and 3D CFD results for the high load and high engine speed operation *tumble 2*. Again the tumble motion L_{xy} is predominant for this point and predicted very well at IVC (beginning of the dashed lines) and in decay quality. But the 0D equations cannot reproduce the swirl component which exists at 3D CFD and even increases a little after IVC but seems negligible. Due to the high engine speed, the turbulence level k in figure 3.13 is very much higher at all times compared to the other validation points. Although the new 0D approach predicts the turbulence quality at 690degCA within a good accuracy of $< \pm10\%$ compared to 3D results, the peak occurs around 5degCA too early.

In summary, the produced model results lie within the expected confidence interval for

80
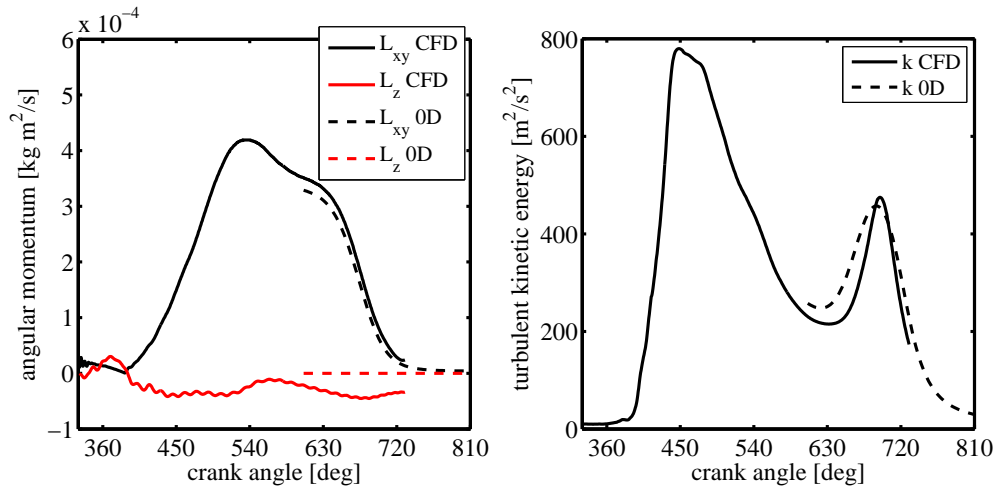
Figure 3.13: Validation of charge motion and turbulence for the BMW N20B20 engine at operation state *tumble 2*. Tumble L_{xy} is predicted well. The build up of swirl L_z *after IVC* cannot be reproduced by the 0D model. Again, the turbulence peak lies too early and slightly too low.

the turbulent burning velocity s_T (especially at 690degCA) and generally show a good quality.

3.5 Parametric study.

Quasi-dimensional modeling approaches allow a detailed view on equation behavior and also comprehensive parameter variations, which will both be done for turbulence in this section.

3.5.1 Fragmentation of mean flow kinetic energy from the intake.

It is desirable to understand the underlying physics for swirl and tumble generation and evolving differences at turbulence production. Therefore, the engine operation points *swirl 1* and *tumble 1* from table 3.2 were compared in detail with the help of the new turbulence model. The results can be found in figures 3.14 and 3.15. Both figures (left) consider the fragmentation of mean flow kinetic energy from the intake valves in a pie chart *at IVC*.

The balancing terms for the correlation are explained in the following. The underlying specific mean flow kinetic energy was calculated with the cylinder mass at IVC according
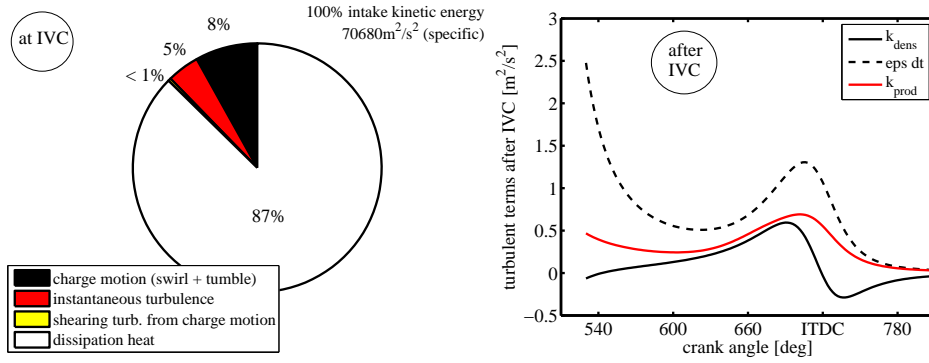
Figure 3.14: Intake energy fragmentation for *swirl 1* at IVC (left). There can only be transfered around 8% from a high level kinetic energy into charge motion. The following up development after IVC (right) shows a late decline of swirl motion in k_{prod}. Due to early valve closure, dissipation $\varepsilon \cdot dt$ destroys turbulence "starting levels" rapidly.

to the integral of equation 3.28 like

$$\text{ke}_{int}\ \bigg|_{IVC} = \int_{IVO}^{IVC} \frac{d\text{KE}_{int}}{m_{cyl}}\ dt. \tag{3.42}$$

This specific integral represents the intake's mean flow energy potential that might initiate global charge motion, turbulence and dissipation (friction) heat in the cylinder. Thus, the pie chart in figures 3.14 and 3.15 (left) correlates all mentioned parts to resulting equation 3.42. The specific charge motion energy at IVC is calculated again with the cylinder mass m_{cyl} at IVC, according to the rotational energy integration from equation 3.27 like

$$\text{e}_{rot,int}\ \bigg|_{IVC} = \int_{IVO}^{IVC} \frac{dE_{rot,int}}{m_{cyl}}\ dt. \tag{3.43}$$

Equation 3.43 represents the specific energy level that lies within charge motion at IVC and therefore correlated with equation 3.42 forms the black pie part in the charts of figures 3.14 and 3.15 (left). Furthermore, integration of equation 3.29 yields

$$k_{prod,int}\ \bigg|_{IVC} = \int_{IVO}^{IVC} dk_{prod,int}\ dt. \tag{3.44}$$
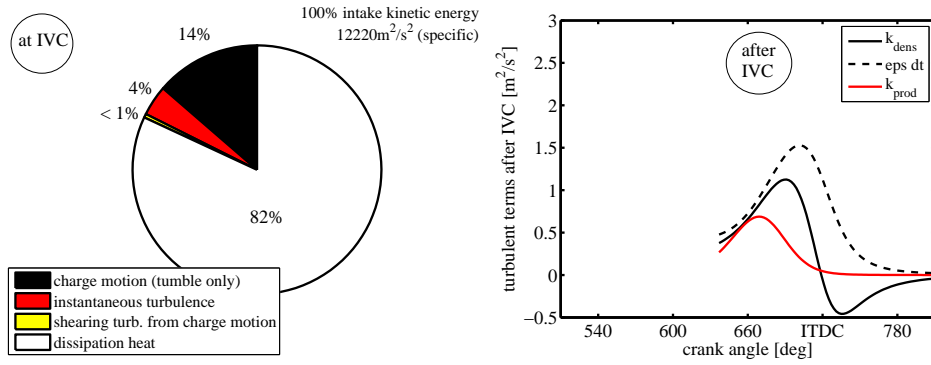
Figure 3.15: Intake energy fragmentation for *tumble 1* at IVC (left). There are transfered around 14% into charge motion energy. The following up tumble decay after IVC (right) contributes early to turbulence production. Afterwards, the density term k_{dens} plays a major role for combustion turbulence.

The correlation of this instantaneous turbulence level at IVC with equation 3.42 represents the red fragment in figures 3.14 and 3.15 (left). The following integration of equation 3.13 produces the shearing turbulence portion at IVC as

$$k_{prod,shr} \Big|_{IVC} = \int_{IVO}^{IVC} dk_{prod,shr} \ dt. \tag{3.45}$$

Note, that this turbulence portion only takes into account the shearing of *existing* charge motion (not shearing at the valves, which is considered in $k_{prod,int}$). The correlation of equation 3.45 and 3.42 yields the yellow pie part in the charts. For the pie chart completion, it is assumed that residual energy fractions transform completely into dissipation heat (great white portions in figures 3.14 and 3.15 (left)) like

$$\frac{f_{heat}}{ke_{int}} \Big|_{IVC} = 100\% - \frac{e_{rot,int} + k_{prod,int} + k_{prod,shr}}{ke_{int}}. \tag{3.46}$$

The right chart in figures 3.14 and 3.15 shows the curves for the dominating contributers in equation 3.2 *after IVC until the end of a probable combustion*. Therefore, some previously mentioned terms were isolated from the 0D model calculation after IVC and plotted for every time step: the turbulent density term k_{dens}, the turbulence production term k_{prod} and the dissipation term $\varepsilon \cdot dt$.

The following analysis of the fragmentation plots 3.14 and 3.15 *at IVC* yield some major differences between the operation points: It is to note, that the balance for *swirl 1* shows a 5 times higher mean flow intake kinetic energy. But it can only convert around 8% into cylinder charge motion at IVC, whereas the operation at *tumble 1* can nearly double that fraction with resting 14% at IVC. The absolute friction loss for the intake stroke is very much higher for *swirl 1* operation. The reason is a smaller valve lift with a smaller integral length scale at the intake stroke and hence higher dissipation rates ε. It is interesting to see, that *shearing of the existing charge motion* at IVC ($k_{prod,shr}$) is negligible for both engine operations within the intake stroke, compare figures 3.14 and 3.15 (left). When 3D CFD results show a high shearing turbulence at the intake stroke, the equivalent term in the 0D model is $k_{prod,int}$ which impacts significantly. (But it has to be remembered, that the 0D model won't resolve local turbulence peaks at the intake valve flow but can only consider cylinder averaged turbulence which will then be lower in comparison.)

Following the path of fragmentation *after IVC* in figures 3.14 and 3.15, one can also correlate the combustion relevant turbulence with the mean flow kinetic energy level from equation 3.42 straightforward like $k(ITDC)/ke_{int}(IVC)$. Here, only 0.02% (swirl operation) and a higher 0.2% (tumble operation) of the overall intake kinetic energy do survive as turbulence k at ITDC . Figure 3.14 (right) points this out by higher destruction rates $\varepsilon \cdot dt$ for swirl operation with early valve closure. The right curves in figures 3.14 and 3.15 show the impact of swirl decline (late and less rapid) and tumble decay (early and with high gradients) on turbulence production k_{prod} after IVC. Summarizing, the engine operation with swirl as main type charge motion is less effective for combustion turbulence. For this configuration, a tumbling gas motion creates highest fluctuations of the velocity field.

3.5.2 Reaction of turbulence on engine variabilities.

It has been shown so far that the proposed 0D turbulence model can recover the physical behavior (compared to CFD) within the limits required. The predictive model character is outline for this section regarding the *BMW N20B20* engine. Therefore, figures 3.16-3.18 show the one-by-one variation of parameters. The reactions of global charge motion L_{xy}, L_z and turbulence k are observed near ITDC at 690degCA. Here, the inherent change of cylinder masses m_{tot} comes as input from previous thermodynamic calculations.

In figure 3.16, the variation of intake valve timing can be seen for the operation point *swirl 1*. For later valve closure, general charge motion is promoted, especially considering the swirl component L_z. This enhances turbulence values at ignition. Moreover, cylinder air charge then increases. Nevertheless, it must be mentioned, that a late valve timing has negative effects on pumping losses within the gas change.

Figure 3.17 shows the influence of intake valve lift on turbulence. The intake valve lift
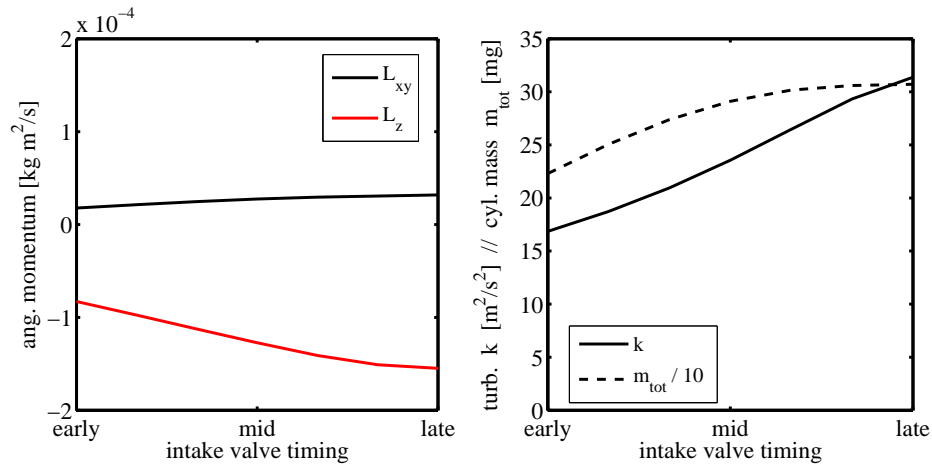
Figure 3.16: Variation of intake valve timing (60-115degCA a.TDC) for *swirl 1.* Shown recordings are instantaneous at 30degCA b.ITDC.
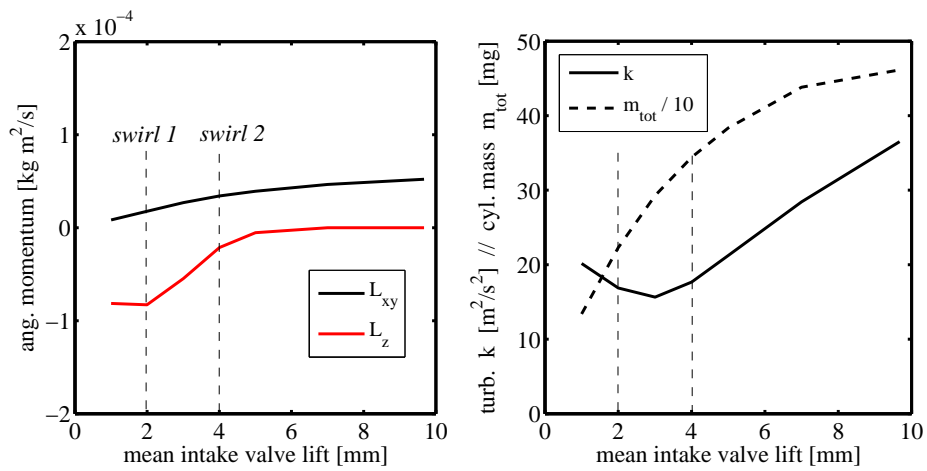
Figure 3.17: Variation of mean intake valve lift for *swirl 1.* Shown recordings are instantaneous at 30degCA b.ITDC.
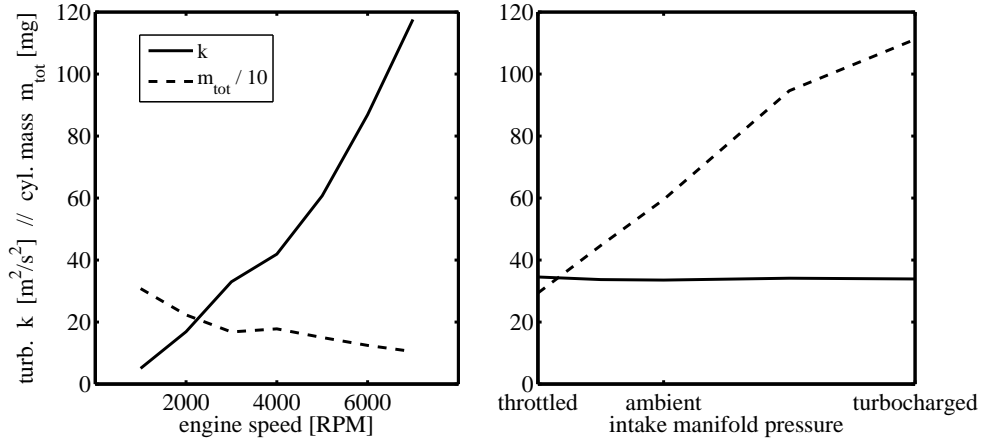
Figure 3.18: Variation of engine speed for *swirl 1* (left) and variation of intake manifold pressure for *tumble 1* (right). Shown turbulent states are instantaneous at 30degCA b.ITDC.

limits the incoming fresh air charge whilst unthrottled engine operation. Therefore, cylinder mass m_{tot} directly follows the mean lift. But another effect is very interesting here: the charge motion behavior changes rapidly. At small valve lifts, swirl L_z is dominating. Swirl intensity decreases with further intake opening, because pre-defined valve phasing (different valve opening) lessens. Near 6mm mean height, there is produced no more swirl component L_z. Tumble motion L_{xy} still is weak, but improves for higher valve lifts. In figure 3.17 there exists a minimum turbulence k before ignition at 3mm mean intake valve lift, because here the tumble motion cannot compensate the occurrence swirl loss. A comparison at maximum valve lift and a mean valve lift of 1mm shows that the degree of turbulence could be nearly doubled. This has an impact on burning durations, since a higher turbulent flame tends to burn faster and more efficient.

In figure 3.18, there are plotted two common phenomena as occuring in 3D CFD calculations. When varying engine speed, Linse [53] states that turbulence k before ignition and engine speed n_{mot} approximately follow the law

$$k \propto n_{mot}{}^a. \tag{3.47}$$

The behavior in figure 3.18 (left) can be fitted best with $a \approx 1.68$ for *swirl 1* operation. A variation of intake manifold pressure only shows negligible effects on turbulence. Although the cylinder mass rises with higher boost pressure in figure 3.18 (right), the turbulence before ignition as mass specific quantity is independent from that.

3.6 Summary and confidence interval.

The discussed turbulence model shall improve quality of predictions for turbulent burning velocities within the high pressure part of an engine cycle. In this approach, the turbulent production term can physically react on a change of engine operation (e.g. intake valve lift, intake valve timing, engine speed, boost pressure etc.). Moreover, the approach offers new charge motion quantities for the first time in 0D calculations. Nevertheless, there are few limiting situations, where the modeling principle is of less accuracy:

- generation of turbulence via exhaust flows

- feedback of turbulence on the gas exchange (slightly differing mass flows over the intake would impact on the next cycle's charge motion)

- influence of late direct injections with high rail pressure near ITDC (catalyst heating operation not yet observed)

- high valve overlaps inhere problems for 0D air charge determination, which the turbulence model then suffers of either

- special local turbulence phenomena cannot be resolved

- late generation of charge motion, that was not yet existent at IVC (compare figure 3.13)

- tumble and swirl interaction with each other (this disregards the assumption of superposition)

The identified cases can be seen as of little importance for most engine operations. Following, the introduced modeling approach is able to describe turbulence within almost the whole engine map.

4 Physical modeling of ignition delay.

Preface for ignition modeling. Parts of the discussed physical model refer to the master thesis of Daleiden [14], which I supervised during my time as doctoral candidate.

4.1 Introduction.

The time span between the formation of a spark (external energy supply) and the detectable heat release of combustion is called *ignition delay*. Most conventional SI engines realize this external energy supply via a spark plug that ionizes the fresh gas and initiates radical reactions and fuel break down.

In this work, the term *ignition delay* relates to the duration from ignition angle α_{ign}, which symbolizes the sparking event, to the flame development crank angle α_5, where 5% of the bulk mass are burned.

$$\Delta\alpha_{idel} = \alpha_5 - \alpha_{ign} \tag{4.1}$$

This formulation seems applicable, because with it, engine measurements can be analyzed with higher repeatability and better signal-to-noise-ratio for pressure indication. (Pressure indication behaves noisy directly at ignition timing which worsens the possibility to analyze early heat release states with 1%, 2% etc. burned mass fraction.)

Figure 4.1 shows the flow chart of the 0D combustion model. It starts with a description of the laminar flame s_L and the interaction with turbulence leading to s_T. For an established turbulent flame, the heat release rate and with that the cylinder pressure can be derived (assumed the geometric flame surface is known, cf. section 5.2.2). Figure 4.1 also shows the actual knowledge gap in grey marked boxes: between sparking event and turbulent flame propagation, there lies an important transition phase. Here the flame speed ranges between laminar and fully turbulent propagation and hence influences the whole process afterwards. The ignition phase deals with rather small flame volumes and is therefore highly dependent on local effects. The resolution of major influences on ignition delay marks a greater challenge for quasi-dimensional modeling.

4.1.1 Necessity for physical description of ignition delay.

It is important to note the significance of ignition delay for the overall quality of combustion. Thus, figure 4.2 shows several effects of ignition offset from measured single cycles at the *BMW N20B20* engine. The measured duration from flame development
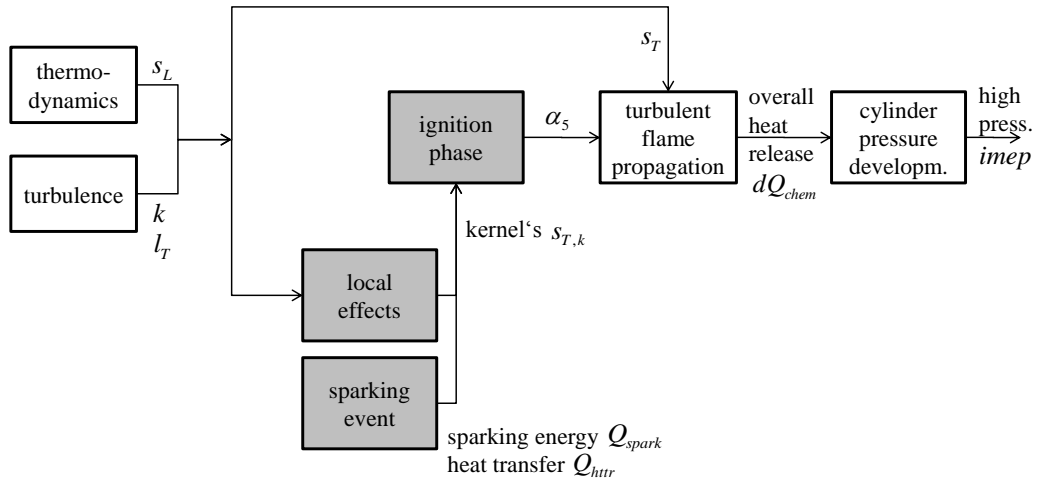
Figure 4.1: Flow chart of combustion modeling for SI engines. The knowledge gap for ignition delay is marked (grey).

angle α_5 to the CA50 angle α_{50} nearly stays constant for a shift of ignition timing (a). This accounts for a wide range of engine operating points and shows, that a deviation in prediction of ignition delay duration $\Delta\alpha_{idel}$ automatically transfers this deviation to later stages of combustion. Moreover, the combustion center α_{50} has a high impact on the indicated mean effective pressure $imep$ of the high pressure engine cycle, compare figure 4.2 (b). This means that the combustion center describes the effectiveness of the combustion process for engine torque generation. Summarizing, the quality of ignition delay models influences significantly the quality of the whole combustion prediction. Figure 4.2 (c) also shows a relative sensitivity analysis of $d\,imep/d\,\alpha_{idel}$ for spread measurements in the engine map. From that it can be stated, that for reaching an accuracy for high pressure $imep$ of better than 6%, the *mean ignition delay* must be predicted as close as ± 3degCA compared to correct values.

4.1.2 A brief discussion of cyclic variations in 0D.

Cyclic variations are a complex characteristic in spark ignited engines. The name "cyclic variability" induces that there occur differences between consecutive engine cycles which can be observed from a macroscopic point of view. Here, especially in-cylinder pressure, engine torque production and emission forming are subject to fluctuations. Even for stationary engine operation (constant mean actuators) it is not possible to avoid cyclic variations. An understanding of possible causes and their consequences are basic for
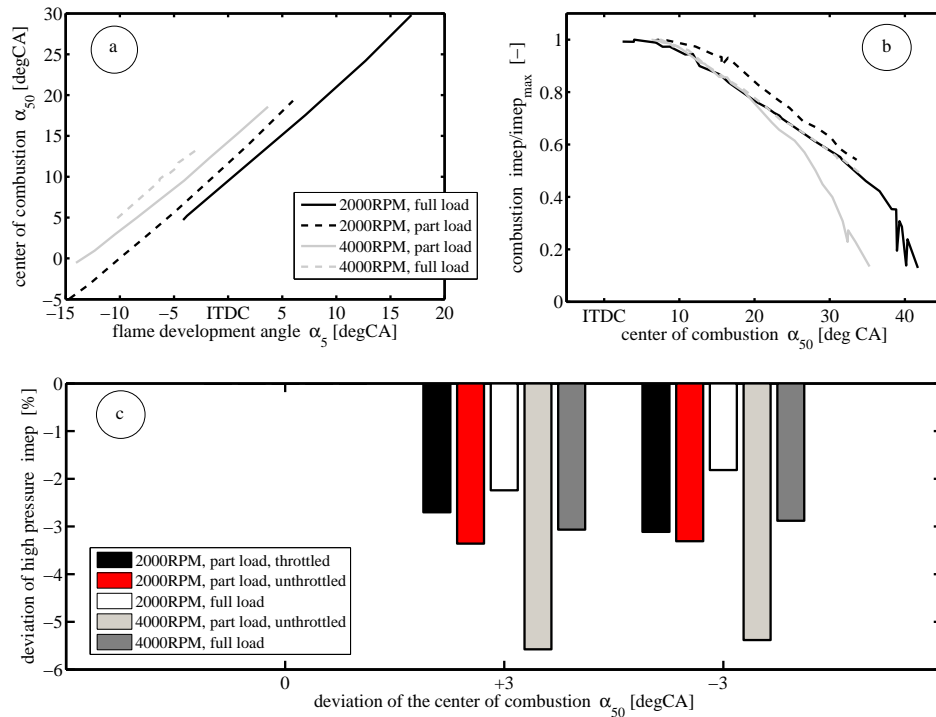
Figure 4.2: Measured single cycle events at the BMW N20B20 engine with pressure indication. Relationship between flame development angle α_5 and combustion center α_{50} (a). A deviation of the crank angle of 50% mass burned α_{50} (CA50) directly influences the quality of calculated mean pressure at combustion *imep* (b,c).

assuring a secure and proper engine operation. Up to now, there doesn't exist a full explanation of cyclic variations neither in experiments, nor detailed or reduced models. Hence, the topic is objective to many research works. A current project, conducted by Bargende [110], summarizes the expected influences leading to cyclic variations to be the following:

- in-cylinder flow field
  - fluctuating local flow structures at the spark plug, instantaneous at ignition timing
    * initial convection of the spark channel [78]
    * mixture fluctuation at the spark plug

* degree of residual gas homogenization (high local gradients correlate with cyclic instability) [114]

– fluctuating global turbulence (k, l_T) changes the flow field [72, 96] (decline of swirl motion, decay of tumble motion)

• fluctuating burn-off phase at the ending expansion cycle

– conversion efficiency η_c (formation of HC and CO)

– duration for complete mixture burn-off

– quenching of the flame at cold walls

All identified effects that are initiated within the ignition of the mixture at the spark location will show influence until the end of combustion. Thus, ignition delay plays a central role for cyclic variations [75].

The challenge for ignition delay modeling now shows in the interpretation of local effects at ignition timing on a quasi-dimensional basis. The derived model showed a good quality of prediction for averaged engine cycles (over some 100cycles) within the whole engine map. Thus, it can be stated, that there exists a behavior of ignition related variations that allows a good 0D modeling of averaged engine cycles: the "good" distribution for flame development angles α_5 can be seen in figure 4.3 (left). Not only
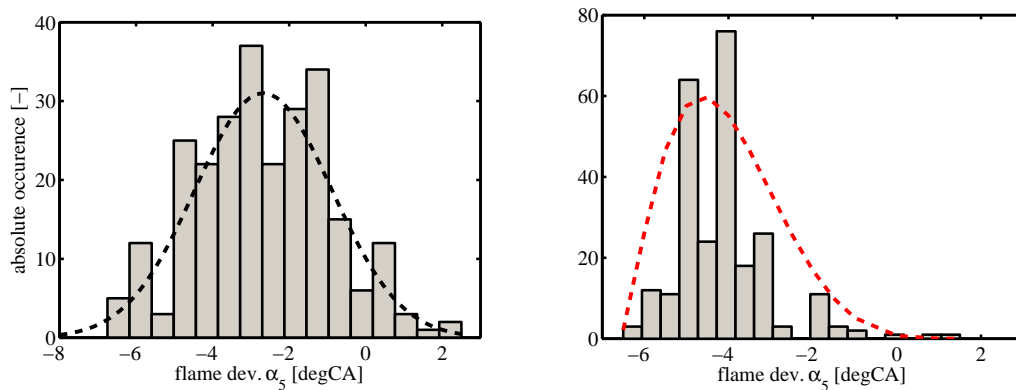
Figure 4.3: Fitted probability distribution of flame development angles α_5 from indicated measurements for 256 consecutive cycles at the BMW N20B20 engine. A "good" distribution of cyclic variations is symmetric to its mean value (left) and can be modeled adequate with a 0D ignition delay approach. A "bad" distribution behaves asymmetric refering to its mean value (right) and is hard to reproduce.

the standard deviation for consecutive stationary cycles should be small, but also the distribution of α_5 should behave symmetric. Thus, a "good" ignition delay distribution for single cycles shows a compensating effect. Slowly burning cycles alternate with fast burning cycles due to cyclic variations. In a measurement of some 100 consecutive working cycles, the averaged angle α_5 compensates to a "good" mean value which values around -3degCA for the example in figure 4.3 (left). In consequence, a slow burning cycle will be partially compensated with a fast burning cycle for the averaged cylinder pressure. If in contrast to marginal variation, consecutive combustion phases spread widely and behave asymmetric in distribution, cf. figure 4.3 (right), the modeling for mean engine quantities gets rough. Here a non-compensating effect occurs for averaged engine cycles: while the "bad" mean value for α_5 ranges around -4.5degCA, some very slow burning cycles occur within the averaging for combustion mean pressure. This lets the most extreme cycles be far away from modeling results with only averaged input quantities. Those complicated operation points occur sometimes at very low engine loads, high residual fractions as well as at engine idling and very late ignition timings.

4.2 Governing physics.

The ignition initiates the regular combustion process within SI engines. It seems appropriate to assume several simplifications that make the complex ignition accessible for 0D modeling: the local mixture at the spark plug is ignitable, the flame front propagates spherically and the kernel size is increased by expansion (especially shortly after ignition). At the beginning of combustion, the laminar flame speed drives the kernel propagation and afterwards the turbulent flame speed becomes more and more important [37]. Hereby, only turbulence structures smaller or equal to the actual kernel size are contributing to a turbulent flame propagation [10].

4.2.1 Approaches to ignition delay.

For the sparking event itself, there exists the the commonly accepted view that it consists of three stages, which are namely the *breakdown of the spark*, the *arc phase* and the *glow discharge* [38, 59]. The ionized plasma is formed within the spark breakdown, which lasts only nanoseconds. (Best ignition conditions can be found at slightly rich mixtures, high pressures and temperatures. Here, the needed sparking energy minimizes.) The arc phase afterwards is driven by expansion of the high temperature bulk gas and lasts few milliseconds. The dominating phase for quasi-dimensional ignition modeling is the *glow discharge*, which is modeled by most approaches. In this phase, for several milliseconds energy from the spark is transfered to the cylinder mass. Pischinger and Heywood [77, 78] formulate the energy budget for the initiated flame kernel (indexed

k) as follows:

$$\frac{d}{dt}U_k = \frac{d}{dt}\left(Q_{spark} + Q_b - Q_{httr}\right) + h_u \cdot \frac{d}{dt}m_k - p \cdot \frac{d}{dt}V. \tag{4.2}$$

Equation 4.2 describes the first law of thermodynamics for the kernel control volume, which includes the spark plug. The change of internal energy U_k therefore sums up from the external energy supply $\dot{Q}_{spark}$, the heat release $\dot{Q}_b$ and the heat losses to the spark plug electrodes Q_{httr} as well as the change of enthalpy through kernel propagation into the unburned gas h_u and the differential working term pdV. Pischinger reports, that the term $\dot{Q}_{spark}$ vanishes for the glow discharge phase [78]. With appropriately rearranging and the assumption of constant heat capacities c_p, Ewald [20] obtained a temperature change for the initiated kernel dT_k, which writes

$$\frac{d}{dt}T_k = -\frac{T_k - T_{ad}}{m_k} \cdot \frac{d}{dt}m_k + \frac{\eta_{\text{eff}}}{m_k c_p} \cdot \frac{d}{dt}Q_{spark} + \frac{1}{\rho_b c_p} \cdot \frac{d}{dt}p. \tag{4.3}$$

In this manner, T_{ad} describes the adiabatic flame temperature and the term η_{eff} concludes that heat supply from the spark plug and heat losses to the spark plug are connected via an efficiency multiplier. Ewald [20] later neglects the pressure term dp for the evaluation of only small time spans $\Delta\alpha_{idel}$, whereas Wiese [114] considers at least polytropic influences with an exponent of $n = 1.35$. Furthermore, Ewald mentions to initialize the ODE for the kernel temperature in equation 4.3 with values for $T_{k,ini} = T_k(t = 0)$ literally ranging from at least T_{ad} up to 60,000K. Wiese adapts the model equation 4.3 and initializes the kernel's size with typical electrode gaps of 0.6-0.8mm for homogeneous SI engines [114]. To close the problem's equation set, the kernel mass burning rate is formed as

$$\frac{d}{dt}m_k = \rho_u \cdot s_{T,k} \cdot 4\pi r_k^2. \tag{4.4}$$

Ewald [20] describes the reduced turbulent burning velocity, considering flame kernel curvature as

$$s_{T,k} = \max\left(s_L, s_T - \frac{2}{r_k}\left(D_0 + D_t'\right)\right). \tag{4.5}$$

This shows, that a small kernel initialization leads to long time spans, where the flame only propagates with laminar flame speed s_L. Besides spherical flame propagation, if there is assumed to be no early flame-wall interaction and no blowing-out of the spark caused by too high velocities at the plug, the kernel radius can be determined from burned volume V_b as

$$r_k = \sqrt[3]{\frac{3}{4\pi}V_b}. \tag{4.6}$$

For evaluation of $s_{T,k}$, the flame diffusivity at the inner layer x_0 (inner layer temperature T_0) is needed and can be formed according to Smooke [98] for cyclic hydrocarbons (e.g. aromatics like C_6H_6). In this approach it is applied to regular gasoline fuels as

$$D_0 = \frac{1}{\rho_u} \cdot \frac{\lambda_b}{c_p}\bigg|_{x_0} \approx \frac{1}{\rho_u} \cdot 2.5810^{-5} \left(\frac{298}{T_0}\right)^{0.7}.$$ (4.7)

Moreover the effective turbulent diffusivity writes

$$D_t^{'} = \sqrt{\frac{c_\mu c_s}{2 Sc_t}} \cdot l_{f,t} \sqrt{k_k} \approx 0.207 \cdot l_{f,t} \sqrt{k_k}.$$ (4.8)

Peters [74] notes that the turbulent flame brush thickness scales with the turbulent length scale l_t and is a time dependent function of the turbulent turn over time scale t_t like

$$l_{f,t} \propto l_t \sqrt{1 - e^{-c_s t/t_t}}.$$ (4.9)

Accordingly, scaled effective turbulence (only turbulent length scales smaller or equal than the kernel size $2r_k$ interact [20]) yields

$$k_k = k \cdot \min\left(1, \left(\frac{2r_k}{l_t}\right)^{2/3}\right).$$ (4.10)

In summary, the model needs a *focusing on the transition from laminar flame propagation s_L after ignition to the development of a turbulent flame.* Ewald [20] and Wiese [114] both switch their models to solve the G-equation in 3D after certain criteria such as $r_{k,end}$ or α_{end} are reached. At this point the scalar G-field of the flame surface can be resolved in 3D discretization. This shows that the 0D initialization of a later CFD flame calculation is very useful. Nevertheless, the goal of the new 0D model for ignition delay does not include local information at any time. Neither a burn rate equation for different 3D cells is solved, nor there is a local flow field available to the approach. Thus, a procedure must be derived for purely quasi-dimensional usage.

4.2.2 Derivation of a 0D capable model.

The aimed ignition delay model shall provide the physical prediction of the time span $\Delta\alpha_{idel}$ in 0D like defined in equation 4.1. The general approach of Ewald [20] must be adapted to reach that goal, because

- no 3D information is available for the 0D model

- no G-equation is solved simultaneously at any time of the starting combustion

- geometric restrictions of the flame propagation occur even before 5% burned gas mass fraction (wall touching) [38]

Kernel temperature Starting with equation 4.3 for the kernel temperature, one can evaluate the importance of the summed terms separately with the help of a thermodynamic engine cycle simulation. (This simulation is provided with the current cylinder pressure, unburned cylinder temperature and the fuel's burned mass fraction from a pressure trace analysis.) The appropriate initialization of the temperature T_k for an operation at 2000RPM/2bar (throttled) at the *BMW N20B20* engine (compare appended sections A and C.2) yields that for the model's ODE

- the heat release term $-\frac{T_k - T_{ad}}{m_k} \cdot \frac{d}{dt} m_k$ is of *great importance* especially for the early stages after ignition. T_k will then diverge from cylinder temperature T_{cyl}. (The term's value rapidly decreases to $-1.5 \cdot 10^5 K/s$ after initialization.)

- the energy supply term $+\frac{\eta_{\text{eff}}}{m_k c_p} \cdot \frac{d}{dt} Q_{spark}$ is of *little importance* in the discharge phase. It can be compensated by several orders of magnitude with the initialization of T_k. (Its value at ignition lies around $7 \cdot 10^2 K/s$ and vanishes at the end of ignition delay because ignition voltage and current were shut off previously.)

- the term of pressure rise $+\frac{1}{\rho_b c_p} \cdot \frac{d}{dt} p$ is of *medium importance* depending on ignition timing. For ignition angles around ITDC the term dominates at late phases of ignition delay. (Here, at $\alpha_{ign} \approx 40$degCA b.ITDC the term values a low $< 1 \cdot 10^5 K/s$ and develops according to the location of maximum pressure rise up to $< 2 \cdot 10^5 K/s$.) For very late ignition timings in the expansion stroke its influence vanishes.

These results allow to use a two zone thermodynamic analysis for T_k evaluation. It is assumed that
$$T_k \approx T_b$$
and therefore the burned temperature can be taken for further evaluations. Moreover robustness of the overall combustion model is increased by dropping one extra equation.

Turbulent flame brush thickness A model comparison could show that the formulation for turbulent flame brush thickness by Schmid [92] is better suited than the transient equation 4.9.
$$l_{f,t} = l_f + c_{f,t} \cdot l_t \cdot \sqrt[4]{1 + \frac{1}{Da^2}} \tag{4.11}$$

While this formulation normally accounts for fully developed turbulent flames, its handling is very predictable and $c_{f,t}$ can serve as calibration factor. Herefore, Ewald mentions in the ignition phase that the assumptions for $l_{f,t}$ are ad-hoc and should

pragmatically help the modeling [20]. Thus, Schmid's correlation will be used in the following.

Keeping in mind the new formulation for $l_{f,t}$ yields $D'_t >> D_0$. (There can be found a factor of 30..85 between D_0 and D'_t after ignition for a sample operation at 2000RPM/2bar (throttled) at the *BMW N20B20* engine.) For the transition of the burning velocity from laminar to turbulent state, this means

$$s_{T,k} \approx \max\left(s_L \ , \ s_T - \frac{2D'_t}{r_k} \right) . \tag{4.12}$$

Geometric restrictions of flame propagation   The analysis of spherical flame propagation from ignition event up to the angle α_5 yields that around 15% of cylinder volume are occupied at the end of ignition delay [38]. Daleiden [14] repeated the simulations with a pan cake shaped combustion chamber and found that for early part load ignition timing the flame touches the walls early before 5% mass burning occur. The kernel radius r_k is therefore one to three times bigger than the actual cylinder height, depending on the engine operation. This makes clear that flame-wall overlap cannot be neglected (fractions of the effective flame surface A_k are shadowed).

$$A_k(r_k) = 4\pi r_k^2 - (A_{head} + A_{liner} + A_{pist}) \tag{4.13}$$

Equation 4.13 accounts for the reduced flame surface by subtraction of projected areas of the quenched flame at head, liner and piston. A more detailed look on the flame surface model can be found in section 5.2.2.

Burning duration and ignition pressure influence   The modeling of ignition delay can be performed with a simple two-zone model considering a burned and an unburned zone. Nevertheless it seems useful, adding an interface between both, which describes the reaction zone processes [30, 31, 65]. This "pseudo zone" inherits unburned characteristics and now conversion time scales of the combustion are available as overall model calibration parameters. The idea behind that *entrainment approach* (compare section 5) is, that unburned gas mass is at first included (entrained, index e) into the reaction zone of the kernel, quite similar to equation 4.4.

$$\frac{d}{dt} m_{e,k} = Ex \cdot \rho_u \cdot s_{T,k} \cdot A_k \tag{4.14}$$

Thus, while the entrained mass fraction $dm_{e,k}$ is determined by the unburned density ρ_u, the turbulent burning velocity of the kernel $s_{T,k}$ and the flame surface A_k, it gets amplified by the expansion factor Ex which is described section 5.3.

After entrainment, the conversion of reaction zone gases can begin. This process is finite in time and can be described with an ODE, telling that only entrained masses can be

converted (burned, index b), cf. equation 4.15. (Conversion $dm_{b,k}$ follows entrainment $dm_{e,k}$.)

$$\frac{d}{dt}m_{b,k} = \frac{m_{e,k} - m_{b,k}}{\tau} \tag{4.15}$$

The conversion performs continuously within multiples of the characteristic time scale τ (further details in chapter 5). Here. it can be seen the advantage of the *entrainment approach*: for quasi-dimensional modeling approaches without local resolution of influences on the combustion, more modeling parameters are available than in a bare flamelet approach. Thus, entrainment equations allow a better separation of flame propagation and subsequent conversion.

Entrainment equation 4.14 deals with the amplifier Ex, which accounts for the burned gas expansion after ignition. It is defined as density ratio between unburned and entrained zone as

$$Ex = \frac{\rho_u/\rho_e}{(\rho_u/\rho_e - 1) \cdot x_e + 1}. \tag{4.16}$$

Fraction x_e compares the amount of entrained mass to total cylinder mass. The behavior of expansion factor Ex at different crank angle positions can be seen in figure 4.4 for a variation of cylinder air charge (engine load). At the very beginning of combustion with
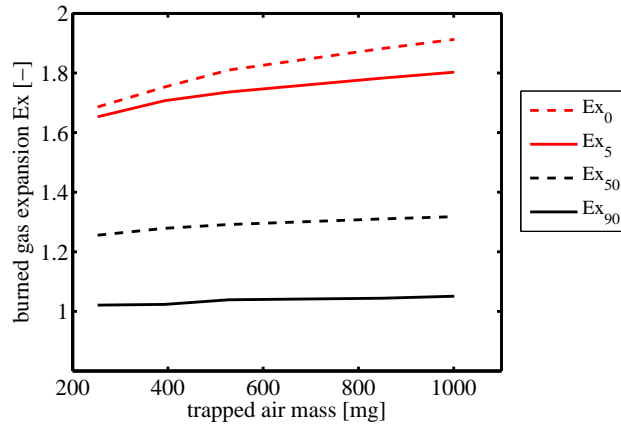
Figure 4.4: Expansion factor Ex at different stages of combustion (ignition, 5%, 50% and 90% burned fraction). The diagram shows a variation of engine load on the abscissa. Expansion effects are most important for the beginning combustion and relativise with proceeding burned fractions. The slope of the curves versus cylinder air charge enhances the modeling of shorter ignition delays at higher pressures.

0% mass burned, Ex_0 responds strongly to higher loads. It causes the ignition event to proceed faster for higher pressures at ignition. This corresponds to practical experiences, where ignition delays shortens for higher pressure at the same time. The difference between expansion factors for part load and full load amount to 10-15% within the ignition delay phase $\Delta\alpha_{idel}$. Figure 4.4 also shows that the impact of expanding bulk gas lessens with proceeding combustion. The expansion factors at 50% burned gas mass Ex_{50} and quite at the end of combustion Ex_{90} tend towards unity. Thereby, Herweg's ideas of expansion effects are confirmed [37].

In summary, within ignition delay modeling the application of an *entrainment approach* with expansion effects Ex helps

- separating the processes of flame propagation at the flame front and total mixture conversion within the reaction zone as well as

- describing the accelerating effect of high ignition pressures on ignition delay times (without contradicting the lowered laminar flame speed).

4.3 Model calibration and validation with measurements.

For the introduced ignition delay model, it is aimed to adjust only few parameters for a map wide calibration. These are namely:

- $c_{f,t}$, changing transition gradients from s_L to s_T (equations 4.5, 4.8, 4.11)

- c_{Ex}, changing the impact of expansion factor Ex (equation 4.16)

The fine-tuning of ignition delay values was performed with a standard optimizing algorithm (gradient determination) to minimize the sum of squared errors when comparing the deviation between ignition delay of measurement and simulation. The investigated engine was a *BMW N20B20* and measurement points for input data were spread according to the distribution in appendix C.1 with a special emphasis on part load, which seems more critical. The fitting procedure was performed at first for the aforementioned 6 standard load points before the obtained and unchanged parameter vector was applied in a simulation of the whole engine map.

Validation results can be seen in figure 4.5. (The ignition delay α_{idel} of the measurement was repeatedly derived from equation 4.1 with the fast heat release analysis, regarding cylinder pressure indication data.) Expectations are met in wide ranges of the engine map. Nevertheless, cyclic variations at low engine loads must be discussed specifically, because their single cycles are distributed like in figure 4.3 (right). Here, the model constantly calculates too short ignition delays.
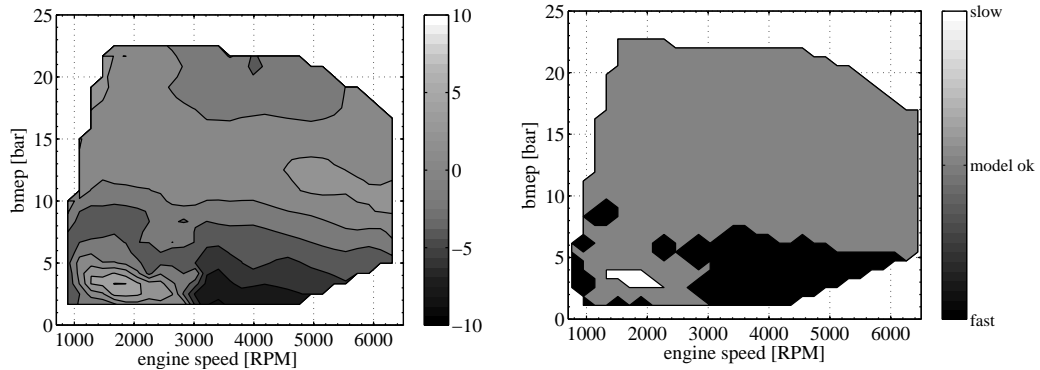
Figure 4.5: Validation results for ignition delay prediction (predicted - model) as absolute deviation [degCA] (left). A grey bit determines whether targeted accuracies of $+/-$3degCA are reached (right). Areas with greater deviation from averaged measurements occur at high residual fractions (model too slow) and at highly fluctating engine cycles in the measurement (model too fast).

Model accuracy for highly fluctuating operation   This section compares how strongly fluctuating in-cylinder quantities affect modeled single cycle ignition delays $\Delta\alpha_{idel}$ and if extrema meet measured data.

For cyclic variations, Wiese reports about differences of 10% for the air-fuel ratio (AFR) between measured values in the exhaust (lambda sensor) and local values at the spark plug during ignition [114]. While this seems plausible for averaged cycles, earlier optical measurements could even show a greater deviation of 15% for single cycles, compare figure 4.6 [26, 46]. It should be kept in mind, that at the end of ignition delay time spans, the flame kernel already has huge volumetric dimensions. Actually, it would be inconsistent to link cyclic variations just back to AFR deviations and no other quantity [110]. (If one ignores this fact, within 15% of the cylinder volume there would have to be the very much richer or leaner regime. This is not anymore a local effect and thus doesn't seem appropriate.)

Daleiden [14] performs a detailed analysis of parameters to observe the impact of local effects on modeled ignition delay $\Delta\alpha_{idel}$. The results are summarized in table 4.1. The unburned temperature T_u provides a great source for local variations of laminar burning velocities. This effect usually appears together with a residual gas stratification in the cylinder. Some own 3D CFD calculations and further optical measurements could show, that this "stratification effect" of temperature and residuals occurs to small extents at ignition timing [46, 52]. Thus, the use of a quasi-dimensional model should allow a satisfying accuracy for ignition delay.
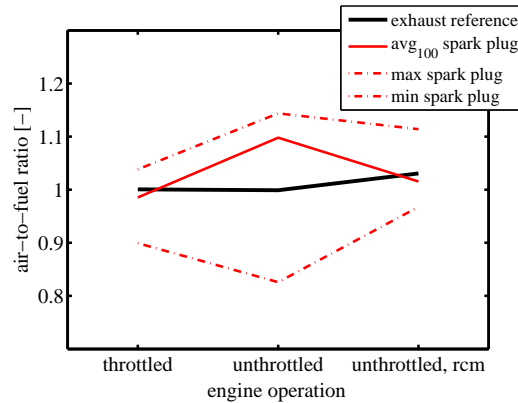
Figure 4.6: AFR fluctuation out of optical engine measurements for throttled, unthrottled operation, normal and with reduced charge motion (rcm) [26, 46]. The averaged local value over 100 cycles avg_{100} differs up to 10% from exhaust gas afr, while for single cycles the spread increases even to around 15%.

local quantity	induced dev.	influence on $\Delta\alpha_{idel}$	reason
pressure	+/-5%	small	Δs_L negligible
temperature	+/-10%	high for low loads	Δs_L huge
air-fuel ratio	+/-5%	small	Δs_L negligible
res. fraction	+/-10%	high for high res. frac.	s_L formulations
turbulence	+/-20%	small	little turb. interaction

Table 4.1: Assessment of local effects on ignition delay for 0D modeling.

Figure 4.7 shows an example for the fluctuation of single cycle angles α_5 for consecutive combustions. Here, the definition for a *margin of fluctuation* can be derived for the 50 fastest and slowest burn rates (dashed lines) and is a macroscopic value for engine roughness evaluation. Then, figure 4.8 summarizes the critical operation points of validation plot 4.5 with respect to cyclic variations of the measured data. Its ordinate axis holds the deviation between modeled values and measurement, while on the abscissa the operation points are listed in ascending order for engine roughness. It can be seen, that model deviations almost always lie within the *margins of fluctuation* for 50 extreme cycles. Some outlying operations touch the boundary of absolute fluctuation for α_5. Summarizing, this result seems very satisfying, because at least the worst and best burning cycle can be reproduced with averaged input data for the 0D ignition delay model. The overall engine map holds a required accuracy of $\pm 3 degCA$ at marginally
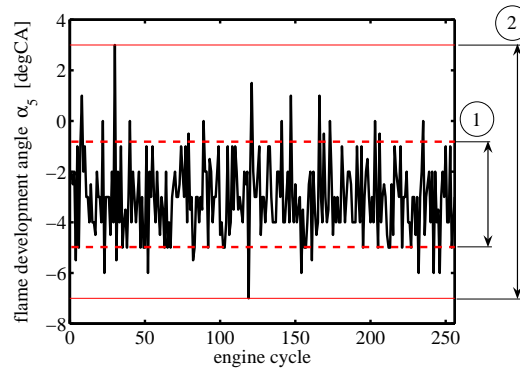
Figure 4.7: Definition of the *margin of fluctuation* (1). Resulting combustion angles α_5 for a highly fluctuating sample measurement are plotted. The margin of fluctuation for each 50 extreme cycles averaged (dashed lines) serves as robust benchmark for the heaviness of cyclic variations. Absolute fluctuation of consecutive cycles (2) include outliers.

fluctuating cycles.

4.4 Parametric study.

It was stated, that unburned temperatures T_u have a great impact on ignition delay, compare table 4.1 and section 2.1.1. Hence, in this section "one-by-one" variations for the *BMW N20B20* engine are performed, which act directly or indirectly on temperature. The responses of the introduced ignition delay model are plotted in figures 4.9-4.11. (The CA50 angle α_{50} is also shown for illustration of the following combustion effects and evolves from the modeling in section 5.) The parametric study also shows the turbulent burning velocities of the kernel $s_{T,k}$ within the transition phase from minimal s_L values to greater s_T values after ignition. Therefore, the plots 4.9-4.11 (right) contain a velocity plateau after ignition, where the slowest kernel propagation is limited to laminar flame speeds s_L, compare equation 4.5. The end of ignition delay at α_5 is characterized by a little unsteadiness, where the propagation velocity $s_{T,k}$ is set equal to a fully turbulent propagation s_T, compare equation 4.12. (The right term $-2D_t'/r_k$ would otherwise always decelerate the flame propagation.) This re-set of burning velocities is therefore needed for the overall combustion model and doesn't introduce negative effects on burning rates, because the gradient's unsteadiness is filtered via the second entrainment equation 4.15.

Figure 4.9 shows a variation of engine load at constant ignition timing. As expected,
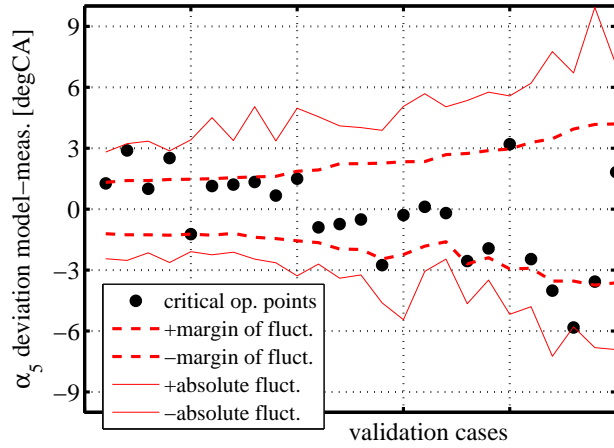
Figure 4.8: Deviation of predicted and measured flame development angles α_5 within the defined *margin of fluctuation* from figure 4.7 (dashed lines) [14]. The physical approach for ignition delay modeling allows to predict engine operations at least within their absolute fluctuation.
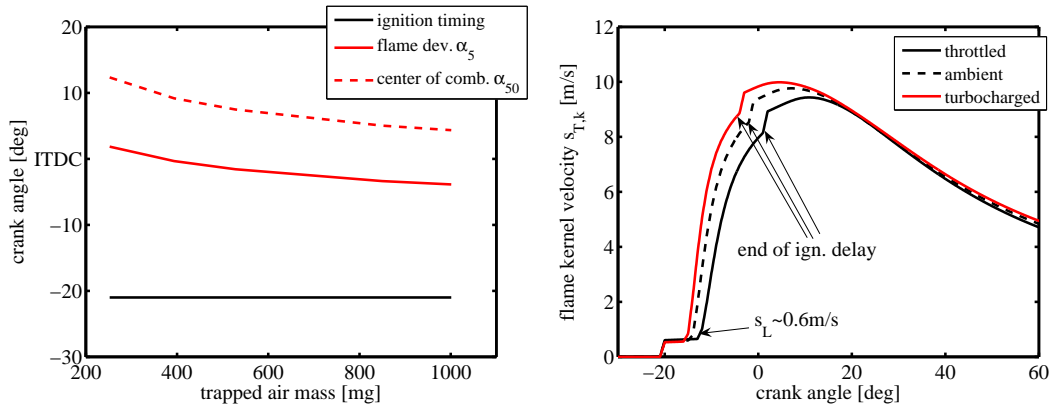
Figure 4.9: Modeled reaction of ignition delay for a variation of cylinder air charge starting at reference engine operation *tumble 1*, compare table 3.2. For constant ignition timings, the angle α_5 occurs earlier for higher boost pressures (left). The differing kernel propagation after ignition causes faster ignition delays (right).
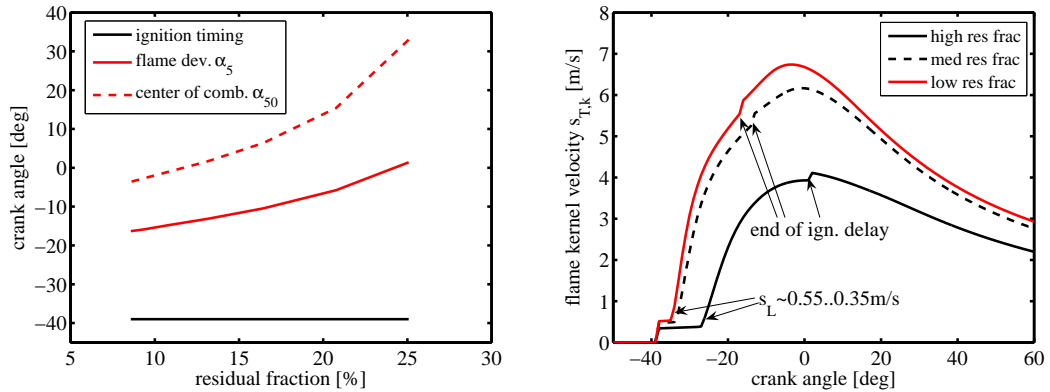
Figure 4.10: Modeled reaction of ignition delay for a variation of residual gas fractions starting at reference engine operation *swirl 1*, compare table 3.2. For constant ignition timings, the angle α_5 reacts highly sensitive (left). The kernel propagation velocity $s_{T,k}$ drops down to 60% from low to high residual fractions (right).

the ignition delay shortens for higher loads. This can be traced back to a faster burning (higher gradient of $s_{T,k}$). The starting value of laminar flame speeds in figure 4.9 (right) behaves very equal, caused by compensating effects of the thermodynamic model (cf. section 2.6).

Figure 4.10 plots the residual variation in the cylinder. Ignition delay reacts highly sensitive on that change - high residual fractions decelerate reaction rates. It must be mentioned that common formulations of laminar burning velocities s_L lack appropriate handling of residual fractions greater than 20% [61].

The variation of ignition timing is performed in figure 4.11. It is interesting to note, that the flame development α_5 does not only shift linearly with changing ignition angles. Due to very different thermodynamics, the slope follows exponential rules. For comparably late ignition timings, this can even lead to misfire because of very delayed and slow ignition processes. The later the combustion begins in the expansion stroke, the harder it is to ensure a secure ignition event. Misfire in figure 4.11 is characterized by unrealistic late angles α_5 and α_{50}. Moreover it occurs an increase of residual fractions in the cylinder because misfiring operation changes the pressure ratios in the exhaust muffler.
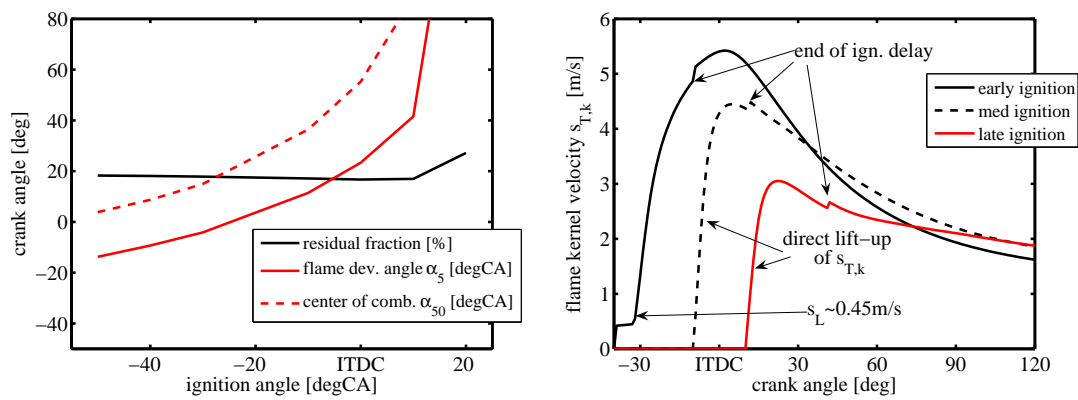
Figure 4.11: Modeled reaction of ignition delay for a variation of ignition timing starting at reference engine operation *swirl 1*, compare table 3.2. A later ignition timing not only shifts the angle α_5 but can also lead to misfire for very late timings (left). The propagation velocity peak $s_{T,k}$ drops dramatically for later sparking events and describes bad initial conditions for upcoming burn-off (right).

4.5 Summary and confidence interval.

The introduced mean value model can calculate the ignition delay $\Delta\alpha_{idel}$ for a 0D combustion model with the help of the outputs from thermodynamic and turbulence modeling (see sections 2 and 3). Therefore, the start of combustion from ignition angle to 5% burned gas fraction is considered, using a physical approach which identifies the turbulent propagation velocity of the initiated kernel. The model thereby takes into account early flame expansion and occuring geometric restrictions for the flame propagation (wall touching). The accuracy of prediction within the engine map yields satisfactory results. For highly fluctuating engine cycles, the model delivers results within the *margins of fluctuations*, if fed with averaged input data.

It has to be noted, that ignition delay prediction can only be as good as its inputs from thermodynamic and turbulence models for the evaluation of s_L, s_T and hence $s_{T,k}$. The input's confidence intervals have been defined previously. For very high residual fractions (especially if looking at external exhaust gas recirculation), proper formulations for laminar burning velocities s_L might improve the model's behavior.

5 Combustion modeling based on a 0D entrainment approach.

5.1 Introduction.

Quasi-dimensional combustion models have used the entrainment idea for the past three decades with considerable success. In comparison with mixing controlled modeling, the entrainment approach is not limited to regimes where mixing is slower than chemical kinetics. Moreover, considering flamelet modeling, inner flame reactions needn't take place on only length scales smaller than the Kolmogorov scale [104]. This becomes important for slow engine speeds and high mixture dilutions. Hence, the phenomenological entrainment idea offers a treatment of chemical processes and flow field interaction in a very wide range of engine operations. (Compared to a multi-dimensional flamelet approach, the entrainment model lacks the ability to break down the thin layer combustion to a modeling of the flame surface development via burning and advection.) Generally the flame in a quasi-dimensional model is assumed to be of trivial shape, because local deformations of the turbulent flame cannot be spatially resolved, compare figure 5.1. The 0D entrainment model divides the combustion chamber into three
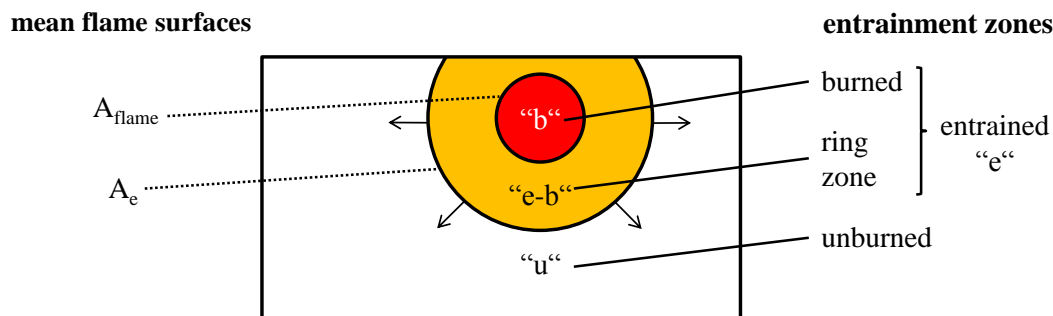
Figure 5.1: Multi-zone division for thermodynamics in the entrainment model.

elementary zones:

1. the unburned zone "u" with homogeneous fresh mixture educts

2. the burned zone "b" with the products of a complete reaction

3. in between evolves the entrained but not yet burned ring "e-b" (the whole entrained zone "e" contains the burned masses also) with intermediate stages of the global one-step reaction

With this zonal division, the entrainment model is able to compute instantaneous heat release rates, the density jump within the flame front and compression of unburned mixture, which is subject to the overall model validity [104].

5.2 Basic equations for entrainment combustion.

In general, the entrainment approach distinguishes between mixing determined processes for the turbulent flame propagation and chemical processes for the following mass burnout.

5.2.1 Mass entrainment and burning.

When it comes to regimes, where mixing controlled modeling and the flamelet approach lack accuracy (compare introduction 5.1), the *two-equation entrainment approach* may improve results. Unburned masses are ignited immediately via the entrainment equation according to Blizard and Keck [8]

$$\frac{dm_e}{dt} = \rho_u \cdot A_e \cdot u_e. \tag{5.1}$$

A major difference compared with the flamelet approach occurs, which lies in the considered effective reaction surfaces (averaged geometric evaluation of a sphere). For the entrainment model, the "entrained surface" A_e is much bigger than the "burned surface" A_{flame} of the flamelet approach according to expansion effects. Both surfaces can be seen in figure 5.1.

In the basic equation 5.1, ρ_u is the unburned mixture density and the quantity u_e describes the entrainment velocity with which the unburned eddies are entering the reaction zone. There exist several approaches for its formulation in literature [3, 60, 68]: The simplest correlation

$$u_e = v' + s_L \tag{5.2}$$

scales $u_e \propto v'$ for higher degrees of turbulence, which is not perfectly consistent with experiments needing earlier ignition timings for higher engine speeds.

Other authors include the turbulent burning velocity from experiments and sometimes a flame kernel transition

$$u_e = s_T. \tag{5.3}$$

Recent works could find that a boost of entrainment velocity u_e considering flame expansion could improve results tremendously. Thus, the current approach in this work

uses Lämmle's expansion factor [57] and is in good agreement with measured data.

$$u_e = Ex \cdot s_{T,\text{eff}} = \frac{\rho_u/\rho_e}{(\rho_u/\rho_e - 1) \cdot x_e + 1} \cdot s_{T,\text{eff}} \tag{5.4}$$

Here, the entrained mass fraction $x_e = m_e/m_{cyl}$ relates to the overall cylinder mass. Moreover it shall be mentioned for the effective turbulent burning velocitiy to be

$$s_{T,\text{eff}} = \begin{cases} s_{T,k} & \text{if } m_b/m_{cyl} < 0.05, \\ s_T & \text{else.} \end{cases} \tag{5.5}$$

s_T is typically determined according to Peters' correlation [74] as in equation 5.6 and $s_{T,k}$ was already derived for ignition delay in section 4.2.

$$\frac{s_T}{s_L} = 1 - \varsigma \cdot \frac{l_t}{l_F} + \sqrt{\left(\varsigma \cdot \frac{l_t}{l_F}\right)^2 + 4\varsigma \cdot \frac{v' \cdot l_t}{s_L \cdot l_F}} \qquad \varsigma = 0.195 \tag{5.6}$$

Figure 5.2 plots the mentioned formulations of the entrainment velocity u_e in equation 5.1. Whilst without adaption $v' + s_L$ and s_T are too slow in the overall process to
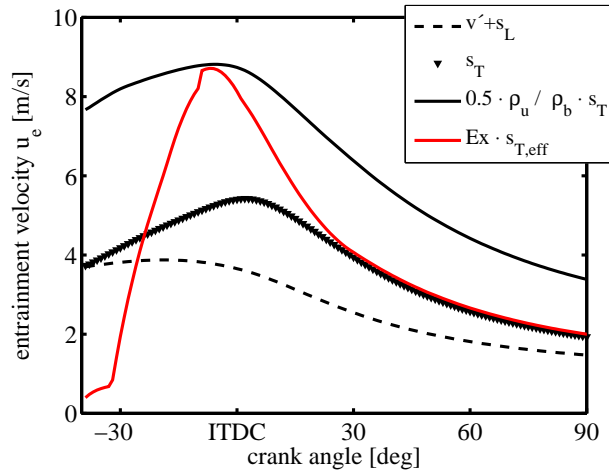
Figure 5.2: Comparison of entrainment velocities u_e from literature for an engine operation at 2000RPM/$bmep$ 2bar (VVT), cf. appendix C.2 for the BMW N20B20 engine. The new modeling approach $Ex \cdot s_{T,\text{eff}}$ inheres the ignition phase with small burning velocities, flame expansion and an asymptotic burnout phase with ordinary turbulent propagation.

entrain the whole unburned mixture before the flame reaches the walls, the formulation

$\rho_u/\rho_b \cdot s_T$ values much higher and leads to rapid fuel consumption gradients resulting in high pressure gradients. The new approach from equations 5.4 and 5.5 is the only one which starts at a laminar propagation after ignition, subsequently overtakes the turbulent burning velocity within the middle of combustion and burns out the remaining masses near cylinder walls with turbulent s_T. (It is known that inflammation and burn out are very much slower compared to the middle of combustion, where the flame finds optimum conditions.) Summarizing, the model covers widely varying propagation speeds in the process. After eddy entrainment took place, the bulk gas burnout can be described as laminar process on smaller length scales [8, 107].

$$\frac{dm_b}{dt} = \frac{m_e - m_b}{\tau} \tag{5.7}$$

Hence, the characteristic time constant is determined with the idea, that discrete micro volumes burn inwardly with laminar chemistry. It forms

$$\tau = \sqrt{\frac{15 \cdot l_t \cdot \nu}{v'}} \cdot \frac{1}{s_L} \tag{5.8}$$

and ranges around several $10^{-1}ms$. The difference between mass entrainment and mass burning is literally compensated within few degrees crank angle.

From this discussion, it becomes clear that a considerable degree of empiricism is included in the entrainment model formulation. Thus, it differs significantly from approaches such as flamelet. However, from 0D/quasi-dimensional viewpoint, which alway requires a certain amount of model adjustments, such an approach is feasible since it contains important physical ideas.

5.2.2 Determing the effective flame surface.

As obvious in equation 5.1, a reliable determination of A_e is needed for every discrete time step of the calculation. (The difference between the reaction zone surface A_{flame} and the entrainment zone surface A_e can be seen in figure 5.1.) It was already mentioned, that a quasi-dimensional modeling approach cannot predict local deformations of the flame front. Hence, the mean entrainment surface is calculated with simple approaches introduced by Blizard and Keck [8] and Morel et al. [65]. Their implementation is plotted for an example time step in figure 5.3, which combines the following key assumptions:

- perfectly spherical flame propagation

- center of the flame at a fixed coordinate (independent from the real ignition source at the spark plug)

- pancake shaped combustion chamber and flat piston geometry

- wall contacting parts of the flame are defined as "dead" (switched inactive for further entrainment)
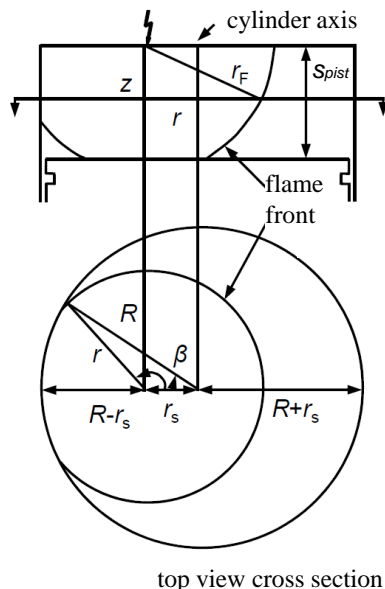
Figure 5.3: Flame surface modeling according for simplified combustion chambers, cf. [8, 68].

For every time step, there can be iterated the entrainment surface for that fixed geometry (cylinder bore, actual chamber height) with

$$A_e = f(r_F, s_{pist}, |\vec{r}_s|) \tag{5.9}$$

as function of the actual sphere radius r_F, piston position s_{pist} and the initialized and constant flame center r_s. (This is performed in contrast to static tabulated values, which are not able to cover a wide range of ignition timings and the yielding different flame-wall-interaction.) Discretized sphere partitions are used to sum up the overall surface (cumulation of truncated cones). As long as the flame front doesn't interact with walls (cylinder head, cylinder liner and/or top piston areas), this iteration is trivial. The entrained volume and surface can then be analytically related in an explicit way. When wall contact occurs, the interacting parts of the flame are subtracted via geometrical operations from the effective surface – the entrainment gets slower. Detailed descriptions of the modeling for A_e can be found in the literature [8, 30, 65, 68].

At this point, it shall be mentioned that the initialization of the flame is of great

importance for the burn out phase. Grill [30] proposed an eccentrically shifted center of the sphere away from the cylinder's vertical axis. Figure 5.4 (left) shows the effect of flame eccentricity *exc* on the surface development. Without eccentricity ($exc = 0$),
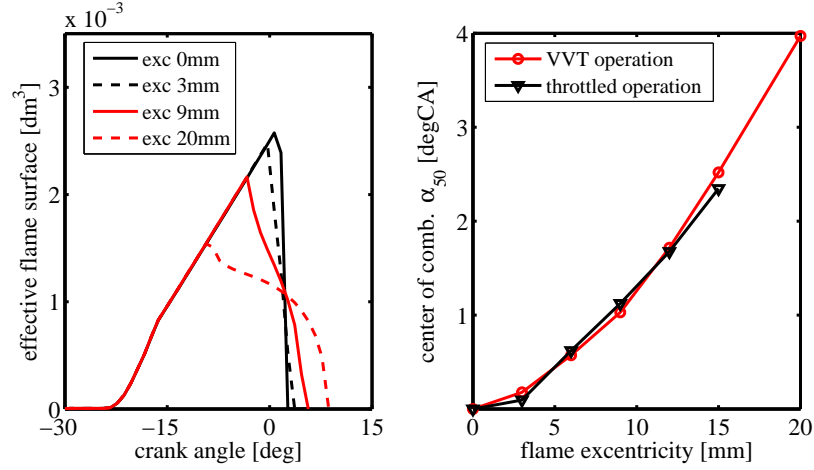
Figure 5.4: Modeled impact of the initialized flame eccentricity on entrainment surface development (left) and on the crank angle of 50% mass burned α_{50} (CA50, right) at 2000RPM, *bmep* 2bar for the BMW N20B20 engine, cf. appendix A and C.2. A variation of the sphere center causes the flame to virtually experience another turbulent propagation.

at a certain point the flame instantly reaches all liner walls at the same time – the flame surfaces collapses and produces inconvenient gradients in the mass burn rates. The nearer to the wall the flame is initialized with $abs(exc)$ rising, the smoother is the reduction of A_e at the end of entrainment. But the surface peak value also decreases due to an earlier liner interaction. Additionally the beginning of entrainment at -15degCA shows an inflection point in the surface function which is caused by the very first wall contact of the flame with the cylinder head.

Figure 5.4 (right) observes the eccentricity impact on cumulated burn rates for the *BMW N20B20* engine at 2000RPM and 2bar break mean effective pressure, compare appendix A and C.2. For both, unthrottled VVT and throttled operation, the variation of the flame center is able to shift the angle where 50% of the unburned mass is converted. This is especially important, when this parameter is used for calibration purposes of the overall entrainment model. Though, the comparably low sensitivity on *exc* may serve for a fine-tuning only.

All in all, it has to be kept in mind, that the flame center initialization doesn't correlate with the real engine's sparking location. Quite the contrary, eccentricity serves as

smoothing option for burn rate prediction.

5.3 Flame expansion effects in the entrainment model.

It exists a significant amount of literature using the entrainment approach for the simulation of premixed combustion in SI engines. A careful study reveals a problem that is occurring for all applications: in comparison with measured data, the model *equation for mass consumption* $\dot{m} = \rho_u \cdot s_T \cdot A_e$ *is too slow.* This formulation covers the physical background of combustion, where the mean entrainment surface burns with a turbulent propagation speed into the unburned mixture. Nevertheless, the pressure trace analysis shows a faster combustion in reality.

Thus, different authors cope in various ways with this problem. Grill [30] uses calibration parameters of the overall entrainment model to accelerate the combustion and to adjust it to the aimed behavior. Therefore, all factors differ from unity later. In contrast, Nefischer [68] chooses a formulation for s_T that estimates the turbulence interaction higher than any other and shows that herefore s_T scales linearly with Damkoehler's number $Da = (s_L \cdot l_t)/(v' \cdot l_F)$ in a log-log plot, which seems alright for the regime of corrugated flamelets. Auer [3] amplifies the entrainment equation with an *expansion factor*, considering the density ratio between burned and unburned zone. The mentioned method is widely discussed and shall be used for this section.

Often, optical experiments of a propagating flame are used to determine burning velocities. Therefore, it is known that not only fuel consumption itself leads to flame kernel growth. There exists a temperature step at the flame front establishing different densities in the unburned and burned mixtures. Thus, a relation for flame kernel growth can be expressed as

$$\frac{d}{dt}r = \frac{\rho_u}{\rho_b} \cdot s_T \tag{5.10}$$

which consequently leads to an increase of the effective surface A_e. The idea behind that approach equals that of an "expanding balloon". The balloon with hot gas on the inside expands homogeneously along the radial direction into the surrounding cold gas. Hence, the environmental volume is compressed which results in a rising cold gas density. This expansion is driven by temperature differences.

When adapting the entrainment approach with expansion factor Ex, one aims to accelerate the process. If this is omitted, the surface even collapses before all cylinder mass could be entrained which results in an incomplete combustion (it can only be burned what was entrained previously). The inclusion of Ex into equation 5.4 couples flame expansion, surface increase and unburned mass consumption for the entrainment process. Therefore, the unburned mixture can burn completely at sufficient rates, which is relevant for *imep* prediction (compare section 5.4). Usage of entrainment expansion contains a major statement: the propagating *entrainment ring interface is permeable.*
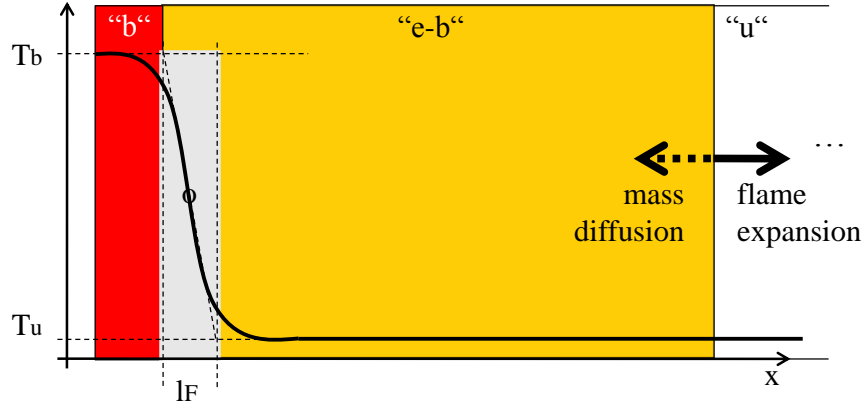
Figure 5.5: Planar projection sketch of a premixed flame with the zonal positioning of the entrainment approach. The laminar flame brush thickness l_F is determined, considering the flame's temperature profile, following Peters [74]. Assuming $l_{e-b} >> l_F$ and homogeneous density yields that $T_{e-b} \approx T_u$.

This means, that expansion of the entrained zone allows diffusion and convection of fresh mixture "u" into the ring zone "e-b", compare figures 5.1 and 5.5. Moreover, it makes sense to adapt the used Ex factor for the entrainment approach as following: as the whole entrained zone is expected to grow, the measure for expansion should be the density ρ_e. (Considering only ρ_b for the burned zone would make a significant difference for the starting combustion, when there is little mass burned but a wide volume already entrained and would therefore neglect the ring zone temperature influence.) Following the sketch in figure 5.5 with a crude estimation of the flame thickness and ring zone, one can state for the ring temperature that $T_{e-b} \approx T_u$. For the entrained density, it yields

$$\rho_e = \frac{p}{R \cdot T_e}. \tag{5.11}$$

The averaged temperature $T_e = \overline{T_e}$ is derived from the simplified idea of perfect mixing between burned and unburned but entrained components in the whole entrainment zone, so that

$$c_p \cdot m_e \cdot T_e = c_p \cdot m_b \cdot T_b + c_p \cdot m_{e-b} \cdot T_{e-b}. \tag{5.12}$$

When assuming that the heat capacity $c_p(T)$ stays constant for all 3 components and temperatures, the entrained temperature as mass averaged value can be rewritten as

$$T_e = \frac{T_b \cdot m_b + T_{e-b} \cdot m_{e-b}}{m_e} = \frac{T_b \cdot m_b + T_u \cdot (m_e - m_b)}{m_e}. \tag{5.13}$$

114

Resulting, the expansion factor defines

$$Ex = \frac{\rho_u/\rho_e}{(\rho_u/\rho_e - 1) \cdot m_e/m_{cyl} + 1} \tag{5.14}$$

whereas this formulation accounts for the declining effect of flame expansion at the end of combustion (compare figure 5.2).

5.4 Analysis of combustion ending.

It is necessary to take a look at the final stages of combustion α_{90}, because measured pressure trace analysis often shows a long burn out phase especially at part load engine operation. This seems rather unrealistic and has its origin in a bad signal-to-noise ratio for the pressure transducer in the later expansion stroke, which leads to late "pseudo heat releases". Thus, the measurements cannot be accurately interpreted in that stroke, but nevertheless the the burn-out phase is of special importance. Figure 5.6 (top) shows an artificial variation of the angle α_{90} (90% burned mass fraction) in the cumulative heat release curve. Therefore, a GT Power simulation at the *BMW N20B20* engine serves the variation for several load points, cf. similar parameters from figure 4.2 (c). The basis burning rates (non-predictive for these results) originated from a pressure trace analysis. For the variation, the starting combustion was held constant (ignition angle, α_5, α_{50}) to observe the isolated impact of the end of combustion, while α_{90} shifts in both directions. It can be stated, that even for a comparably high deviation of α_{90} the indicated mean effective pressure *imep* shows little sensitivity, as long as the heat release quality near ignition top dead center is not influenced.

In figure 5.6 (bottom) the degree of burned fuel for the process is varied with a GT Power simulation at the *BMW N20B20* engine. While the beginning heat release is maintained, after η_c% of burned fresh mixture, the rest of the original burn rate curve is cut at the corresponding angle α_{η_c}. With this variation, it can be stated that

$$-\frac{\Delta imep}{imep_{max}} \leq (100\% - \eta_c).$$

Hence, the degree of mass burnout is to predict very accurately.

In summary, it is not as important for *imep* prediction where the combustion ending lies as to know to what extent the flame consumes the fresh mixture. This must be considered for a modeling of *quenching distances* at the cold wall (very important for engine operation with high heat loss rates). Therefore, Peters as well as Turns use a crude estimate $\delta_{quen} \approx 5..6 \cdot l_F$ correlating with laminar flame thickness [74, 107].
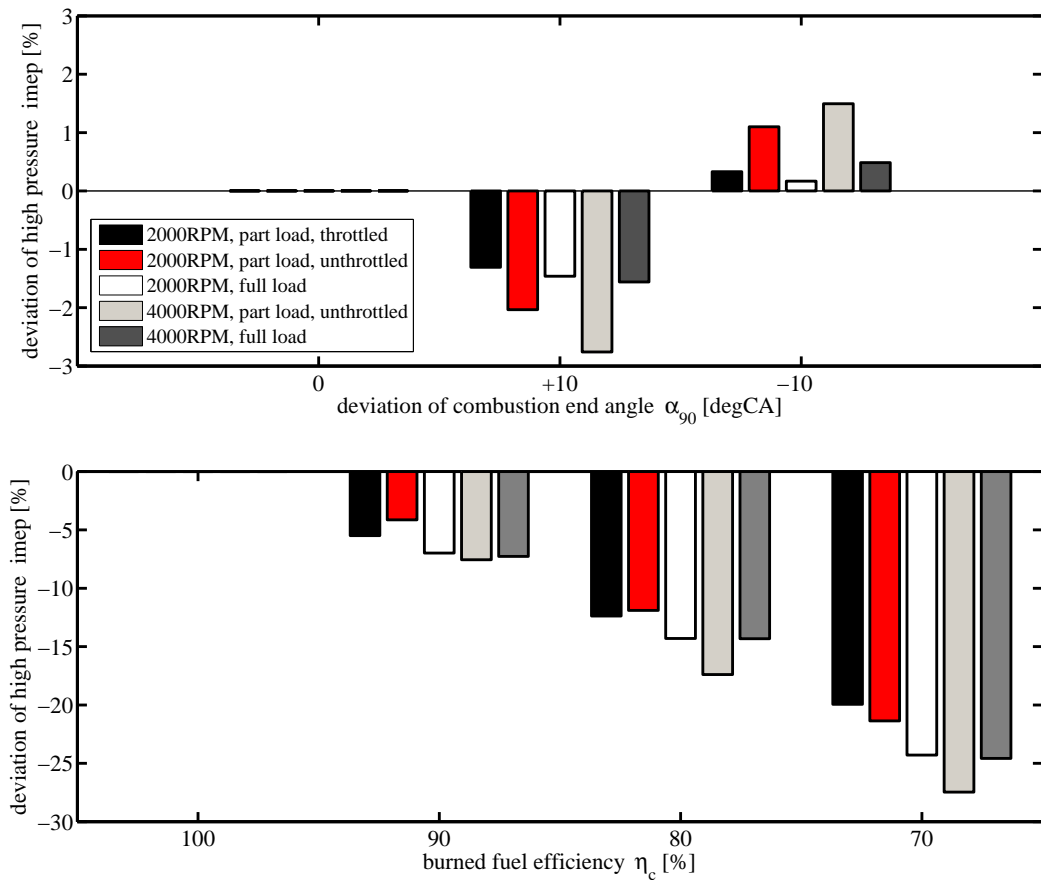
Figure 5.6: Simulated variation of combustion end angle α_{90} (top) and combustion efficiency η_c (bottom) regarding the accuracy of high pressure combustion *imep*. Combustion ending angles show to be less important than to predict to what extent the total fuel mass was consumed.

5.5 Classification of flame regimes.

The classification of regimes helps to gain understanding for the interaction between turbulent and chemical processes for turbulent flame propagation. Marking the stages of SI engine combustion can therefore be performed in the Peters-Borghi diagram [54, 55, 74]. In this log-log illustration, current velocity scales v'/s_L are plotted versus length scales l_T/l_F. The introduction of several non-dimensional numbers allows finding the different regimes that a flame can be represented or attributed to:

When assuming a Schmidt number of unity

$$Sc = \frac{\nu}{D} = 1, \tag{5.15}$$

the turbulent flow can then be characterized with the Reynolds number

$$Re = \frac{v' \cdot l_t}{s_L \cdot l_F}. \tag{5.16}$$

For $Re < 1$ laminar flamelets can be assumed in a triangular area in the Peters-Borghi diagram and for $Re > 1$ turbulent combustion takes part. The Damkoehler number Da defines the ratio between turbulent time scales and chemical reaction time scales (cf. equation 3.1) and thus tells if the flame propagation is mixing controlled or reaction controlled. In case $Da = 1$, the bisecting line can be found in the Peters-Borghi diagram. Typical SI engine combustions operate in regimes with $Da > 1$, hence controlled by turbulence and mixing. The ratio between chemical time scales and the Kolmogorov turn over time t_η on Kolmogorov length scales l_η for the smallest eddies, known as Karlovitz number, is formed as

$$Ka = \frac{\tau_{chem}}{\tau_\eta} = \frac{l_F^2}{l_\eta^2}. \tag{5.17}$$

$Ka > 1$ shows that the smallest eddies are penetrating into the preheat zone. But they can only enter the reaction zone, if they are smaller than the laminar flame thickness, hence $l_\eta < l_F$. The function $Ka = 1$ has a slope of 1/3 in the Peters-Borghi diagram. Figures 5.8-5.11 show that homogeneous and stochiometric turbulent combustion in SI engine configurations takes place in two main regimes: *corrugated flamelets* and *thin reaction zones*, compare also figure 5.7.

5.5.1 SI engine combustion regimes.

Corrugated flamelets. Corrugated flames are flamelets, where the reaction zone is a very thin layer. They are characterized by weak turbulence and fast chemistry, which in fact allows an interaction between laminar flame propagation and turbulent scales [73]. In this regime, Reynolds number and Karlovitz number behave like $Re > 1$, $Ka < 1$ and the velocity fluctuation is greater than laminar burning velocities. Figure 5.7 (left) shows, that turbulent eddies turn at a velocity v' of at least laminar flame speed s_L. Therefore the biggest eddies are not just run over by the fast flame, but can clearly deform its front (corrugation). The increased turbulent burning velocity is caused by significant amplification of the turbulent flame surface. Another characteristic is an unchanged inner flame structure. Because the smallest eddy size (Kolmogorov scale) is still too big to penetrate the inner flame, all turbulence can only work on the flame's
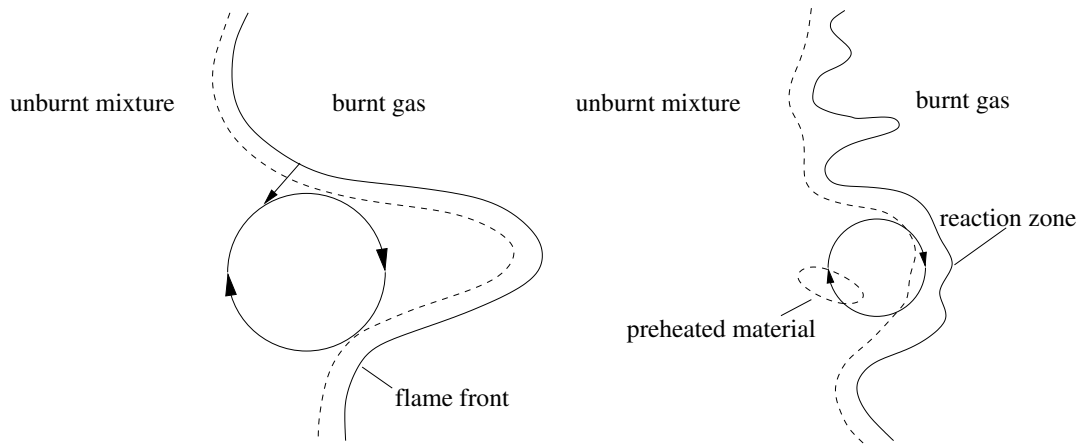
Figure 5.7: Turbulence-flame interaction for the regimes of *corrugated flamelets* (left) and *thin reaction zones* (right) [73].

outer appearance.

Thin reaction zones. In this regime the smallest eddies can enter the inner flame structure. They penetrate into the broader preheat zone and increase mixing processes by transfer of preheated material into the fresh gas zone, compare figure 5.7 (right) [73]. The reasons for this enhanced interaction lie in a comparably smaller eddy size and higher degrees of turbulence. The regime has its name from the fact that turbulent structures cannot yet enter the thin reaction zones of the flame, hence $Re > 1$, $Ka > 1$ but still $l_\eta > l_F$. Hence, the location of chemical conversion stays quasi-steady. Turbulent burning velocity is determined by reactive diffusion and normal convection of the flame structure [74].

5.5.2 Trajectories in the Peters-Borghi regime diagram.

In his investigations, Linse [53] finds, that certain changes in the throttled operation state of an in-line 6-cylinder SI engine cause the change of combustion boundary conditions. This can be tracked in the regime diagram.
The *horizontal shift* along increasing values of the axis l_t/l_F in the Peters-Borghi regime diagram, cf. especially figure 5.9 (right), can have two different reasons:

1. especially a decrease of laminar flame thickness (thermodynamics) and/or

2. an increase of mean eddy sizes (turbulence).

This translation to the right end weakens the ability of eddies to penetrate into the inner flame structure and thicken it. Moreover, this shift is normally caused by engine

load changes.

The *vertical shift* along increasing values of the axis v'/s_L in the Peters-Borghi regime diagram, cf. especially figure 5.9 (left), also has two reasons:

1. an increase of velocity fluctuations (turbulence) and/or

2. a slower laminar flame propagation (thermodynamics).

With a translation to the top end in the diagram, fast turbulent structures highly affect the macroscopic outer structure of a slow laminar flame front. Turbulence changes (e.g. by engine speed variation) are major contributors to this vertical shift.

The mentioned mechanisms work independently from each other but may also be superimposed, which will be shown in the following variations.

5.5.3 Classification of multiple operation states.

In this section, different engine operation states for the *BMW N20B20* aggregate are classified in the *Peters-Borghi regime diagram* for premixed combustion with the help of Peters' formulation for turbulent burning velocities [73, 74]. Therefore, the variations were simulated with the introduced combustion model environment in a GT Power coupling (including thermodynamic verifications, the turbulence model, the ignition delay model and the *validated entrainment model* itself, cf. sections 2.3.2, 3, 4 and 5.6).

Figure 5.8 shows the result of different ignition angles in the Peters-Borghi regimes. Therefore, the part load standard VVT operation at 2000RPM and *bmep* 2bar (appended in section C.2) was varied with an early ignition timing at 40degCA before and a late timing at 10degCA after ITDC. For an early/regular ignition, a ring shaped curve [53] passes through the regime border with Karlovitz number $Ka = 1$. The late ignition shifts the curve to the left because cylinder pressure lessens, hence the laminar flame can broaden. A tiny vertical translation is caused by smaller laminar burning velocities. Additionally, the later the ignition occurs, the more the resulting curve loses its ring shape, caused by the profile of laminar flame thickness versus crank angle.

Figure 5.9 shows the flame classification for varying engine speed (left) and engine load (right) at maximum intake valve lift (throttled operation). All shown simulations were carried out with *tumble 1* operation as basis load point, cf. table 3.2. Linse [53] could already show that engine speed affects turbulent states (pure vertical shift) and engine load affects the thermodynamic states (pure horizontal shift) of the flame. This statement only accounts for an operation at maximal valve lift and constant valve timing. Therefore, the load is defined via the intake manifold pressure (500, 1000, 2000mbar in this case).

Figure 5.10 plots an engine speed variation for low intake valve lift (unthrottled operation), compare appendix C.2 with 2000RPM and *bmep* 2bar (VVT) as reference
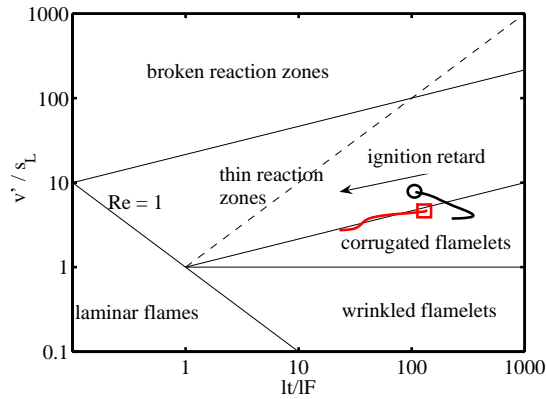
Figure 5.8: Peters-Borghi classification for a variation of ignition timing at 2000RPM, part load. The curves are plotted from ignition (symbol) to combustion ending. Circular marked ignition takes place at -40degCA, square marked ignition occurs at 10deg after ITDC.
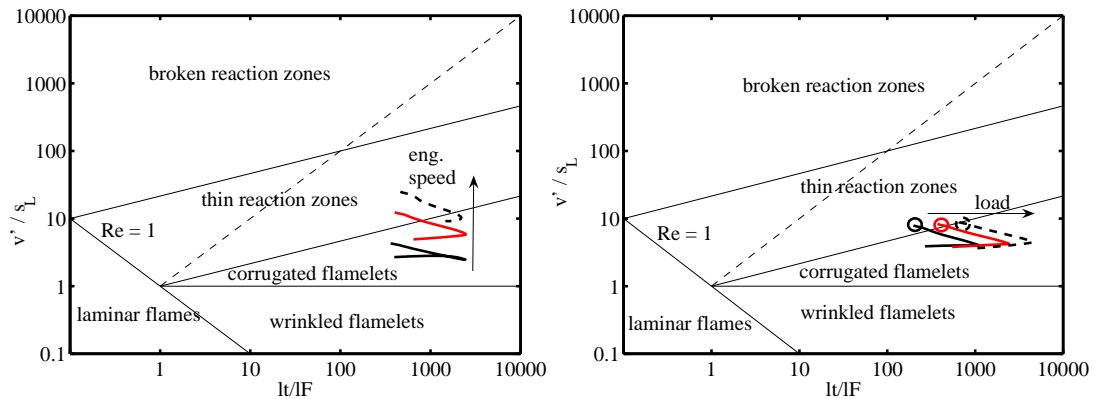
Figure 5.9: Peters-Borghi classification for a variation of engine speed (left) and engine load (right) at maximum intake valve lift, compare Linse [53]. Engine speed (1000, 3000, 6000RPM) shows impact on turbulent intensity, load states (intake pressure: throttled, ambient, turbocharged) affect laminar flame thickness.

operation. It can be seen, that this not only affects turbulence but also the thermodynamic state. Throttling losses over the intake become frequent at high engine speeds which results in less fresh cylinder charge (pressure loss over the intake valve and gap
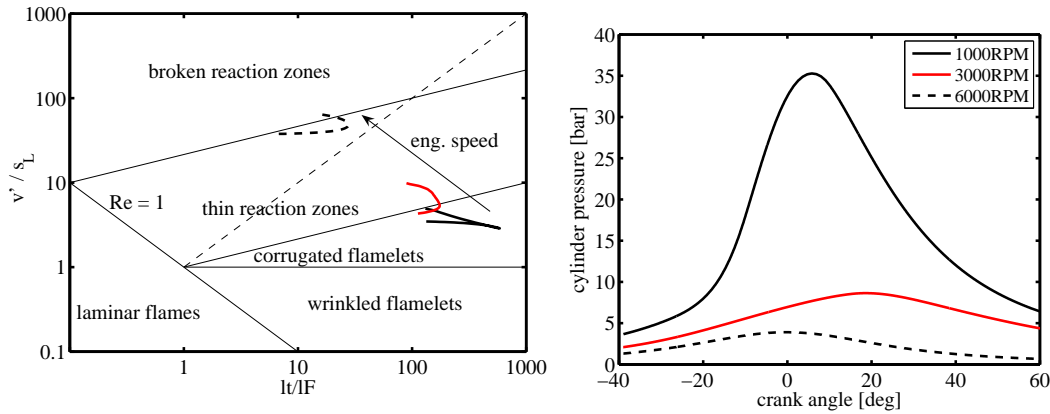
Figure 5.10: Peters-Borghi classification for a variation of engine speed at low intake valve lift and ambient intake pressure (left). A higher engine speed not only affects turbulence but also the trapped air masses in the cylinder. Thus, the impressed engine speed also shifts the engine load and cylinder pressure (right).

velocity relate like $p_L \propto (\vec{v}_{IV})^2 \propto 1/L_{IV}{}^2$). The cylinder pressure decreases and the flame structure can broaden. Thus, a variation of engine speed at low intake valve lift also leads to a shift along the load axis. For the simulation of an engine speed at 6000RPM, the combustion takes place very closely to the regime borders between *thin reaction zones* and *broken reaction zones*, where the applicability of the turbulent burning velocity formulation lacks accuracy. Nevertheless a 6000RPM load point with very low valve lift are not essential for normal engine driving cycles but shall illustrate the general behavior of the combustion model in this manner.

Figure 5.11 plots the variation of intake valve lift for an unthrottled operation at 2000RPM. The simulations were carried out with *swirl 1* operation as basis load point, cf. table 3.2. For the lift ranging from 1mm to 4mm, this results in a change of thermodynamics (load control via valve lift) and turbulence (different types of charge motion induced). The quality of resulting load changes is comparable to figure 5.10 and the behavior of swirl and tumble motion for this lift variation can be seen in figure 3.17 (left). At 4mm no more fresh charge enters the cylinder with rising valve lift. Thus, thermodynamics then stay unchanged. From that point, only turbulent states vary, which can be seen in a vertical shift in the regime diagram.
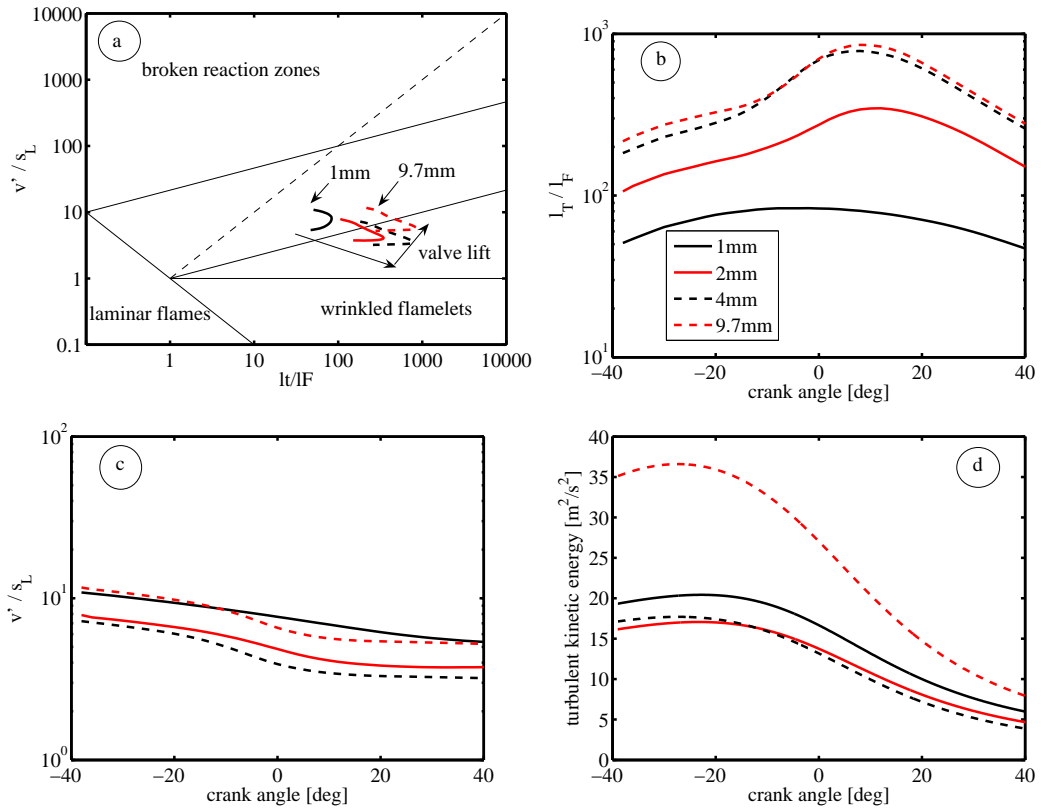
Figure 5.11: Peters-Borghi classification for a variation of intake valve lift at 2000RPM and ambient intake pressure (a). For the range from 1mm to 4mm the valve lift controls the amount of trapped fresh charge and changes the turbulent states due to transition from swirl to weak tumbling motion. This produces a combined shift of thermodynamics and turbulence in the regime diagram. Between 4mm and maximum valve lift the load stabilizes (b) and only turbulence changes (c,d).

5.6 Model calibration and validation with pressure trace analysis.

The proposed entrainment model is already capable of predicting the general behavior of ignition delay α_{idel} and CA50 angle α_{50} quite well at all engine operations. It is very important to note at this point, that the *untuned model* can already be used for *early stages of engine development*, when reliable measurements are not yet available or real hardware is still too expensive for wide employment. This is not only versatile for virtual engine calibration but also for model based control issues and data mining for new concepts.

The mentioned entrainment results can be further improved with the help of an auto-calibration routine. The aimed high degree of automation thereby reduces manual sources of error.

So at first, some points of interest within the engine map have to be chosen for calibration. Thereby one has to act with caution when spreading all important influences on combustion (residual gas, load, turbulence, air-fuel ratio). Afterwards an innovative work flow for the *automated model calibration* process contains the following steps:

1. producing a new set of calibration parameters (optimizer)

2. calculating the engine cycle including combustion (engine simulation)

3. evaluating the error norm based on targeted quantities (post processor)

4. comparing error values with accuracy corridor (pre-optimizer)

There is performed a software "hand shake" between all mentioned steps and the work flow is repeatedly performed until the cumulated error values fall below accepted limits. It is advised to run all time consuming calibration steps on distributed infrastructure, which can immensely fasten execution (convergence in one day for the whole engine map, containing around 250 simulation cases).

The quantities for error evaluation which are to be reproduced, were chosen to be flame development angle α_5 and CA50 angle α_{50} (compare section 4), because they are of great importance both for *imep* and exhaust gas temperature prediction. Free parameters for entrainment equations are

- C_{burn}, scaling time constant τ in equation 5.8 and

- C_{egr}, scaling residual impacts of x_{rg} on laminar burning velocity s_L according to Metghalchi's formulation [61]:

$$s_L = s_{L_0} \cdot \left(\frac{T_{cyl}}{T_0}\right)^\alpha \cdot \left(\frac{p_{cyl}}{p_0}\right)^\beta \cdot \left(1 - 2.06 \cdot x_{rg}{}^{C_{egr}}\right). \qquad (5.18)$$

In this relation the quantities $\{s_{L_0}, T_0, p_0\}$ describe a state of reference laminar burning velocity, reference temperature and pressure. The empirical exponents α and β influence sensitivity on state variables.

In case of an alternative application of Ewald's formulation for s_L [20], the fine-tuning works in the term of the reactive mass fraction

$$Y_{react} \propto (1 - x_{rg})^{C_{egr} \cdot 0.8507} \quad .$$ (5.19)

At last it is to be noted, that the calibration factors for optimization lie close to unity for global optima, which proves that the underlying physics are correctly captured in the models.

Results of a converged model calibration can be found in figure 5.12 for the *BMW N20B20* engine and some standard data point from appendix C. The validation of cumulative burn rates are plotted for different operation states. It becomes clear that
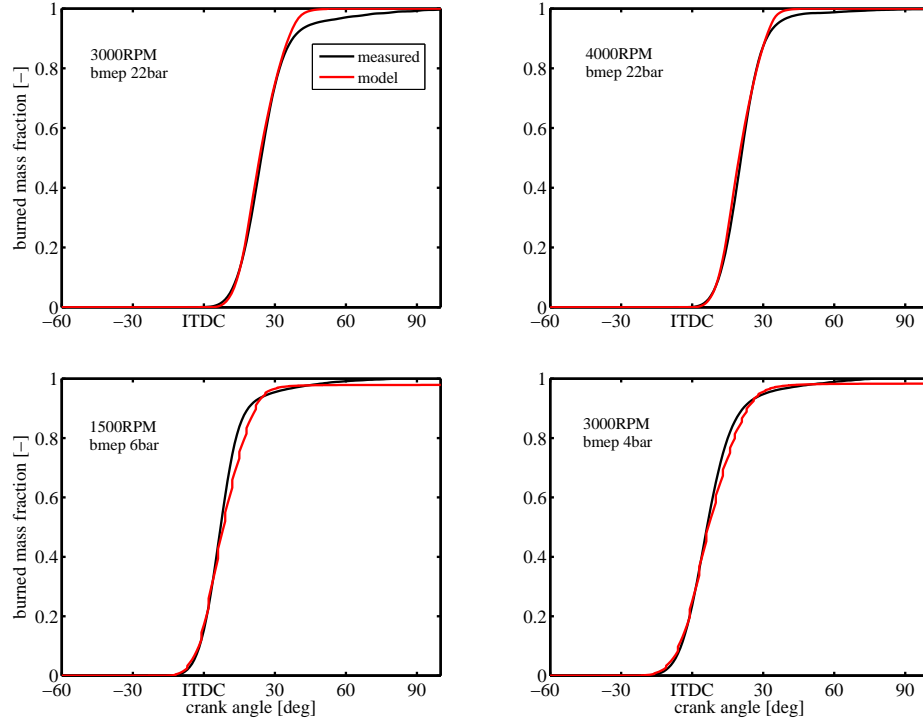
Figure 5.12: Validation results for the auto-calibrated entrainment combustion model. Turbulence, load and residuals vary widely for the four operations.

especially the beginning combustion is met extremely well. The simulated burn out

124

duration deviates from measurements, which origins from obtained pressure data but doesn't impact on *imep* quality, compare section 5.4.

Another interesting impact are residual fractions, compare figure 5.13 for a part load operation at 2000RPM/*bmep* 2bar (VVT) with late exhaust valve closure for an enhanced flue gas mass ($x_{rg} = 25\%$). As common formulations for laminar burning
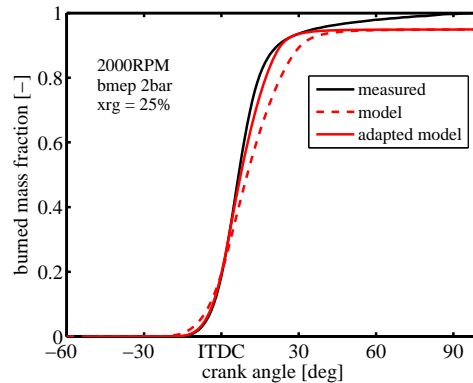
Figure 5.13: Effect of calibration factor C_{egr}. Residual fractions are enhanced (early ignitions required). Slow laminar burning velocity s_L highly affects the whole combustion behavior.

velocities overestimate the influence of high diluent fractions, the flame gets so slow that it is quenched by the piston before it can consume all fresh mixture. A tuned factor C_{egr} can accelerate the combustion and reproduce the measured data, but a better s_L formulation for higher residual fractions could furthermore improve the combustion efficiency (instead of stopping at $\eta_c = 96\%$).

Proof of concept. For the calibrated combustion model, figure 5.14 shows the quality of the overall model complex. All aforementioned model parts (thermodynamics, turbulence, ignition delay, entrainment) have been included in these results and work together to produce a cumulated heat release. Figure 5.14 shows the deviation between the model results and a measured engine map (model - measured value) for the crank angle of 5% mass burned α_5 (left) and the crank angle of 50% mass burned CA50 (right). Thus, in case the deviation values are greater than 0, the model predicts a too slow combustion and vice versa.

The combustion speed is underestimated in figure 5.14 for very low engine loads. These results show the same quality that could be found in the thermodynamic model validation, compare figure 2.11 (left), since the air charge determination has problems
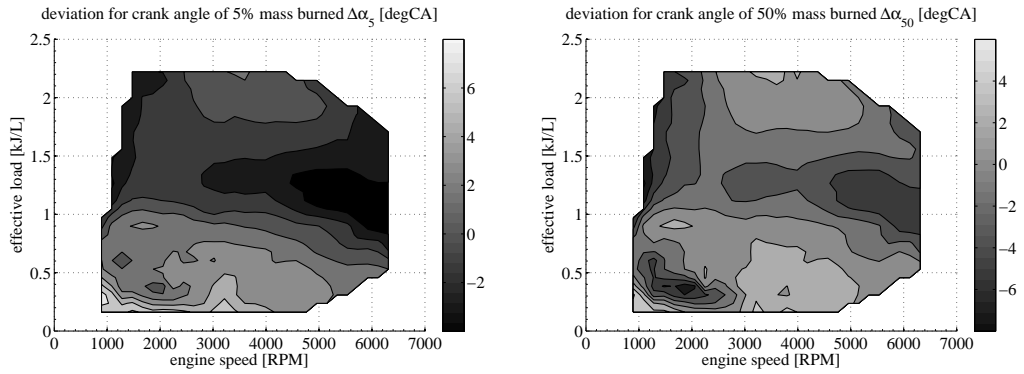
Figure 5.14: Proof of concept for the combustion model complex. Deviations between predicted and measured cumulative heat releases are shown for the crank angle of 5% mass burned α_{50} (left) and 50% mass burned CA50 (right).

coping with very small intake valve lifts and residual gas back flow phenomena. Thus, a good prediction of air masses and the thermodynamic state is fundamental to a good prediction of the combustion state.

The combustion model predicts a too high burn rate for high valve overlaps in part load and full load both at low engine speeds. This effect can be traced back to a lack of residual fraction in the simulated cylinder, compared to the measurement. Moreover the "scavenging of turbulence" fractions directly from the intake to the exhaust is neglected in the derived turbulence model and might contribute to deviations in that manner.

For high engine speed and part load, the combustion model predicts a too fast heat release in figure 5.14. In these operation states, the ignition timing is very early because the time spans for combustion shorten significantly. The derived turbulence model overestimates the turbulence states for ignition timings early before ITDC, compare *tumble 2* turbulence in figure 3.13 (right), which accelerates the turbulent burning velocity. This effect becomes more evident in the deviation of CA50 angles, since in the phase of ignition delay the turbulence impact on the heat release rate is smaller (transition from laminar to turbulent flame).

Considering that the measured values for figure 5.14 derived from a fast heat release analysis, the results of the overall combustion model are acceptable within the whole engine map. With this proof of concept, an application in virtual engine calibration is promoted.

126

5.7 Engine map exploration.

After calibration and validation of the entrainment model, the fast computation of whole engine maps on a cluster of processors allows taking a wider look at interesting quantities.
Results such as shown in figure 5.15 can be used in mechanical design of engine parts. Here, the maximum cylinder pressure is plotted within a truncated map (left). Maximum
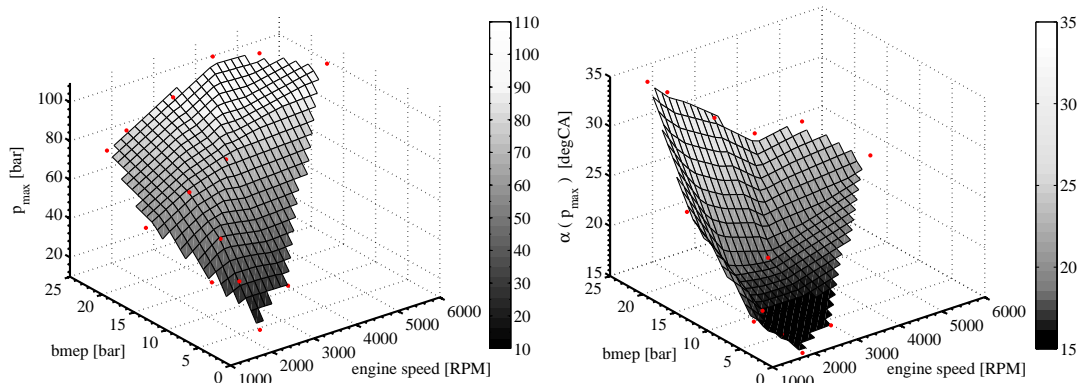
Figure 5.15: Engine map exploration for mechanical design. Maximum cylinder pressure (left) and its occurrence after ITDC (right) are plotted for typical engine operations.

values range around 100bar at high engine speed and high loads and are important for cylinder head, piston and piston ring design. The right plot in figure 5.15 shows the occurrence of maximal pressure values after ITDC. The higher the load is, the later occurs the maximum pressure because a higher fuel mass must burn at similar engine speeds. The effect of a knock preventing ignition (ignition angles served as model input) at full load and small engine speeds can be seen for considerably late maximal pressures at 35degCA after ITDC. The occurrence of maximal pressures can be used for dimensioning crank train related assemblies.
Figure 5.16 plots pressure excitations in the exhaust system. Therefore, the pressure peaks after the turbine were plotted for each operation. Those amplitudes are responsible for acoustic behavior and vibrations. Hence, results can be used for exhaust system design and early statements on noise-vibration-harshness issues (NVH) for new engine concepts. The shown results do not only correlate with engine load and speed (cylinder pressure, outlet frequency) but also with exhaust cam timing and waste gate position.
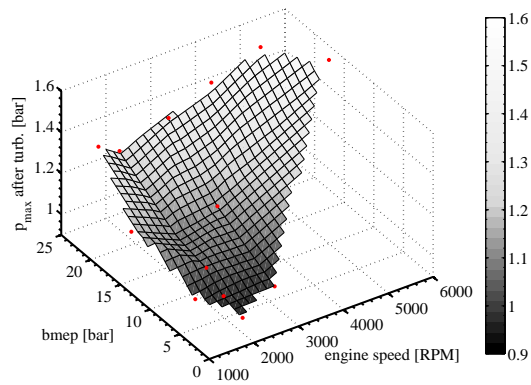
Figure 5.16: Engine map exploration for acoustic related statements. Pressure amplitudes after turbine are inducing potential for noise and vibrations in the exhaust system.

6 Virtual engine calibration with a quasi-dimensional combustion model.

Preface for virtual engine calibration. Parts of the discussed results originate from the master thesis of Knoll [45], which I supervised during my time as doctoral candidate. All simulations in this section were carried out for the *BMW N20B20* engine configuration. Chapter excerpts were published previously [27].

6.1 ECU engine torque model.

In torque based ECU concepts, many functions calculate their quantities based on the engine's output. The engine torque model therefore provides all necessary information about "sensed" torque and links the central physical output of the engine with the actuators. One can divide two pathways for its calculation:

- *forward* – the ECU sends an effective torque demand for the driving situation and the engine torque model calculates the triggering of the actuators to provide this output.

- *backward* – the engine torque model produces a measure for effective torque at the clutch from supplied actuator conditions and measurements.

The directions of calculation are related to the physical signal flow of engine torque development. In modern power train systems with electronic accelerator, the overall torque demand can be modulated independently from the driver's wishes. Hence, for the control of actuators, the mentioned forward pathway of the engine torque structure gets important. It is interesting to note, that the inversion of the forward calculation can virtually sense torque and therefore save the expenses for real sensor hardware.

For actuation of demanded torque, the distinction of fast and slow possibilities is appropriate. The *fast actuation* synchronously works with each combustion cycle and is provided via variable ignition timing and injection. For stoichiometric concepts, the air-fuel ratio is rather constant, which leaves ignition timing as free parameter. The *slow actuation* influences the air charge, which needs several engine cycles to reach steady state again. (For example, the throttle flap in an SI engine can be used to control the entering air masses into the cylinder. Depending on the gas volumes between throttle flap and intake valves, there is introduced a certain reaction time after an actuation of the throttle flap until the system can be run in a new steady state with then lower

or higher load.) For dynamic reasons, if the torque demand is a step function, the engine is at first actuated via the fast path, inducing a quick change of combustion efficiency. Afterwards, to reach the optimum operation again the slow path is reset to the according air charge.

6.1.1 Description of the functional calculation.

The main task of the torque model is the determination of the effective engine output. Therefore, the reduction of combustion mean effective pressure (mep) follows the law

$$bmep = imep_{comb} - pmep - fmep. \tag{6.1}$$

With regards to thermodynamics, the energy release in the cylinder produces a pressure rise at the compression and expansion stroke, which concludes a gross indicated pressure $imep_{comb}$. To keep the engine cycle going afterwards, the consecutive gas change at the exhaust and intake requires pumping energy $pmep$. The mechanical losses are subtracted in the following per friction mean effective pressure $fmep$. At this point, only effectively usable energy $bmep$ is still present at the clutch, compare equation 6.1. This brake mean effective pressure is an equivalent to brake torque.

A combustion model opens up the opportunity to learn more about the gross indicated pressure and the indicated high pressure engine torque ($imep_{comb} \propto M_{ind}^{comb}$) because it can evaluate pressure rise due to heat release rates. Here, the indicated combustion efficiency ranges from zero to unity and may be defined for every engine operation state as

$$\eta_{ind}^{comb} = \frac{imep_{comb}}{imep_{comb}^{max}}, \tag{6.2}$$

with $imep_{comb}^{max}$ as optimum value for the corresponding engine parameters. Moreover an associated gas change analysis may evaluate pumping losses $pmep$ for different engine operations. Two thermodynamic samples for combustion related calibration data are plotted in figure 6.1.

Ignition curves. The correlations between indicated mean effective pressure and ignition timing are called "ignition curves". They are measured by stabilizing all actuators at a steady engine operation. Only the ignition angle is used as varying parameter, whereby the air charge stays constant. It turns out, that there is an optimum ignition timing, where the combustion produces the best possible pressure rise for this engine operation and the indicated output maximizes. Apart from that optimum timing, thermodynamic losses (wall heat transfer and exhaust enthalpy) rise. From this knowledge, there can be derived an indicated efficiency of operation which correlates the actual $imep$ with the one at optimum ignition timing for this engine operation. This is plotted in figure 6.1 (left). The later ignition angles are limited due to high exhaust gas temperatures
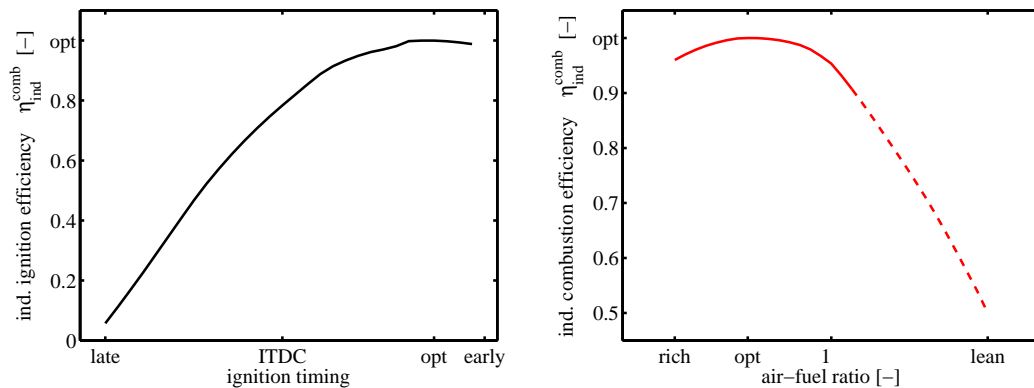
Figure 6.1: Schematic diagram for "ignition curves", showing the indicated efficiency versus different ignition timings (left). Schematic diagram for "air-fuel ratio curves", correlating indicated combustion efficiency to mixture richness (right). Stoichiometric engine concepts don't use the lean part of the correlation as in the dashed part.

and misfiring operation, harming the catalytic system at the real engine. The earlier ignition angles are bounded to knocking limits. For the ECU torque model the ignition curves are an important objective. Their requirements in accuracy and thus test bed resources are very high.

Air-fuel ratio curves. The mentioned indicated efficiency of operation also changes with the richness of mixture. Again all actuators are stabilized at a steady engine operation but now the amount of fuel injected is varied at constant trapped air mass and optimum ignition timing. The combustion efficiency can be recorded versus air-fuel ratio, compare figure 6.1 (right). Stoichiometric engine concepts move around fuel air ratios of unity; richer mixtures are burned when exhaust gas cooling is essential. For stoichiometric and rich mixtures the air-fuel ratio curves are rather flat and have their optimum slightly in the rich regime, which can be explained with higher laminar burning velocities. Here, indicated air-fuel efficiency values around 0.9+ and requires less calibration effort compared to the mentioned ignition curves.

Signal flow for torque estimation. Figure 6.2 shows how the ECU processes calibrated data for torque modeling. In this simplified flow chart, the "backward" path of torque calculation is described assuming stoichiometric mixture. At first, the general engine
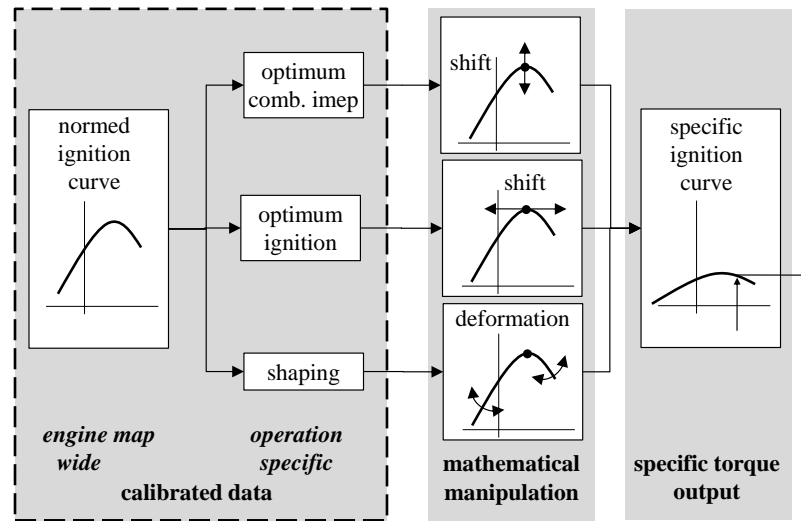
Figure 6.2: Simplified signal flow for the torque structure's determination of the indicated engine output $imep_{comb}$. The dashed context of the ECU function can be calibrated with a combustion model. (influences of a differing air-fuel ratio are neglected here.)

specific ignition curve (*normed* ignition curve) is applied. It represents the general shape of all ignition curves in the engine map without specific information about the special operation point. Afterwards, this general engine specific curve is manipulated, considering specific operation characteristics. These are namely the *optimum imep* output and the *optimum ignition timing*. The parabolic opening angle of the engine specific input is edited with a *shaping* factor which controls the mathematical slope for each specific operation point. Hence, with the help of operation specific data (depending especially on engine speed, air charge and engine temperature), the normed curve could be modeled as specific ignition curve. It now becomes clear, that all dashed contents in figure 6.2 need to be filled with data. Together, the specific ignition curve and the actual ignition angle form a measure for the indicated torque. This output can then be corrected for different air-fuel ratios, varying from stoichiometric mixture.

6.1.2 Requirements and conduction of simulation experiments.

The engine torque structure shows high potential for virtual calibration because measurement efforts are very high and repeatedly needed in engine development. Required accuracy ranges differ widely depending on the project's maturity. Moreover many

132

consecutive ECU functions need the engine torque structure's results even in early stages of engine development [48, 87]. Following equation 6.1, a combustion model may be able to calculate the indicated engine output $imep_{comb}$ for different engine operations. Thus, the dashed context in figure 6.2 is open to calibration. Moreover, the loss term for gas exchange $pmep$ could be described with an added on engine cycle simulation, which is a standard work flow to determine trapped air charge as well. In fact, it seems harder to determine the friction maps $fmep$ for the torque model, because these cannot be physically modeled for complex engine systems (variable high pressure pump, thermal management, engine stop automatic etc.) but have to be measured in advance. Hence, this is not objective in this work.

When acquiring data for engine torque calibration via 0D simulation, one has to keep in mind the rough boundary conditions connected to the measurement on real hardware test beds. The simulation is able to determine multi-cycle averaged values without the need for a robust air-fuel control, knock prevention or final injection strategy. This makes it more handy for early applications. Moreover, virtual determination of indicated engine torque is not subject to cyclic variations. For engine simulation one does not have to fear a system damage, thus there can be driven very late ignition timings which cause high exhaust gas temperatures and probably misfiring operation. For very early ignitions, at a test bed there would be expected knocking events which limit the operation range. This doesn't occur for simulation. Summarizing, the properties of 0D virtual torque calibration are

- *advantages*
  - $\oplus$ early model application possible due to little need for robust environmental controllers (air-fuel ratio, knock, etc.)
  - $\oplus$ simulation is partially freed from disturbing influences, since real world physics are not fully captured (e.g. cyclic variation phenomena and sensor hysteresis)
  - $\oplus$ operation boundaries for ignition timing can be expanded

- *future potentials, possible deviations*
  - $\ominus$ no trivial determination of real hardware ignition limits without additional modeling of knock and misfire
  - $\ominus$ not predicting the influence of different injection timings SOI (inhomogeneity of mixture)
  - $\ominus$ influences of different engine temperatures on combustion should be filed in advance as far as required

Simulation set-up. Similar to the real test bed process, one has to create a modular grid of measuring objectives capturing all important areas of the engine operation map.

Engine speed and reference volumetric efficiency therefore specify the simulation list. They serve as enquiry parameters for the engine actuator quantities, originating from previous basic calibration. (This means, that the calibration of optimum valve train parameters, best ignition timing and air charge control must be accomplished earlier.) After defining the steady state engine operation, the ignition timing is varied around its optimum value. Therefore an offset angle is applied along the earlier direction and another offset vector is applied to capture the curve tail for late ignitions, compare figure 6.1. At every different ignition stage, there are now recorded the steady state quantities of interest (*imep*, *pmep*, etc.). It has to be paid attention if the simulation met the target volumetric efficiencies, because their deviation directly involves incorrect stretching of produced two-dimensional calibration data.

All in all, main efforts were put into the calculation of around 365 ignition curves for the engine torque model within 3.5 days of parallel computing. This is even a time cut compared to dynamic experiments on the test bed, lasting around 1-2 weeks.

6.1.3 Calibrating the ECU torque model.

The introduced combustion simulation approach is capable to predict combustion *imep* even before model calibration. But accuracy can be boosted with few model constants, mentioned in the previous chapters. Figures 6.3 and 6.4 aim at a raw comparison between some original measured and original simulated ignition curves. (The post
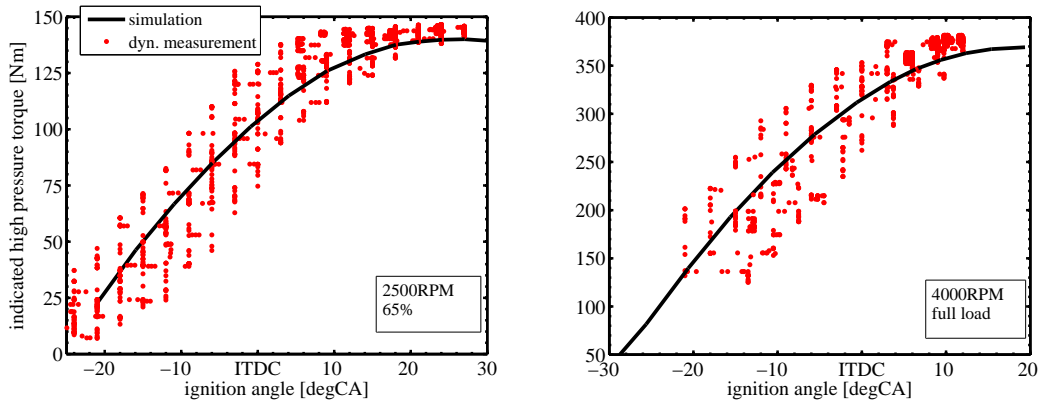

Figure 6.3: Ignition curve comparison between simulation and dynamic measurement. 2500RPM/ 65% volumetric efficiency is important for inner city parts of the NEDC (left). The limited operation range at 4000RPM/ full load can be expanded in the simulation (right).

processing of the obtained data blocks would happen in the next calibration step and

change the raw values by filtering and averaging. Therefore, the comparison uses original scatter data for the measurement itself.) Especially for driving cycles, it is relevant to reproduce the demanded engine torque precisely, because drivers constantly pass through those operation ranges. In figure 6.3, there is plotted the dynamicly measured raw scatter and the unprocessed simulated ignition curve for a relevant low speed/ low load point (left). Thereby the measured scatter is produced by dynamically setting ignition timings with continuous recording of pressure indication (indicated torque can be derived from indicated mean effective pressures). The test bed data is spreading widely due to cycle-to-cycle variations, short-term and mid-term sensor drift as well as measuring outliers. Hence, it can be understood, that the quality of engine calibration data is coupled with an intelligence in clustering and averaging the scatter. Here the simulated *imep* widely meets the averaged measurement spread. Especially in figure 6.3 (right), the advantage of expanded operation ranges for the simulation becomes clear – the engine output can be quantified without fear of knocking and critical exhaust temperatures.

In figure 6.4, a rich ignition curve is shown. Here, another important fact for the
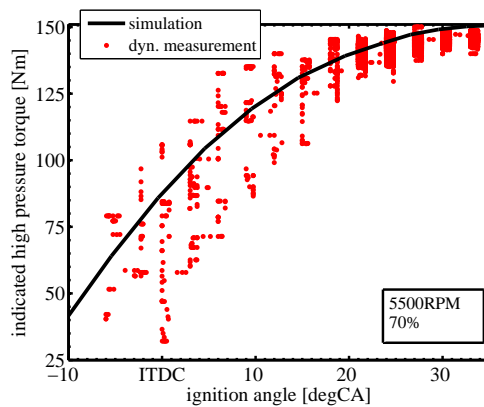
Figure 6.4: Ignition curve comparison between simulation and dynamic measurement at 5000RPM/ 70% volumetric efficiency. The operation is slightly rich for exhaust gas cooling and the test bed operation clearly produces misfiring for late ignition angles.

simulation data comes into mind: the simulation cannot capture misfire operation. Those points of the scatter would have to be filtered, because they falsify the mean value of indicated torque. Hence, simulation methods can even boost robustness of the ECU calibration because there is no need to refilter the data.

All in all, the introduced combustion model is reliable to produce data for serial production in the ECU torque model, which will be further investigated in the following plots.

Figure 6.5 shows the derived data for optimum indicated torque (left) and optimum ignition angle (right). (The actuations for valve timing, intake valve lift, boost pressure,
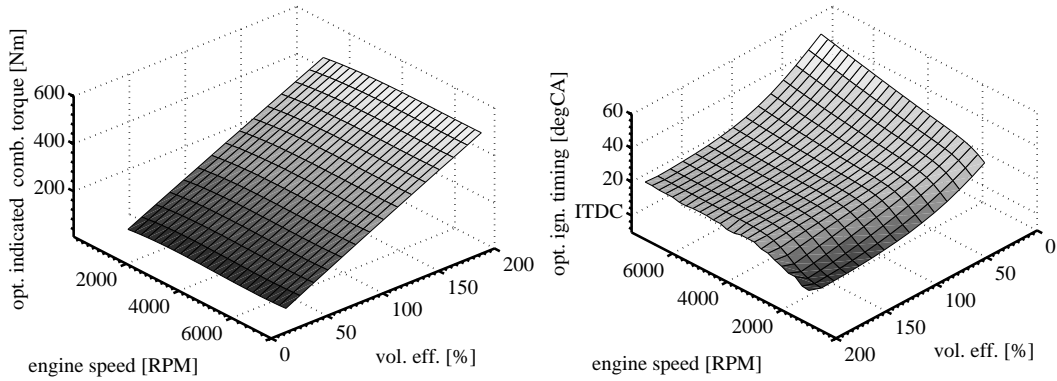
Figure 6.5: Derived data for ECU torque model calibration. Optimum indicated torque (left) and optimum ignition angles prior ITDC (right). The margins of the engine map were extrapolated for completeness.

throttle angle and fuel injection served as input for the simulations and they were derived from test bed calibration works.) The optimum indicated torque shows a trivial form within the engine map, because it only depends on the engine's load. Hence, with best possible ignition timing at stoichiometric mixture it writes $M_{ind}^{comb} \propto voleff$.

The map of optimum ignition angles is more complex in behavior, compare figure 6.5 (right). It shows that the needed spark advance rises in the direction of low loads, resulting from longer ignition delay spans. The nearer the operation is to full load, the closer the ignition can be be located to ITDC. There also exists a rise of optimum ignition angles along the engine speed axis, because faster turbulent burning velocities cannot totally compensate the shorter times for the combustion process. Especially the surface peak at high engine speeds and low loads has to be considered with caution because it doesn't evolve from physics but from map extrapolation at the margins. These parts of the engine map are normally not used in engine operations and are not subject to simulation. Also the optimum ignition angles in knock risky regimes must be reviewed, having in mind that there exists a limitation to mechanics which is not covered in this model so far.

The air-fuel ratio curves in figure 6.6 (left) show the decline of combustion *imep* for different loads ("idling" and full load) at 6000RPM for the *BMW N20B20* engine. Generally, the behavior is similar for varying operations, but for real hardware at full load one is obliged to pay attention to critical temperature limits at the exhaust. Air-fuel ratio curves can then only be driven up to a critical minimum level of exhaust
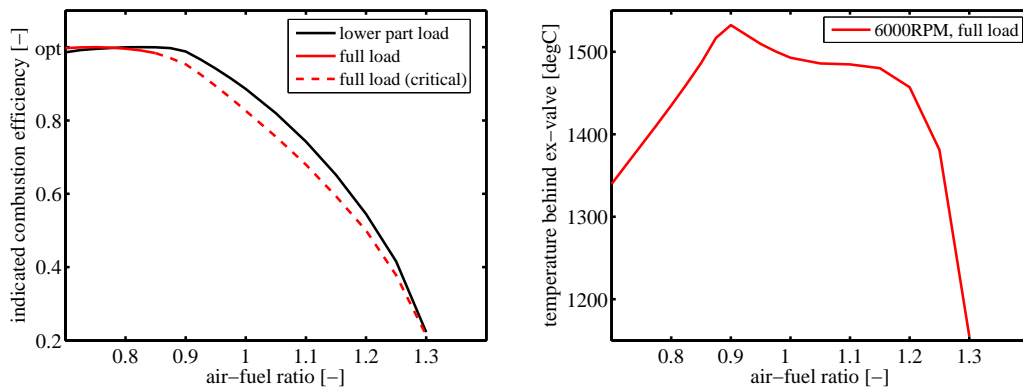
Figure 6.6: Air-fuel ratio curves for differing engine loads at 6000RPM (left) and dependency of the exhaust gas temperature on AFR (right).

gas cooling. For leaner mixtures lacking data can only be acquired via simulation (dashed line) or extrapolation. Figure 6.6 (right) points out that for the *BMW N20B20* aggregate the temperature behind the exhaust valves has its peak at slightly rich mixtures (again because of laminar burning chemistry). Apart from that mixture quality, the temperature is falling, hence fuel mass variation can be used for cooling effects. If one imagines a certain *critical* temperature level below the stoichiometric one, it's obvious that full load points at high engine speeds can only be driven with rich or very lean mixture. (Here, lean operation faces the problems of lacking power output and extensive NO pollutant fractions.)

The greatest potentials of virtual ECU torque model calibration lie within the simulation of similar engines, different operation states ("warm" and "secure" operation, "emergency operation" etc.) and refinement of calibration data instead of extensive remeasurement as well as providing guidelines in early development stages.

6.2 ECU exhaust gas temperature.

The exhaust gas temperature is a central input for many vehicle related ECU functions that cover e.g. engine warm up, component protection, catalytic conversion and on-board diagnosis (OBD). There are several reasons, why the temperature is modeled instead of sensor application:

- thermocouples often lack dynamic response because of their reaction time constants and can therefore only sense low-passed temperature averages

- temperature information is needed at several locations in the exhaust system (e.g. prior to turbine, prior to the lambda sonde and next to the catalytic converter)

- exhaust gas composition leads to abrasion of sensor material and lowers its durability

- sensor fouling via particular matter might bias its output over life time (sensor drift)

Hence, the modeling of exhaust gas temperatures combines robustness, cost effectiveness and dynamics for all dependent ECU software parts.

In general the temperature function provides its results for two different concerns. One serves *component protection* and can be seen as inverse calculation. For the life time endurance of all components in the "hot end" part of the exhaust system, the mentioned function part requests a mixture enrichment which assures that temperature limits are not exceeded (cooling effect). This assures the functionality of turbocharger and catalytic converter when it comes to engine operations in power output areas. On the other hand the straight forward calculation concerns the reaction of the *exhaust gas temperature* on engine actuators at dynamic conditions. These information are important e.g. for early mixture controls after cold start (heating of the lambda sonde), engine fan control after engine stop and the diagnosis of oxygen storage capacity (OSC) of catalysts, which highly depends on boundary temperatures.

The calibration of the overall ECU function for exhaust gas temperature is very demanding in terms of time and resources. The work flow at the test bed is performed via steady state measurements. Therefore recorded temperatures have to be stationary which involves long thermal time constants. Later in the calibration process, substantial experiments at the real hardware vehicle/engine variants are performed to model wall heat transfers of the exhaust system for different driving situations. All in all parts of the complex calibration process can be accelerated and supported via virtual methods.

6.2.1 Description of the functional calculation.

The exhaust temperature function practically executes two consecutive stages of calculation. The first step looks at the *temperature formation* in the cylinder at *"engine cycle end"*, when the exhaust valves open. Accumulated released enthalpies depend on the prior combustion process as well as on in-cylinder heat transfer rates. Hence, the formation part can be evaluated with the help of a physical combustion model and added-on engine cycle simulation. The following step in the ECU function takes temperature and enthalpy information and computes diffusive *temperature drops* due to wall heat losses in the *exhaust manifold*. Modeling approaches are rather complex as several differential equations distinguish inner convection between gas and tube walls and outer convection/radiation between exhaust pipes and drifty air in the engine

compartment. The degree of heat transfer highly depends on the individual system assembly and three-dimensional flow field formation [36, 48, 100]. Especially a waste gated turbocharger requires special attention as it behaves like a highly variable heat sink. Hence, the data for individual component temperatures and velocity related convection are still measured individually in each vehicle configuration.

Inner cylinder processes. The 0D virtual calibration of the exhaust temperature ECU function concentrates on in-cylinder *temperature formation*, which is mostly vehicle-independent. Its modeling can be seen in figure 6.7. This ECU sub-function is realized
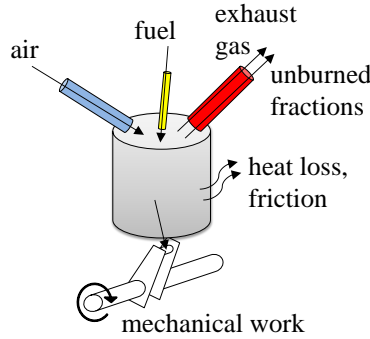
Figure 6.7: Energy flow scheme for in-cylinder *temperature formation* T_{ex} at exhaust-valve opening.

as lossy thermodynamic system with permeable boundaries (mass and energy transfer). Enthalpies from the entering air and fuel as well as its heating value are balanced with draining energy flows. Exiting flows sum up as mechanical work done to the crank train, gas heat losses, chemically bonded enthalpy from unburned fuel fractions (especially for rich mixtures) and thermal enthalpy of the exhaust gas.

A massive simplification for the real-time ECU processing is achieved, when enthalpy flows are calculated with the help of slow sensor signals $\overline{\dot{m}} = \dot{m}_{sensor}$ and mean heat capacities as in equation 6.3.

$$\dot{H} = \int_{T_{ref}}^{T} \dot{m} \cdot c_p(T) \cdot dT \approx \overline{\dot{m}} \cdot \overline{c}_p \cdot \Delta T \tag{6.3}$$

with

$$\Delta T_i = (T_i - T_{ref}).$$

139

This allows to form the energy budget in equation 6.4 for an open thermodynamic system as in figure 6.7.

$$\Delta T_{ex} = \frac{1}{1 + \lambda \cdot m_{stoi}} \cdot \frac{1}{c_{p,ex}} \cdot$$
$$\left[H_u + \lambda \cdot m_{stoi} \cdot \left(c_{p,air} \cdot \Delta T_{air} - \frac{P_{mech} + \sum \dot{Q}_{httr} - \dot{H}_{chem}(\lambda)}{\dot{m}_{air}} \right) \right] \quad (6.4)$$

Keeping in mind, that this expresses the cylinder gas temperature difference (compared to a reference temperature) when the exhaust valves open, the ECU needs special input accuracies from the following functions:

- air charge determination, $\dot{m}_{air} \propto voleff \cdot n_{mot}$

- engine torque model, $P_{mech} \propto bmep$

A greater deviation of these functional inputs directly induces worse accuracies for the thermodynamic ECU model. Moreover the burned fuel should be well-known to determine lower heating value H_u, stoichiometric fraction m_{stoi} and heat capacity $c_{p,ex}$. The chemical bonded energy H_{chem} in unburned fractions of the exhaust gas can be interpreted as combustion efficiency for steady states in terms of air-fuel ratio λ.

$$\lambda \cdot m_{stoi} \cdot \frac{\dot{H}_{chem}(\lambda)}{\dot{m}_{air}} = \frac{H_{chem}(\lambda)}{m_{fuel} \cdot H_u} \cdot H_u = (1 - \eta_c(\lambda)) \cdot H_u \quad (6.5)$$

Thus, H_{chem} can be determined in different ways: while at the test bed, the unburned exhaust components are recorded because they contain remaining caloric potential. Otherwise, finding combustion efficiencies is the effective way of calculation for combustion simulations.

In equation 6.4 the gas' total heat flux is inserted in term $\sum \dot{Q}_{httr}$, which assumes a distribution of heat into the coolant and the oil circuit.

$$\sum \dot{Q}_{httr} = \dot{Q}_{coolant} + \dot{Q}_{oil} = \dot{Q}_{gas} \quad (6.6)$$

Thereby, the summation in equation 6.6 doesn't consider the term of "outer convection" from the engine block which originates from a heat up of cylinder metals and its following direct release to the surrounding air flow – this handshake works without liquid media in between. (It could be found that this term is hardly to measure at all with conventional methods and defines a rather small fraction of the total heat flux [81]. For the ECU function, this results in a simple constant or nil calibration of "outer convection" for in-cylinder *temperature formation*.)

It's obvious, that the calibration of the ECU function needs to know about the fragmentation of total gas heat losses into coolant and oil fluid, compare equation 6.6. Therefore,

the flux into the cooling water is modeled as function of four input parameters like

$$\dot{Q}_{coolant} = f(n_{mot}, voleff, \lambda, \alpha_{ign}). \tag{6.7}$$

Heat losses bearing on oil heat up form independently and can be sufficiently modeled with regard to only engine speed and load.

$$\dot{Q}_{oil} = f(n_{mot}, voleff) \tag{6.8}$$

Summarizing, for the calibration of the exhaust temperature function, the terms for combustion efficiency η_c, heat losses to the coolant $\dot{Q}_{coolant}$ and heat losses to the oil circuit $\dot{Q}_{oil}$ must be defined. Together with the inputs from the ECU air charge determination and the ECU engine torque model, they form the exhaust gas temperature at exhaust valve opening, cf. equation 6.4.

6.2.2 Requirements and conduction of simulation experiments.

Virtual methodology with a 0D combustion model might boost the early availability of calibration data for the ECU exhaust gas temperature function and expand available operation ranges of the aggregate (e.g. stoichiometric high speed/load points). This helps the ECU function to deal with rather physical data inputs instead of pure extrapolation even if objectives cannot be measured at the test bed. This and the possibility of parameter variations emphasize the chance of virtual engine map exploration. Regarding main equation 6.4, the engine cycle simulation can contribute to a variety of ECU maps:

- Virtual air charge determination [62, 88] and virtual engine torque modeling (compare section 6.1) already showed its capabilities.

- Gas heat losses $\dot{Q}_{gas}$ can be calibrated with standard approaches.

- Combustion efficiency η_c is to be read out at the very end of combustion.

- For problem closure one evaluates the cylinder temperature T_{ex} at exhaust valve opening.

This virtual method shares the advantages and potentials of the engine torque model section 6.1.2. Especially for low load points, the steady state simulation is rather fast in comparison to thermal time constants at the test bed, gaining real-time advantages. As drawback one has to consider the influence of incident air flow from the test bed fan which cannot be trivially rebuilt in engine cycle simulations. It is assumed to be of minor importance [81]. Moreover, all Newtonian approaches for in-cylinder thermal losses need exact gas to wall temperature gradients which relatively limits the acquirable accuracy.

Conduction of simulations. The setup of a simulation grid is very much alike the method in section 6.1.2 except that now ignition curves are less important. Instead, only pre-calibrated engine points are simulated (actuation comes from basic calibration and the engine torque model itself). Performing few ignition curves and air-fuel ratio curves like in figure 6.1 produce extra knowledge on the behavior of $\dot{Q}_{coolant}$ in equation 6.7.

The simulation environment leaves three possibilities for thermodynamic and thermal engine cycle coupling:

1. *direct* coupling – parallel simulation of the thermal cooling/oil circuit with inputs and information back flow to the predictive combustion model

2. *indirect* coupling – separate computation of the in-cylinder combustion model and uni-directional data transfer just to the thermal environment

3. *no* coupling – predictive computation of combustion and later fragmentation of heat losses, due to equation 6.6

The first method was succesfully performed by Knoll [45] with a thermal structure model. Direct coupling covers the back link of thermal system changes (wall temperatures etc.) to the combustion process. A big disadvantage lies in the high complexity of the data transfer, overall computation times and the stability of simulation. Seider [95] therefore couples the simulation environments in an indirect way. At first the thermal boundary conditions (heat transfer rates and heat transfer coefficients) are stored into data files. These data are obtained from detailed 0D combustion calculations. Afterwards, the data files are given to the thermal structure simulation, iterating heat flux fragmentation. This type of coupling is comparably faster because of little iteration cycles but cannot cover reciprocal effects. Moreover the thermal model needs detailed knowledge from thermal test beds in advance.

For this work, the method with *no coupling* was chosen. The back link of steady state combustion seems rather negligible because only engine warm up is seen as critical. Moreover, the thermal structure model produces the same results as the thermal test bed measurements presets. So the most efficient way for this kind of steady state calibration is to simply fragment the gas heat losses with pre-measured data from previous engine derivates or previous construction levels.

The whole simulation procedure involved to compute several complete engine maps and some air-fuel ratio variations as ignition variations as well. This took around 2 days on 4 parallel processors.

6.2.3 Calibrating the ECU exhaust gas temperature.

At first, the calibration process shall prove its ability to reproduce basic qualities of the thermal test bed measurement. Therefore, several experiments were compared, see

figure 6.8. It can be seen that the general quality of the maps agrees as cumulated
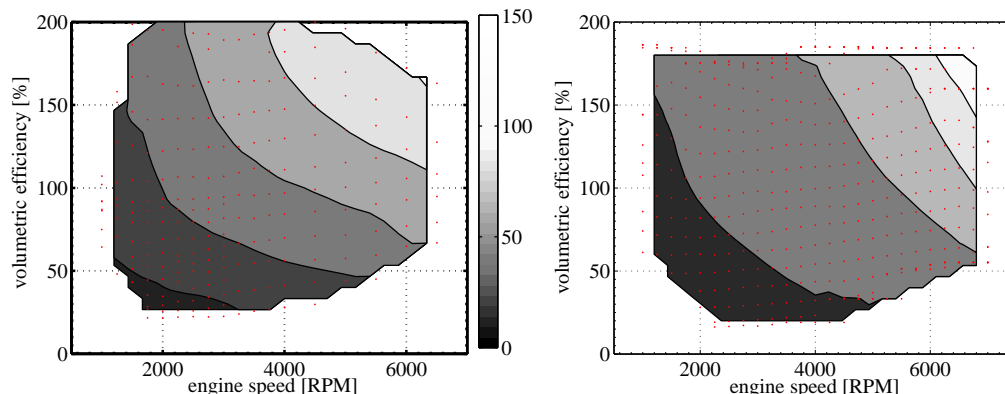

Figure 6.8: Comparison of gas heat losses $\dot{Q}_{gas} = \dot{Q}_{coolant} + \dot{Q}_{oil}$ [kW] from simulation (left) and thermal test bed (right)

heat losses scale with load and engine speed. (Here, the load axis has chosen to be relative air charge to not compare possible deviations between the engine torque model outputs.) The interesting difference between the maps shown here, lies in the data acquisition: the thermal test bed measurement (right) drives constantly at a coolant temperature of 105°C and an oil temperature of 110°C. The reasons can be seen in a better data handling for the later thermal modeling. Nevertheless, this situation is rather not realistic because part load combustion efficiency and knock behavior can be optimized with only differing coolant temperatures. This is why the engine cycle simulation in figure 6.8 (left) was performed with realistic thermostatic values for coolant temperatures ranging from 85-110°C in the map. (For oil-water cooling systems the oil temperature is more or less coupled to the coolant.) Moreover the optimum parameters for valve control, injection and turbo charging are input to the simulation but weren't yet available for the earlier thermal test bed process. This explains the differing map boundaries in figure 6.8 and why some points are "overestimated" by the simulation while others are "underestimated".

Figure 6.9 shows the fraction $Q_{gas}/m_{fuel} \cdot H_u$ of wall heat losses compared to the total fuel energy for one cycle. It is interesting to note, that the plot's maximum value lies around 35% and its minimum around 15%. The rule of thumb (saying that 1/3 of total fuel energy is equally devoted to exhaust gas enthalpy, production of mean effective pressure and gas heat losses) can only be applied for the lower left corner of the map. Moreover, whereas absolute values of gas heat losses maximize at high load/high speed as in figure 6.8, the thermal efficiency of high pressure cycles maximizes meanwhile.

A fragmentation of total gas heat losses $\dot{Q}_{gas}$ to coolant and oil flow can be found in

143
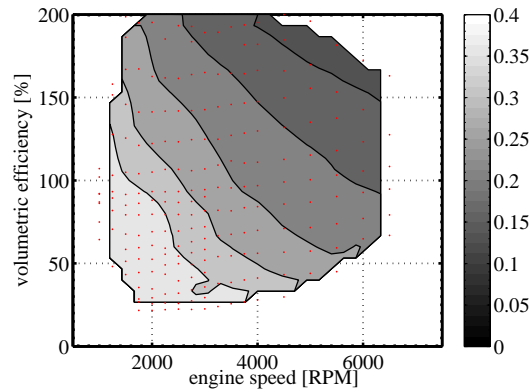
Figure 6.9: Simulated fraction [-] of fuel energy $m_{fuel} \cdot H_u$ that produces in-cylinder gas heat losses Q_{gas}.

plots of figure 6.10. The coolant can take much more heat, because its heat capacity is
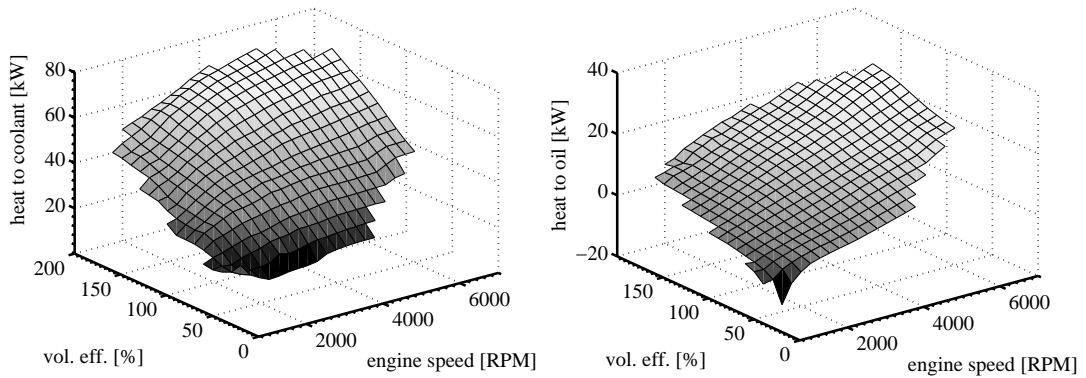
Figure 6.10: Calculated heat to coolant $\dot{Q}_{coolant}$ (left) and oil $\dot{Q}_{oil}$ (right) for optimum ignition and stoichiometric mixture.

quite high, so is its thermal mass. Moreover the map for $\dot{Q}_{coolant}$ looks rather uniform and more or less shares the quality of total heat losses. The correlation looks different for $\dot{Q}_{oil}$, which very much follows the hyperbola of equal power output. Not only, that the parasitic heat to the oil is lower than to the coolant, moreover $\dot{Q}_{oil}$ switches signs also. For its negative values in figure 6.10, the oil is externally heated and loses temperature to the cylinder gas or the walls. This effect is known in thermal experiments as *heat*

input. Plot 6.10 (right) already satisfies the ECU oil heat model, because it is assumed to be independent of later ignition angles and differing mixture richness. For the coolant heat the mentioned parameters have to be considered, compare figures 6.11 and 6.12.

Figure 6.11 is an ignition variation for the *BMW N20B20* engine and shows that
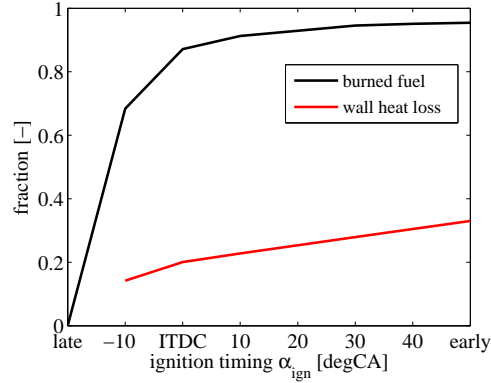
Figure 6.11: Simulated effects of an ignition timing variation on burn out η_c and wall heat losses at 2000RPM/ *bmep* 2bar (VVT).

leaving the optimum ignition going to ITDC leaves the mixture less time to burn which results in a lower burned fuel fraction. At the same time, the overall heat loss fraction lessens, because the combustion cannot produce as high temperatures anymore – the temperature gradient to the wall decreases. Hence, for a later ignition the energy balance shifts to the term $\dot{H}_{chem}$ because the exhaust gas still contains high potential in unburned HC and incompletely burned CO emissions. For even later ignition angles, this trend enforces while burned fuel fractions drop dramatically, ending even in misfire. The total gas heat losses follow this behavior. When the burned fuel fraction hits nil, this causes an undefined mathematical situation because

$$f_{Q_{gas}} = \frac{Q_{gas}}{\eta_c \cdot m_{fuel} \cdot H_u} \tag{6.9}$$

and $\eta_c \to 0$. At misfire the fraction of total gas heat losses would lift up and trend to infinity, thus being greater than the inserted energy of the fuel. For the ECU function, it can be assumed that $\Delta f_{Q_{coolant}} = \Delta f_{Q_{gas}}(\alpha_{ign})$ at the steady part of the curve, compare modeling equations 6.7 and 6.8. (Hereby, $f_{Q_{coolant}}$ forms by replacing Q_{gas} with $Q_{coolant}$ in equation 6.9).

Figure 6.12 observes a variation of mixture quality for the *BMW N20B20* engine. In the left plot, the reaction of heat flux to the coolant has its peak at stoichiometric mixtures. For richer operation, the heat flux decreases around 20% which can be explained with

Figure 6.12: Simulated effects of an air-fuel ratio variation on the relative coolant heat flux changes $\dot{Q}_{coolant}$ (left) and burned fuel efficiency η_c (right).

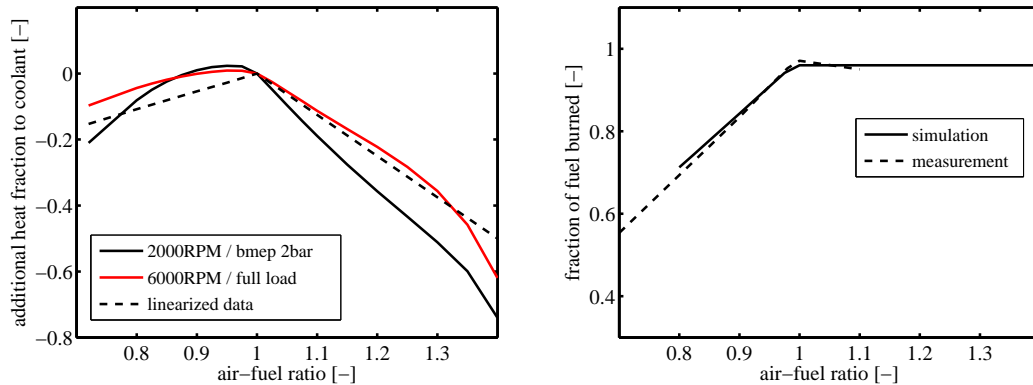enhanced injection cooling and an operation with higher laminar burning velocities which is closer to the ideal Otto cycle. This effect is more significant for 2000RPM than for 6000RPM because for longer time scales the thermodynamic efficiency is worse. For leaner operation, cylinder temperatures fall and the temperature gradient to the wall decreases. This induces smaller heat flux to the coolant. The linearized plot data would be typically handed to the ECU for the coverage of engine behavior especially at rich operation.

Figure 6.12 (right) simulates a variation of mixture quality on burning efficiency η_c for the sample operation at 6000RPM, fuel load. Again, in the rich regime the burn out is incomplete. For 20% additional fuel mass at $\lambda = 0.8$ the burn out drops 30%. This meets quite well the expected values from a sample measurement. For $\lambda = 1$ and lean mixtures the simulation predicts nearly all masses to be burned. This may be alright from the sight of chemical mass balancing but ignition and burn out quenching normally don't permit this optimistic outsight. In this work, a stoichiometric and homogeneous injection concept is considered and lean operation doesn't occur so far. For fuel stratification and lean engines, the combustion model should be operated in wider ranges.

For the calibration of the ECU exhaust gas temperature model with real hardware, at the very beginning of the process, one invests great efforts into the sensor systems and the measuring methods. The calibration of the model using a thermal and/or a stationary test bed involves high costs and many iteration loops. Here, the 0D combustion model can deliver the relevant data (η_c, $\dot{Q}_{coolant}$, $\dot{Q}_{oil}$) earlier which can then be used and "tuned" in a later fine-calibration on the test bed.

7 Summary and outlook.

Summary.

In this work a physical 0D combustion model is set up, which can cope with a new generation of spark ignition engines. Therefore, the following sub models were individually developed and validated:

- *thermodynamics* to provide the inputs to the chemical laminar burning velocity,

- *quasi-dimensional turbulence and global charge motion* to provide additional inputs to the turbulent burning velocity,

- *physical ignition delay* for a quasi-dimensional estimation of the beginning combustion process,

- *combustion based on an entrainment approach* to capture the burn-out phase of the combustion process.

The interaction between the aforementioned sub models was secured and validated in the whole engine operation map. After that, the complete combustion model was used to show its industrial applicability within the *virtual engine calibration* considering engine torque production and the exhaust gas temperature.

Outlook.

For the introduced 0D combustion model, there exist a variety of possible future applications which can be entered with some extra modeling effort. This virtual approach can relax the goal conflict of time cut, cost cut and quality gain.

Higher modeling depth. The following sub-model extensions might provide further insights into engine operation:

- a *knock* model helps to determine ignition limits [83, 101]

- *cyclic variations* can deliver maximum residual gas mass fractions (degree of unthrottling) [34]

- a *scavenging* model determines trapped cylinder components for high VVT valve overlap and positive pressure gradients

- laminar *burning velocity* formulations for alternative fuels and ethanol blends expand the simulation width

- description of *emissions* forwards engine point optimization [11, 56, 83]

- *transient* combustion processes open up driving cycle simulation

- ...

Further model applications. *Basic engine calibration* of VVT valve control and ignition timing will be a potential new field of application if the combustion model is able to predict drivability limits for each steady state operation. The ECU *boost pressure control* function can be calibrated with the knowledge how the virtual system reacts on step functions of actuators (tip-in maneuver). For *mechanical optimization* and *acoustic experiments* the combustion simulation can deliver input data and be part of the iteration process. The *Hardware-in-the-Loop* platform (HiL) could process predictive combustion for model based control strategies. Herefore all sub-models must be enabled to compute in real-time, which can be achieved equivalent to the neural network methodology in the thermodynamic chapter.

8 Bibliography

[1] Munnannur Achuth and Pramod S. Mehta. Predictions of Tumble and Turbulence in Four Valve Pentroof Spark Ignition Engines. *International Journal of Engine Research*, Vol. 2, No. 3:pp. 209–228, 2001.

[2] Munnannur Achuth, Ganesa Subramanian, and Pramod S. Mehta. Model Predictions for Tumble and Turbulence in SI Engine Combustion Chambers. *SAE*, 2001-28-0013, 2001.

[3] Matthias Auer. *Erstellung phänomenologischer Modelle zur Vorausberechnung des Brennverlaufes von Magerkonzept-Gasmotoren*. PhD thesis, TU München, 2010.

[4] Christian Barba. *Erarbeitung von Verbrennungskennwerten aus Indizierdaten zur verbesserten Prognose und rechnerischen Simulation des Verbrennungsablaufes bei Pkw-DE-Dieselmotoren mit Common-Rail-Einspritzung*. PhD thesis, Eidgenössische Technische Hochschule Zürich, 2001.

[5] Michael Bargende. Turbulenzmodellierung für quasidimensionale Arbeitsprozessrechnung - FVV M2709. Research proposal. 2010.

[6] Michael Bargende. *Ein Gleichungsansatz zur Berechnung der instationären Wandwärmeverluste im Hochdruckteil von Ottomotoren*. PhD thesis, TU Darmstadt, 1991.

[7] Michael Bargende, Christine Burkhardt, and Alfred Frommelt. Besonderheiten der thermodynamischen Analyse von DE-Ottomotoren. *Motortechnische Zeitschrift*, 2001.

[8] Norman C. Blizard and James C. Keck. Experimental and Theoretical Investigation of Turbulent Burning Model for Internal Combustion Engines. *SAE*, 740191, 1974.

[9] Claus Borgnakke, Vedat Arpaci, and Rodney Tabaczynski. A Model for the Instantaneous Heat Transfer and Turbulence in a Spark Ignition Engine. *SAE*, 800287, 1980.

[10] Konstantinos Boulouchos, Tobias Steiner, and Panayotis Dimopoulos. Investigation of flame speed models for the flame growth period during premixed engine combustion. *SAE*, 940476, 1994.

[11] Franz Chmela, Dimitar Dimitrov, Benjamin Losonczi, Gerhard Pirker, Harald Schlick, and Andreas Wimmer. Möglichkeiten und Grenzen der null-dimensionalen Simulation des Arbeitsprozesses von Großmotoren. In *12. Tagung: Der Arbeitsprozess des Verbrennungsmotors*, 2009.

[12] Peter Csallner. *Eine Methode zur Vorausberechnung der Änderung des Brennverlaufes von Ottomotoren bei geänderten Betriebsbedingungen.* PhD thesis, TU München, 1981.

[13] Wen Dai, Charles E. Newman, and George C. Davis. Predictions of In-Cylinder Tumble Flow and Combustion in SI Engines with a Quasi-Dimensional Model. *SAE*, 961962, 1996.

[14] Pol Daleiden. Kennfeldweite Modellierung des Brennverzugs in einem turboaufgeladenem Benzindirekteinspritzer-Motor mit variablem Ventiltrieb mittels Simulation und Versuch. Master thesis, TU Kaiserslautern, 2010.

[15] Manuel Dorsch. Echtzeitfähige 1D Thermodynamikmodellierung für die Motorapplikation direkteinspritzender Benzinmotoren. Master thesis, Universität Stuttgart, 2011.

[16] Franz Durst. *Grundlagen der Stroemungsmechanik - Eine Einfuehrung in die Theorie der Stroemungen von Fluiden.* Springer-Verlag Berlin, 2006.

[17] Helmut Eichert, Michael Günther, and Steffen Zwahr. Simulationsrechnungen zur Ermittlung optimaler Einspritzparameter an DI-Ottomotoren. *Automobiltechnische Zeitschrift*, 2005.

[18] Helmut Eichlseder, Manfred Klüting, and Walter F. Piock. *Grundlagen und Technologien des Ottomotors – Der Fahrzeugantrieb.* SpringerWienNewYork, Helmut List, 2008.

[19] Christian Eiglmeier. *Phänomenologische Modellbildung des gasseitigen Wandwärmeüberganges in Dieselmotoren.* PhD thesis, Uni Hannover, 2000.

[20] Jens Ewald. *A Level Set Based Flamelet Model for the Prediction of Combustion in Homogeneous Charge and Direct Injection Spark Ignition Engines.* PhD thesis, RWTH Aachen, 2006.

[21] Ingo Friedrich. *Motorprozess-Simulation in Echtzeit - Grundlagen und Anwendungsmöglichkeiten.* PhD thesis, Technische Universität Berlin, 2008.

[22] Stefan Frommater. Analyse und Bewertung verschiedener Modellansätze zur Beschreibung des ottomotorischen Wandwärmeübergangs. Bachelor thesis, TU Bergakademie Freiberg, 2012.

[23] Daniel Gohl. Analyse der Auslegung und Bewertung von Einlasskanälen. Master thesis, ETH Zürich, 2005.

[24] Rainer Golloch. *Downsizing bei Verbrennungsmotoren – Ein wirkungsvolles Konzept zur Kraftstoffverbrauchssenkung.* SpringerVerlag Berlin, VDI Buch, 2005.

[25] Dimity Goryntsev, Amsini Sadiki, Michael Klein, and Johannes Janicka. Large Eddy Simulation Based Analysis of the Effects of Cycle-to-Cycle Variations on Air-Fuel Mixing in Realistic DISI IC-Engines. *Proc. Combust. Inst.*, Vol 32, 2009.

[26] Sebastian Grasreiner. Analyse eines direkteinspritzenden Turbo-Ottomotors mit variabler Ventilsteuerung am optischen Motor. Master thesis, TU Ilmenau, 2008.

[27] Sebastian Grasreiner. Virtualisierung der Applikation für Otto-TVDI-Motoren - Ein physikalisches Brennverlaufsmodell zur Serienentwicklung. In *ProMotion2009*, 2009. Lecture.

[28] Sebastian Grasreiner, Christoph Luttermann, and Christian Hasse. Echtzeit-fähige Thermodynamikmodellierung von neuen Ottomotoren der BMW Group - ein Beitrag zur kennfeldweiten und physikalischen Verbrennungsvorhersage. In *Motorische Verbrennung - Aktuelle Probleme und moderne Lösungsansätze*, 2011.

[29] Sebastian Grasreiner, Christoph Luttermann, Jens Neumann, and Christian Hasse. Quasi-dimensional modeling of turbulence and global charge motion for new BMW spark ignition engines - a contribution to physical combustion predictions. In *8th Symposium: Powertrain Control Systems For Motor Vehicles*, 2011.

[30] Michael Grill. *Objektorientierte Prozessrechnung von Verbrennungsmotoren.* PhD thesis, Universität Stuttgart, 2006.

[31] Michael Grill and Michael Bargende. Quasidimensionale Verbrennungsmodellierung und 1-D-Strömungssimulation an Ottomotoren. In *7. Internationales Stuttgarter Symposium, Automobil- und Motorentechnik*, 2007.

[32] Michael Grill, Thomas Billinger, and Bargende Michael. Quasi-Dimensional Modeling of Spark Ignition Engine Combustion with Variable Valve Train. *SAE*, 2006-01-1107, 2006.

[33] Lino Guzzella and Christopher Onder. *Introduction to Modeling and Control of Internal Combustion Engine Systems .* Springer Verlag Berlin, 2004.

[34] Christian Hasse, Volker Sohm, and Bodo Durst. Numerical Investigation of Cyclic Variations in Gasoline Engines Using a Hybrid URANS/LES Modeling Approach. *Computer and Fluids*, Vol 39:25–48, 2010.

[35] Johann Hauber. Kreisprozessrechnung als Echtzeitmodell für Hardware-in-the-Loop-Anwendungen. Master thesis, Hochschule München, 2005.

[36] Stefan Heller. *Analyse und Modellierung des instationären Wärmeübergangs in der ottomotorischen Abgasanlage.* PhD thesis, TU München, 2009.

[37] Ruediger Herweg and Rudolf Maly. A fundamental model for flame kernel formation in S.I. engines. *SAE*, 922243, 1992.

[38] John B. Heywood. *Internal Combustion Engine Fundamentals.* McGraw-Hill, 1988.

[39] Stefan Hildenbrand, Stefan Staudacher, Dieter Brüggemann, Frank Beyrau, Markus C. Weikl, Thomas Seeger, and Alfred Leipertz. Numerical and experimental study of the vaporization cooling in gasoline direct injection sprays. *ScienceDirect*, 2006.

[40] Knut G. Hockel. *Untersuchung zur Laststeuerung beim Ottomotor.* PhD thesis, TU München, 1982.

[41] Nataliya Hunzinger, Markus Rothe, Ulrich Spicher, Tim Gegg, Martin Rieber, Axel Klimmek, and Andreas Jäger. Quasi-Dimensional Combustion Simulation of a Two- Stroke Engine. *SAE*, 2006-32-0062, 2006.

[42] Eduard Köhler and Rudolf Flierl. *Verbrennungsmotoren – Motormechanik, Berechnung und Auslegung des Hubkolbenmotors.* Vieweg+Teubner, 2009.

[43] Norbert Klauer, Manfred Klüting, Fritz Steinparzer, and Harald Unger. Aufladung und variable Ventiltriebe – Verbrauchstechnologien für den weltweiten Einsatz. In *Wiener Motorensymposium*, 2009.

[44] Manfred Klüting, Stephan Missy, and Christian Schwarz. Potenziale des Strahlgeführten Benzin-DI-Brennverfahrens in Verbindung mit Aufladung. In *Wiener Motorensymposium*, 2005.

[45] Ulrich Knoll. Eindimensionale Motorprozessrechnung eines turboaufgeladenen Benzindirekteinspritzer-Motors mit variablem Ventiltrieb für die virtuelle Steuergerätebedatung. Master thesis, Hochschule München, 2011.

[46] Peter Koch. *Tracer-LIF-Techniken als Werkzeug zur Optimierung moderner direkteinspritzender Ottomotoren.* PhD thesis, FAU Erlangen-Nürnberg, 2010.

[47] Franck Koppes. Echtzeitfähige Thermodynamikmodellierung für die Motorapplikation direkteinspritzender Benzinmotoren. Master thesis, TU Kaiserslautern, 2009.

[48] Matthias Kratzsch, Michael Günther, Nick Elsner, and Steffen Zwahr. Modell-ansätze für die virtuelle Applikation von Motorsteuergeräten. *Motortechnische Zeitschrift*, 09/2009:p. 664–670, 2009.

[49] David Kriesel. *Neuronale Netze.* Rheinische Friedrich-Wilhelms-Universität, 2006.

[50] Peter Langen and Wolfgang Nehse. BMW EfficientDynamics – Blick in die Zukunft. In *30. Internationales Wiener Motorensymposium*, 2009.

[51] Peter Langen, Jörg Reissing, and Matthias Klietz. Hochentwickelte Antriebe – kein Widerspruch zur Profitabilität. In *19. Aachener Kolloquium "Fahrzeug- und Motorentechnik"*, 2010.

[52] Micha Löffler and Alfred Beyrau, Frank und Leipertz. Acetone laser-induced fluorescence behaviour for the simultaneous quantification of temperature and residual gas distribution in fired spark-ignition engines. *Applied Optics*, 49:37–49, 2010.

[53] Dirk Linse. Einfluss der Einlasskanal-induzierten Ladungsbewegung auf die Brenngeschwindigkeit in einem direkteinspritzenden Ottomotor. Master thesis, RWTH-Aachen, 2006.

[54] Dirk Linse, Christian Hasse, and Bodo Durst. An Experimental and Numerical Investigation of Turbulent Flame-Propagation and Flame Structure in a Turbo-Charged Direct Injection Gasoline Engine. *Combustion Theory and Modeling,*, 13:167–188, 2009.

[55] Dirk Linse, Christian Hasse, Bodo Durst, and Christian Schwarz. Kombinierte experimentelle und numerische Analyse der turbulenten Flammenausbreitung und -struktur in einem direkteinspritzenden Ottomotor. In *23. Deutscher Flammentag, VDI-Berichte Nr. 1988, 277-282*, 2007.

[56] Dirk Linse, Andreas Kleemann, Bodo Durst, and Christian Hasse. Simulation der Stickoxidemissionen von direkteinspritzenden Ottomotoren mit einem gekoppelten CFD-Multizonenmodell. In *Motorische Verbrennung - Aktuelle Probleme und moderne Lösungsansätze*, 2011.

[57] Christian Lämmle. *Numerical and Experimental Study of Flame Propagation and Knock in a Compressed Natural Gas Engine.* PhD thesis, ETH Zürich, 2005.

[58] Michael Loy. Analyse des Einflusses von Einlasskanal-Formparametern auf die Ladungsbewegung und Optimierung der Einlasskanalgeometrie mit Hilfe software-gestützter multi-objektiver Optimierungsverfahren. Master thesis, TU München, 2005.

[59] Rudolf Maly and Manfred Vogel. Initiation and Propagation of Flame Fronts in Lean CH4-Air Mixtures by the Three Modes of the Ignition Spark. *Proceedings of the Combustion Institute*, 17:821–831, 1978.

[60] Günter Merker, Christian Schwarz, Gunnar Stiesch, and Frank Otto. *Verbrennungsmotoren - Simulation der Verbrennung und Schadstoffbildung.* Teubner Verlag, 2006.

[61] James C. Metghalchi, Mohamad; Keck. Burning velocities of mixtures of air with methanol, isooctane, and indolene at high pressure and temperature. *Combustion and Flame*, pages 191–210, 1982.

[62] Wolfgang Mühlbauer. Echtzeitfähige Modellierung der laminaren Brenngeschwindigkeit in komplexen Ottomotoren. Master thesis, FAU Erlangen-Nürnberg, 2010.

[63] Andrea Milocco. *Ein flexibles, semi-empirisches Verbrennungsmodell für unterschiedliche ottomotorische Brennverfahren.* PhD thesis, TU Braunschweig, 2007.

[64] Alexander Mitterer, Heiko Konrad, Gerd Krämer, and Norbert Siegl. Entwicklung und Applikation von modellbasierten Steuergerätefunktionen am Beispiel der neuen BMW Reihen-Sechszylindermotoren mit Valvetronic. In *Autoreg VDI/VDE*, 2006.

[65] Thomas Morel, Charles I. Rackmil, Rifat Keribar, and Mark J. Jennings. Model for Heat Transfer and Combustion In Spark Ignited Engines and its Comparison with Experiments. *SAE*, 880198, 1988.

[66] Christoph Natkaniec. Einfluss der Kolbenstellung auf den Durchflussbeiwert der Drosselströmung an den Einlass- und Auslassventilen eines aufgeladenen DI-Ottomotors. Master thesis, Universität Hannover, 2007.

[67] Philippe Neeser, Dirk Linse, Michael Günthner, Christian Hasse, and Hermann Rottengruber. Strategien zur Erweiterung des Betriebsbereichs eines ottomotorischen HCCI-Brennverfahrens. In *Motorische Verbrennung - Aktuelle Probleme und moderne Lösungssätze*, 2009.

[68] Adolf Nefischer. *Quasidimensionale Modellierung turbulenzgetriebener Phänomene in Ottomotoren.* PhD thesis, TU Graz, 2009.

[69] Martin Nijs, Peter Sternberg, Michael Wittler, and Stefan Pischinger. Steuergerätefähige Luftpfadmodelle für Ottomotoren mit erweiterter Ventiltriebsvariabilität. *Motortechnische Zeitschrift*, 2010.

[70] Georg Noske. Ein quasidimensionales Modell zur Beschreibung des ottomotorischen Verbrennungsablaufs. *VDI Fortschrittsberichte*, Reihe 6 211, 1988.

[71] Thomas Offer. *Numerische Lösungskonzepte für die Motorprozess-Simulation.* PhD thesis, Technische Universität Berlin, 1999.

[72] Nir Ozdor, Mark Dulger, and Eran Sher. Cyclic Variability in Spark Ignition Engines A Literature Survey. *SAE*, 940987, 1994.

[73] Norbert Peters. *Four Lectures on Turbulent Combustion - ERCOFTAC Summer School.* RWTH ITV Aachen, 1997.

[74] Norbert Peters. *Technische Verbrennung.* RWTH ITV Aachen, 2009.

[75] Rudolf Pischinger, Manfred Kell, and Theodor Sams. *Thermodynamik der Verbrennungskraftmaschine.* Springer Verlag Wien, 2009.

[76] Stefan Pischinger. *Verbrennungsmotoren – Vorlesungsumdruck.* Rheinisch-Westfälische Technische Hochschule Aachen, 2008.

[77] Stefan Pischinger and John B. Heywood. A study of flame development and engine performance with breakdown ignition systems in a visualization engine. *SAE*, 880518, 1988.

[78] Stefan Pischinger and John B. Heywood. How Heat Losses to the Spark Plug Electrodes Affect Flame Kernel Development in an SI-Engine. *SAE*, 900021, 1990.

[79] Robert Pivec. *Quasidimensionale Modellierung des gasseitigen Wärmeüberganges in Verbrennungsmotoren.* PhD thesis, Technische Universität Graz, 2001.

[80] Stephen B. Pope. *Turbulent Flows.* Cambridge University Press, 2000.

[81] Christian Poruba, Gerald Seider, and Martin Kröner. Energiebilanzierung im Entwicklungsprozess von Motoren. *Wärmemanagement des Kraftfahrzeugs*, Vol. 5, 2006.

[82] Stephen G. Poulos and John B. Heywood. The effect of chamber geometry on spark ignition engine combustion. *SAE*, 830334, 1983.

[83] Maximilian Prager and Georg Wachtmeister. Verbrennungsmodell für einen Hochleistungsgasmotor zur Vorausberechnung von Emissionen, Klopf- und Aussetzergrenze. In *12. Tagung: Der Arbeitsprozess des Verbrennungsmotors*, 2009.

[84] Helmut Pucher and Jörn Kahrstedt. *Motorprozesssimulation und Aufladung.* expert Verlag, 2005.

[85] Damian E. Ramajo, Angel L. Zanotti, and Norberto M. Nigro. Validación de un modelo de tumble y turbulencia para un motor de cuatro válvulas de alto rendimiento. *Mecánica Computacional*, Vol. 24, No. 8:pp. 1527–1542, 2005.

[86] Juan Ignacio Ramos. *Internal Combustion Engine Modeling.* Hemisphere Publishing Corporation, 1989.

[87] Christian Roithmeier. *Virtuelle Applikation von Motorsteuerungsfunktionen am Beispiel der Lasterfassungsfunktion und der Fahrdynamikfunktionen.* PhD thesis, TH Karlsruhe, 2011.

[88] Christian Roithmeier, Nico Neuweiler, Christoph Luttermann, and Alexander Mitterer. Calibration methods for air charge determination based on measurement and simulation data. In *Automotive Workshop Spa*, 2006.

[89] Fred Schäfer et al. *Handbuch Verbrennungsmotor. Grundlagen, Komponenten, Systeme, Perspektiven.* Vieweg+Teubner, Richard van Basshuysen, 2010.

[90] Jens Schäfer, Sebastian Zwahr, and Michael Wensing. INA 3Cam: ein neuartiges System zur mechanisch vollvariablen Ventilsteuerung. In *Variable Ventiltriebe, Haus der Technik*, 2009.

[91] Jens Schäfer, Sebastian Zwahr, Michael Wensing, and Christian Tanasie. 3cam – continuously variable cam shifting valve train. In *CONAT 2010: International congress on Automotive and Transport Engineering*, 2010.

[92] Hans-Peter Schmid. *Ein Verbrennungsmodell zur Beschreibung der Wärmefreisetzung von vorgemischten turbulenten Flammen.* PhD thesis, TH Karlsruhe, 1995.

[93] Claudia Schubert. Drall- und Tumblemodellierung zur Berechnung des Wandwärmeüberganges. Master thesis, Technische Universität Graz, 2001.

[94] Claudia Schubert, Andreas Wimmer, and Franz Chmela. Advanced Heat Transfer Model for CI Engines. *SAE*, 2005-01-0695, 2005.

[95] Gerald Seider and Fabiano Bet. Neue Simulationstechniken - Potenziale für den virtuellen Produktentstehungsprozess. In *Haus der Technik, 7. Tagung: Wärmemanagement des Kraftfahrzeugs*, 2010.

[96] Huixian Shen, Peter C. Hinze, and John B. Heywood. A Model for Flame Initiation and Early Development in SI Engine and its Application to Cycle-to-Cycle Variations. *SAE*, 942049, 1994.

[97] Yu Shi, Hai-Wen Ge, and Rolf D. Reitz. *Computational Optimization of Internal Combustion Engines.* SpringerVerlag Berlin, 2011.

[98] Mitchell D. Smooke. *Reduced Kinetic Mechanisms and Asymptotic Approximations for Methane-Air Flames: A Topical Volume (Lecture Notes in Physics).* Springer Verlag Berlin, 1991.

[99] Ulrich Spicher et al. *Ottomotor mit Direkteinspritzung - Verfahren, Systeme, Entwicklung, Potenzial.* ATZ/MTZ-Fachbuch, Richard van Basshuysen, 2007.

[100] Anastassios Stamatelos and Ioannis Kandylas. Berechnung des Wärmeübergangs in Motorabgassystemen. *Motortechnische Zeitschrift*, 59:p442–450, 1998.

[101] Andrei Stanciu and Jens Neumann. Analyse von Klopfkriterien für die Ladungswechselsimulation aufgeladener Ottomotoren. In *Ottomotorisches Klopfen - irregulaere Verbrennung*, 2010.

[102] Gunnar Stiesch, Christian Eiglmeier, Günter P. Merker, and Friedrich Wirbeleit. Möglichkeiten und Anwendung der phänomenologischen Modellbildung im Dieselmotor. *Motortechnische Zeitschrift*, 60:p. 274–283, 1999.

[103] Rodney. J. Tabaczynski, Colin R. Ferguson, and Krisna Radhakrishnan. A turbulent entrainment model for spark-ignition engine combustion. *SAE*, 770647, 1977.

[104] Kevin V. Tallio and Phillip Colella. A Multi-Fluid CFD Turbulent Entrainment Combustion Model: Formulation and One-Dimensional Results. *SAE*, 972880, 1997.

[105] Henk Tennekes and John L. Lumley. *A First Course in Turbulence.* MIT Press, 1972.

[106] Mario Theissen. *Untersuchung zum Restgaseinfluß auf den Teillastbetrieb des Ottomotors.* PhD thesis, Ruhr-Universität Bochum, 1989.

[107] Stephen R. Turns. *An Introduction to Combustion - Concepts and Applications.* McGraw-Hill, 2006.

[108] Jurij I. Vibe. *Brennverlauf und Kreisprozess von Verbrennungsmotoren.* VEB Verlag Technik, Berlin, 1970.

[109] Mathieu Voisine, Lynda Thomas, Jacques Borée, and Patrick Rey. Spatio-temporal structure and cycle to cycle variations of an in-cylinder tumbling flow. *Exp. Fluids*, 50:1393-1407, 2011.

[110] Markus Wenig and Michael Bargende. Zyklenschwankung. Research report, FVV 995, 2010.

[111] Michael Wensing. *Motorische Verbrennung – Vorlesungsumdruck Friedrich-Alexander Universität Erlangen-Nürnberg.* 2009.

[112] Michael Wensing. Neue Brennverfahren – Möglichkeiten und Anforderungen. In *Ferienakademie der Universitäten Erlangen-Nürnberg, München und Stuttgart, Sarntal, Italien*, 2009. Lecture.

[113] Hardy Weymann, Friedrich Dinkelacker, and Oliver Nelles. Neuronales Berechnungsmodell zur Bestimmung des Brennraumdruckverlaufs. *Motortechnische Zeitschrift*, 2010.

[114] Wolfram Wiese. *Vorhersage von Brennverzug und -dauer bei Ottomotoren auf Basis der Brennraumströmung.* PhD thesis, RWTH Aachen, 2009.

[115] Andreas Witt. *Analyse der thermodynamischen Verluste eines Ottomotors unter den Randbedingungen variabler Steuerzeiten.* PhD thesis, TU Graz, 1999.

[116] Gerhard Woschni. Die Berechnung der Wandwärmeverluste und der thermischen Belastung der Bauteile von Dieselmotoren. *Motortechnische Zeitschrift*, 31:491–499, 1970.

[117] Serge Zakharian, Patricia Ladewig-Riebler, and Stefan Thoer. *Neuronale Netze für Ingenieure.* Vieweg-Verlag, 1998.

A Engine details.

In this work, a new generation of SI engines was subject for combustion modeling. The main technologies combined were

- exhaust gas turbo charging,

- fully variable valve train and

- gasoline direct injection.

The **BMW N20B20** engine represents a 4-cylinder derivate of this new engine concept and was used as example for analysis and research in this work. Figure A.1 and table A.1 take a closer look on its configuration.

Figure A.1: The BMW N20B20 - "TwinPower Turbo" engine. Source: BMW Group

Engine name	**BMW N20B20** - "TwinPower Turbo" concept
Engine type	spark-ignited
Construction	DOHC 4 in-line (two balance shafts), exhaust gas turbocharger, fully variable valve train *"BMW Valvetronic"*, gasoline direct injection *"BMW high precision injection"*
Piston stroke Cylinder bore	90.1mm 84.0mm
Compression ratio	10:1
Piston rod length Piston offset	144.35mm -14.0mm
Engine displacement	1996cm^3
Valves per cylinder	2 intake / 2 exhaust
Intake valve actuation	variable timing $\Delta = 60$degCA (hydraulic), continuous variable valve lift 0.2 .. 9.7mm (mechanical)
Exhaust valve actuation	variable timing $\Delta = 55$degCA (hydraulic), maximum valve lift 9.3mm (mechanical)
Load control	part load: intake valve lift / timing, near full load: turbocharger with wastegate strategy
Exhaust turbo charger	twin scroll concept with optional scavenging operation
Fuel supply	homogeneous stoichiometric gasoline direct injection, spray guided operation with rail pressure <200bar, multi hole solenoid valve injector
Power output (nominal) Maximum torque	180kW @ 5000-6500RPM 350Nm @ 1250-4800RPM

Table A.1: The BMW N20B20 represents a complex new SI engine generation. Data source: BMW Group

B Reduced fuel details.

In this work different simulations were carried out which need a definition of the specific fuel type in use (e.g. for fuel vaporization). The overview in table B.1 summarizes most important properties and is derived from Pischinger's tabulation [75, 76] refering to **unleaded gasoline fuel ("Euro Super")**. Simulation values that differ from standardization were measured in a detailed fuel analysis at the BMW Group.

	DIN EN 228 spec	simulation values
component mass fractions	h 0.14 / c 0.84 / o 0.02 / n 0.0	h 0.13 / c 0.86 / o 0.01 / n 0.001
molar weight	98kg/kmol	100kg/kmol
stoich. air rate	14.5kg / 1kg fuel	14.05kg / 1kg fuel
density @ 15degC	0.72-0.780kg/l	0.759kg/l
boiling curve curve start vap. @ 70degC vap. @ 100degC vap. @ 180degC curve end	min. 30degC 20 - 50 vol.-% 46 - 71 vol.-% 93 - 97 vol.-% max. 210degC	(winter/summer quality)
vapor pressure	35 - 70kPa 55 - 90kPa	(summer quality) (winter quality)
vaporization heat	420kJ/kg	350kJ/kg
lower heating value	42MJ/kg	42.08MJ/kg
ignition limit	afr = 0.4 - 1.4	
RON MON	at least 95.0 at least 85.0	

Table B.1: SI fuel specification according to international standardization. Differing input values for the 0D simulation are listed separately.

C Operation point details.

For different research tasks of this work, there were repeatedly used similar engine operation points. References of previous chapters shall be resolved in detail in this appendix.

C.1 Sensitivity analysis.

For the sensitivity analysis, considering the quality of input parameters for the combustion model, the following operation points in figure C.1 were used to explore their influences on laminar and turbulent burning velocity s_L and s_T (cf. sections 2 and 3). The simplified sensitivity analysis therefore takes into account and varies **static values** at ignition timing from table C.1.

		operating points					
		1	**2**	**3**	**4**	**5**	**6**
quantity	*unit*						
p	*bar*	10	4	34	16.5	5.8	21
$\mathbf{T}_u$	*K*	455	540	710	710	640	755
xrg	-	0.255	0.2	0.07	0.07	0.12	0.02
AFR, λ	-	1	1	1	1	1	0.88
$\mathbf{l}_F$	*m*	9.8E-05	9.7E-05	7.8E-06	1.3E-05	4.0E-05	7.8E-06
$\mathbf{l}_t/\mathbf{l}_F$	*m*	20.4	20.6	255	151	50.2	258
$\mathbf{s}_L$	*m/s*	0.102	0.300	0.587	0.703	0.596	0.996
TKE	m^2/s^2	30	40	50	150	400	400
specifics		part load, VVT, early ign.	part load, throttled	full load, late ign. (knock)	mid part load	part load, max. speed	nom. power, rich mixt.

Table C.1: Engine map specific operation points for the BMW N20B20 system. The quantities were derived from typical measurement data and serve as input to formulations of the laminar and turbulent burning velocity.
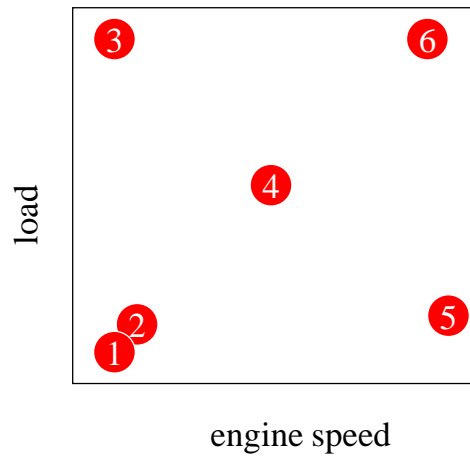
Figure C.1: Engine map with operation points for sensitivity analysis according to table C.1.

C.2 Typical part load operation at 2000RPM/bmep 2bar.

In engine modeling, it is a known problem to provide a good result quality especially at lower part load operation. Thus, the model quality and prediction ability is often assessed in these critical states. For driving cycles, the engine operation at 2000RPM and brake mean effective pressure of 2bar is a special point of interest, where many comparisons are based on. This shall be reason for an extended usage in this work. The considered engine parameters are exemplary for the *BMW N20B20* engine and are listed in table C.2.

		VVT	**throttled**
quantity	*unit*		
engine speed	*RPM*	2000	2000
nominal intake VL	*mm*	2	9.7
intake VL phasing	*mm*	2.76/1.24	9.7/9.7
max intake VL position	*degCA a.TDC*	60	90
intake VL duration	*degCA*	196/170	286/286
induced charge motion	-	swirl, (tumble)	tumble
intake manifold pressure	*bar*	0.9	0.5
trapped air mass per cylinder	*mg*	140	200
ignition timing	*degCA b.ITDC*	35	28

Table C.2: Engine parameters for the operation at 2000RPM and *bmep* 2bar, once for unthrottled (VVT) and once for throttled operation at the BMW N20B20 engine.

D Turbulence modeling details.

D.1 Association of major and minor tumble components.

For the derived turbulence model in chapter 3, it seems useful to associate the two occuring tumble components from figure 3.4 mathematically because they behave akin. This proceeding keeps in mind that component L_x is the main tumbling contributor to global charge motion and the energy cascade. Nevertheless, the minor component L_y is still considered in turbulence production. Thus, a simplification of the calculation can be achieved via transfer from three general charge motion directions $\{x, y, z\}$ into only two left $\{xy, z\}$. Figure D.1 illustrates the proceeding. The left chart shows the CFD
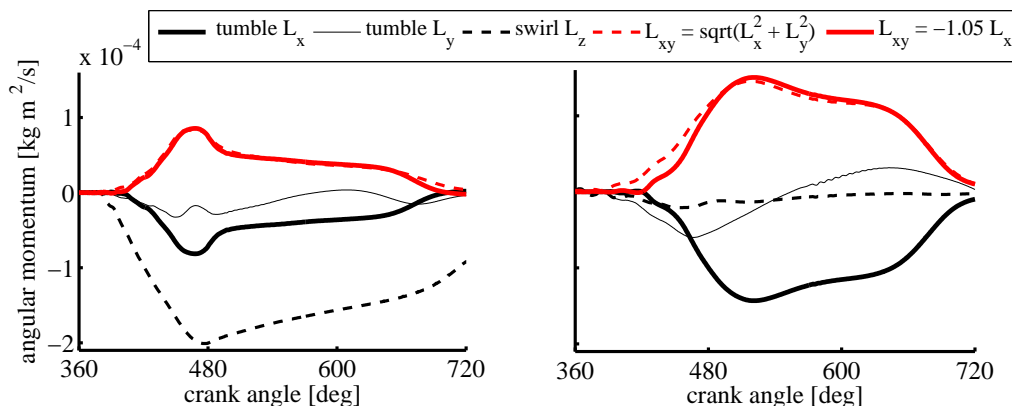
Figure D.1: Association of the main x-tumble component with minor y-tumble for swirl dominated operation *swirl 1* (left) and tumble dominated operation *tumble 1* (right).

charge motion curves for the operation at *swirl 1* whereas the right chart considers the CFD results for an operation at *tumble 1*, compare table 3.2. The tumbling motions in figure D.1 are marked with black solid lines (L_x thick, L_y thin).
The key idea of associating the planar quantities to result in L_{xy} forms as

$$\left| \vec{L}_{xy}{}_{\mathrm{math}} \right| = \left| \begin{pmatrix} L_x \\ L_y \end{pmatrix} \right| = \sqrt{L_x{}^2 + L_y{}^2}. \tag{D.1}$$

167

Equation D.1 represents the correct mathematic form for the absolute length of a planar vector $\vec{L_{xy}}$ and is also plotted in figure D.1.

Following, the detailed analysis of a wide range of CFD results repeatedly shows that $L_x{}^2 >> L_y{}^2$ which simplifies the form for the L_{xy} model as

$$L_{xy} \approx -C_{x,xy} \cdot L_x. \tag{D.2}$$

The turbulence model assumes the constant $C_{x,xy}$ to value around *1.05* for all engine operations. The behavior of this estimation is quite similar to the correct mathematic form and also plotted in figure D.1.

D.2 Quasi-dimensional derivation of the mass moment of inertia.

Derivating the moment of inertia j_{dir} for all directions *dir* is required for the rotational energy which writes

$$E_{dir,rot} = \frac{1}{2} \cdot \frac{L_{dir}{}^2}{m_{cyl} \cdot j_{dir}}.$$

Here, some geometric correlations are needed. The simple cylinder in figure D.2 is bounded by its bore diameter D_{bore} and the actual piston stroke s_{pist}. The rotating
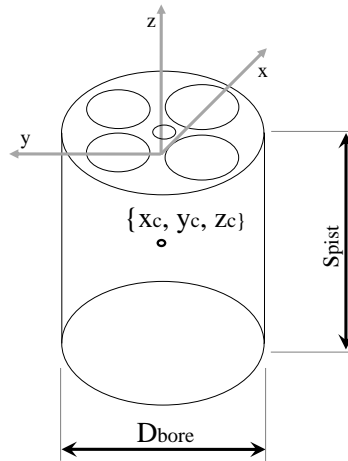

Figure D.2: Actual cylinder dimensions and assumed center $\{x_c, y_c, z_c\}$ of a rotating charge motion.

charge motion is assumed to be centered in the coordinates $\{x_c, y_c, z_c\}$. Formulations

for mass moments of inertia are given in engineering mechanics textbooks, cf. equations D.3 - D.5.

$$J_x = \int_{m_{cyl}} \left((y - y_c)^2 + (z - z_c)^2\right) dm_{cyl} \tag{D.3}$$

$$J_y = \int_{m_{cyl}} \left((x - x_c)^2 + (z - z_c)^2\right) dm_{cyl} \tag{D.4}$$

$$J_z = \int_{m_{cyl}} \left((x - x_c)^2 + (y - y_c)^2\right) dm_{cyl} \tag{D.5}$$

The following mathematical ideas can be applied

- $dm_{cyl} = \rho_{cyl} \cdot dV_{cyl}$; density ρ_{cyl} is constant within the cylinder volume V_{cyl}.

- coordinate transformation into cylinder coordinates with $dV_{cyl} = r \cdot dr d\phi dz$ and a rotational center at

$$\begin{pmatrix} x_c \\ y_c \\ z_c \end{pmatrix} = \begin{pmatrix} 0 \\ 0 \\ -\frac{s_{pist}}{2} \end{pmatrix}$$

- volume integrals are transformed with new boundaries

$$\int_{-\frac{s_{pist}}{2}}^{0} \int_{0}^{2\pi} \int_{0}^{\frac{D_{bore}}{2}} \ldots \cdot r \cdot dr d\phi dz$$

- yielding trigonometric integral parts are simplified at according boundaries bnd

$$\int_{bnd} \sin^2 \phi d\phi = -\frac{1}{2} \cdot (\sin \phi \cdot \cos \phi - \phi)\Big|_{bnd}$$

$$\int_{bnd} \cos^2 \phi d\phi = \frac{1}{2} \cdot (\sin \phi \cdot \cos \phi + \phi)\Big|_{bnd}$$

- cylinder density is rewritten as

$$\rho_{cyl} = \frac{m_{cyl}}{V_{cyl}} = \frac{m_{cyl}}{s_{pist} \cdot \frac{\pi}{4} \cdot (D_{bore})^2}$$

- finally a mass independent moment of inertia is calculated via mass weighting for all directions dir

$$j_{dir} = \frac{J_{dir}}{m_{cyl}}$$

Thus, the formulations from equations D.3 - D.5 are finally mass specific expressions (unit $[m^2]$) as

$$j_{xy} = \frac{1}{4} \cdot \left(\left(\frac{D_{bore}}{2} \right)^2 + \frac{s_{pist}{}^2}{3} \right), \tag{D.6}$$

$$j_z = \frac{1}{2} \cdot \left(\frac{D_{bore}}{2} \right)^2. \tag{D.7}$$

Mathematical derivation yields $j_x = j_y$ and is therefore defined j_{xy} in the following. Figure D.3 shows characteristics of mass specific moments of inertia versus crank shaft position for the *BMW N20B20* engine.
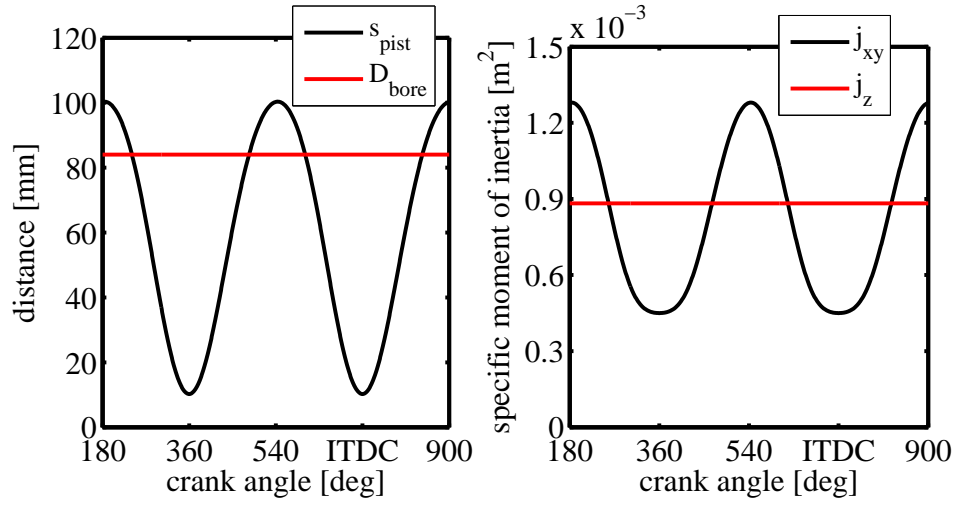
Figure D.3: Mass specific angular inertia versus crank shaft position for the BMW N20B20 engine configuration with 0.5Litres cylinder displacement, a compression ratio of 10 and a piston offset.

D.3 Steady state discharge analysis for a review of tumble generation.

In early stages of combustion development, usually almost no engine hardware is available. Though, engineers require the knowledge about combustion behavior of current geometries. Therefore, a standard CFD workflow was initiated containing the *steady discharge analysis*. This robust tool allows to resolve the trade-off between high mass flows over the intake valves (high air charge for full load operation) and sufficient

air motion in the cylinder. [23, 58]

For a certain cylinder head geometry, the steady discharge analysis is conducted the following way in 3D CFD:

- pre-processing: geometric connection of the cylinder head with a long and open tube (diameter equals D_{bore}) for an undisturbed flow field

- imposing a pressure drop over the inlet/outlet (valves closed)

- quasi-static opening of the intake valves to establish a quasi-static flow field

- for each valve lift: instantaneous evaluation of mean tumble generation (compare equations for "swirl number definition" by IAV, AVL, Tippelmann, etc.) in several predefined planes of the open tube

- additionaly, for each valve lift: instantaneous evaluation of valve mass flow and comparison to isentropic conditions

- post-processing: recording of tumble generation and isentropic flow area versus intake valve lift

The obtained results from a steady discharge analysis are available as early as CAD geometries are defined. Hence, they can be used for further geometrical optimization and as input for simulation tasks (e.g. 1D gas change prediction, pressure trace analysis or turbulence modeling like in this case).

In figure D.4, there can be seen the normalized contribution to tumble generation and mass flow, derived from a steady discharge analysis. It concludes that a more open intake valve creates more tumble because the natural flow field is less disturbed. This matches practical experiences. Moreover, higher mass flows can enter the cylinder at higher valve lifts and equal pressure ratios, which seems trivial.

Because the discussed 0D turbulence model relies on "tumble generation" numbers $\mathrm{Tu}_{x,IVi}$ as seen in section 3.2.5, it is important to feed the calculation with reliable data from the steady discharge analysis.
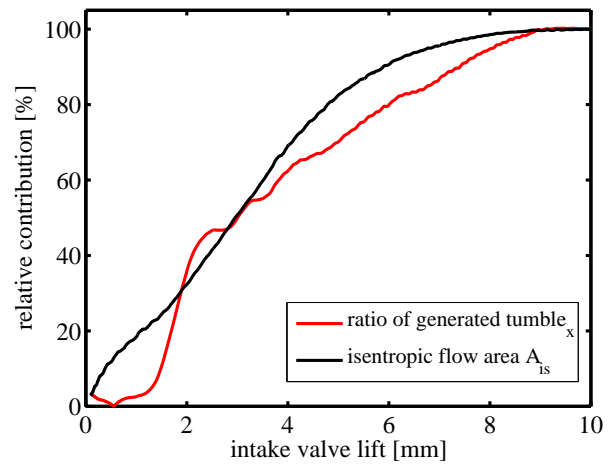
Figure D.4: Tumble generation and isentropic flow area from 3D CFD discharge analysis (valid for one cylinder head configuration of the BMW N20B20 engine). Data source: BMW Group

D.4 Summary for the 0D turbulence model.

In the following, the key ideas of a new turbulence modeling approach are summarized with their equations employed. Used indices refer to table 3.1.

<div style="border:1px solid">

one equation $k - \varepsilon$ turbulence balance
$$dk = dk_{prod} + (dk_{int} - dk_{exh} + dk_{inj}) + dk_{dens} + dk_{squish} - \varepsilon \cdot dt$$

overall turbulent production *"prod"*
$$dk_{prod} = dk_{prod,shr} + dk_{prod,int}$$

shearing production *"shr"* (all engine strokes) $$dk_{prod,shr} \propto -dE_{rot,shr}$$	**instantaneous intake turbulence *"int"*** (intake stroke, intake valves open) $$dk_{prod,int} \propto (d\mathrm{KE}_{int} - dE_{rot,int})$$

intake mean flow kinetic energy
$$\frac{d}{dt}\mathrm{KE}_{int} = \frac{1}{2} \cdot \sum_{IVi} \left(\dot{m}_{IVi} \cdot (\vec{v}_{IVi})^2 \right)$$

decay of rotational energy *"rot"* $$dE_{rot,shr} \propto \sum_{dir} dL_{shr}$$	**build up of rotational energy *"rot"*** $$dE_{rot,int} \propto \sum_{dir} dL_{int}$$

tumble decay and swirl decay *"dir"* $$\frac{d}{dt}L_{dir,shr} = L_{dir} \cdot \Psi_{dir} \cdot \sqrt{k}$$	**tumble production *"x"*** $$\frac{d}{dt}L_{x,int} \propto$$ $$\sum_{IVi} \dot{m}_{IVi} \cdot \mathrm{Tu}_{x,IVi}$$	**swirl production *"z"*** $$\frac{d}{dt}L_{z,int} \propto \Delta\dot{p}_{IVi}$$
decay function $$\Psi = f(s_{pist}/D_{bore})$$	**tumble generation** $$\mathrm{Tu}_x = f(L_{IVi})$$	**momentum flow** $$\dot{p}_{IVi} = \dot{m}_{IVi} \cdot v_{IVi}$$

</div>

Table D.1: Key relations for the new 0D turbulence model.

E Artificial variation of singular influences on combustion.

The introduced model of this work offers new opportunities when learning about the influences on SI engine combustion. It is now possible to artificially vary each influence one-by-one and see, what reaction each sub model shows and how this interacts with with effective fuel burn rates. (This approach is akin to the measurements that can be performed in a so called "rapid compression machine".)

The research work for this sensitivity analysis on the *BMW N20B20* engine proceeds in the following by:

- turning off the gas exchange module of the software coupling, cf. figure 1.4

- selecting an initialization angle α_{ini} shortly before ITDC

- imposing a set of standard operation parameters for the definition of thermodynamics and turbulence

- scaling each influence p, T, x_{rg}, λ and k independently with the remaining input vector being constant

- recording the reaction of burn rates etc. on the input's drift

The mentioned basis operation point is listed in table E.1 and was loosely derived from *swirl 1* operation from section 3. Figures E.1-E.3 then show the model's reaction for the burning durations, whereas $5 - 50\%$ stand for the beginning combustion, $50 - 90\%$ represent the burn out phase and $5 - 90\%$ quantifies the overall combustion duration.

A pressure variation directly changes overall burning durations in figure E.1 (left). A higher pressure initialization leads to shorter burning. The high impact of pressure in this chart does not evolve from the negligible and contradicting shift in laminar burning velocity (cf. figure 2.1) but from a great change of unburned density, which then accelerates the entrainment with $\dot{m}_e \propto \rho_u$ as in equation 5.1.

The temperature variation shows the same trend as an increasing pressure in figure E.1 (right). Here the high sensitivity of s_L in the locally laminar flame is driver for a faster combustion.

Figure E.2 (left) shows the quite sensible reaction of combustion duration on a residual variation. For residual fractions greater than 25% some formulations available for laminar burning velocities reach the zero-crossing - there occurs misfire, compare section

basis operation point derived from *swirl 1*

quantity	unit	initialization value
p	$[bar]$	1.4
T	$[K]$	480
x_{rg}	$[-]$	0.25
λ	$[-]$	1.0
k	$[m^2/s^2]$	14
L_{xy}	$[kg \cdot m^2/s]$	2.96E-05
L_z	$[kg \cdot m^2/s]$	-9.30E-05
α_{ini}	$[degCA]$	60 b.ITDC
α_{ign}	$[degCA]$	40 b.ITDC

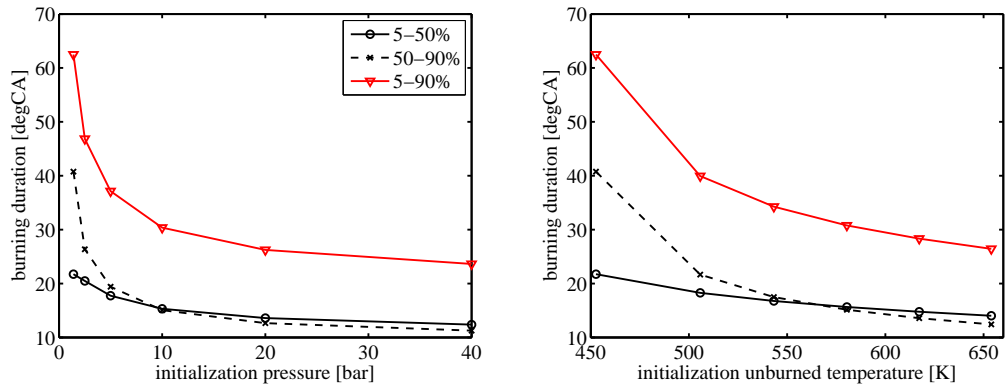Table E.1: Basis operation point for artificial variations of combustion influences.

Figure E.1: Artificial one-by-one variation of pressure p_{cyl} (left) and unburned temperature T_u (right) by entrainment simulation of the combustion duration.
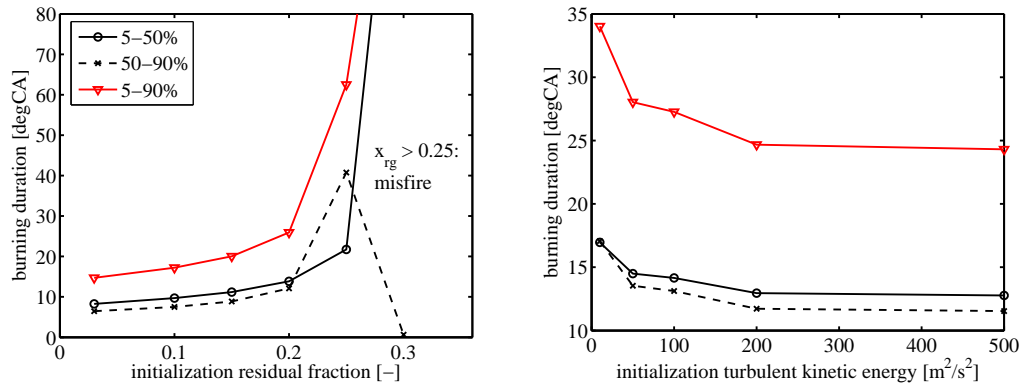
Figure E.2: Artificial one-by-one variation of residual fraction x_{rg} (left) and turbulence k (right) by entrainment simulation of the combustion duration.

2.1.1.

The variation of turbulence in figure E.2 directly impacts on the turbulent burning velocity as visible in section 3.1.3. Thus, an increase of turbulence does not lead to a linear acceleration of the combustion.

  The air-fuel ratio can influence the combustion by temperature effects, which is a well-known effect for calibration purposes. A lean and rich mixture does not really change the beginning combustion and ignition delay, cf. figure E.3 (left). For the burn out process, a very rich and very lean mixture lead to longer burning durations. The mean temperatures in the cylinder in figure E.3 (right) show a direct dependency on afr. A 30% enrichment leads to a higher evaporation cooling and a rich combustion and thus lower cylinder temperatures. This is especially important for the peak temperature values and the burn out. Meanwhile, the difference between lean and stoichiometric combustion nearly vanishes for the plotted temperatures.
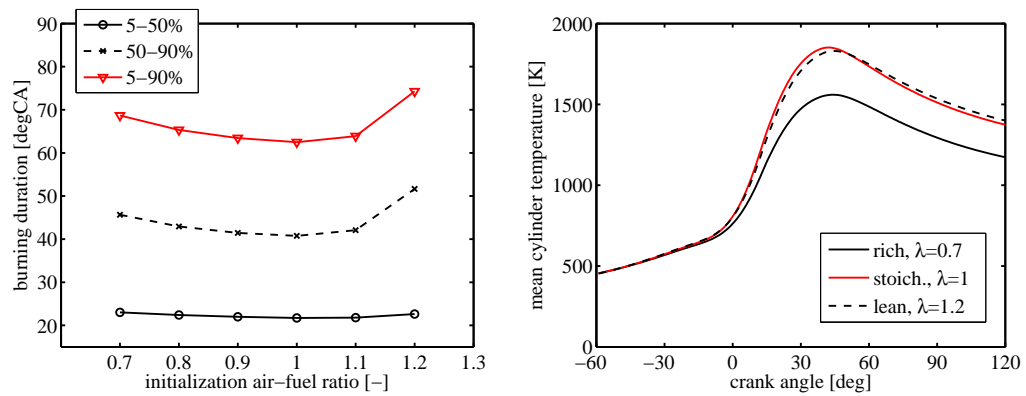
Figure E.3: Artificial one-by-one variation of air-fuel ratio λ (left) by entrainment simulation of the combustion duration. The reaction of mean cylinder temperatures T_{cyl} is also recorded (right).

F Combustion model interface in the GT Power environment.

This section shows, how the introduced combustion model communicates. As the *combustion user code* is directly embedded into a dynamic link library *dll* that GT Power can use, one has to define transfered quantities that are shared by both parties but only edited by one.

Input quantities. *From GT Power* into the combustion model:

- simulation triggers: initialization, cylinder number, cycle number, discretization step, simulation time.

- chemical definitions: species specification (unburned and burned), heat capacities.

- mechanical definitions: cylinder set up, crank train set up, current crank angle, cylinder volume.

- operation details: fuel injection specification, fuel type, air fuel ratio, cylinder mass, residual gas, engine speed, valve timings, current valve lifts, ignition angle.

- cylinder thermodynamics: pressure, temperatures (unburned, burned, averaged), mass flows over the valves.

- side models: heat transfer.

Output quantities. *From the combustion model* back to GT Power:

- combustion flag (combustion active?)

- combustion start angle

- combustion end angle

- current heat release rate dQ

- cumulated heat release Q, ignition delay $\Delta\alpha_{idel}$, crank angle of 50% mass burned $\alpha50$ (CA50)